Inhaltsverzeichnis

Kapitel 1

Introduction

1.1 Mesoscopic physics

Mesoscopic physics has been a rapidly growing field in solid state physics for the last two decades [1, 2, 3, 4]. Being located between the macroscopic world of classical physics and the microscopic world of quantum mechanics it is concerned with electronic properties of systems which are, on the one hand, large enough to use statistical methods, but on the other hand, are sufficiently small that the quantum mechanical phase has to be included. Most of the observed non-classical effects are due to a reduced dimensionality with respect to characteristic length scales. Among them are the electron wavelength λ, the phase-coherence length l_ϕ, as well as scattering lengths for elastic l_e, electron-electron l_{e-e} and electron-phonon l_{e-ph} scattering. For a solid these lengths are typically in the range of nano- to micrometers. The computer industry's demand for smaller and faster electronic devices has fuelled the development of manufacturing techniques for this range, which has made mesoscopic physics accessible to the experimentalist.

A few quantum effects like superconductivity, weak localization or the quantized Hall-resistance [5] can even be observed in macroscopic devices. Nevertheless the major part of mesoscopic physics is restricted to the submicrometer range and to low temperatures, where electron scattering lengths are large compared to the device size. The most famous phenomena are the Aharanov-Bohm effect (resistance oscillations with respect to the magnetic field) [6], the Josephson effect [7], the quantization of the electrical resistance in a quantum point contact [8], Coulomb blockade in small electrical islands [9] and quantum dots [10], which behave like artificial atoms. The

latter two are in consideration for possible computing devices in the future.

The electrical quantity, which is commonly studied, is the resistance in the linear current-voltage (I-V) regime. On the other hand, electrical noise or current fluctuations give additional information about electrical charge transport not accessible by resistance measurements. Therefore noise has become a powerful tool whose importance in mesoscopic physics has continually increased for the past years [11].

1.2 Current fluctuations

1.2.1 General

The current $I(t)$ flowing through a device exhibits fluctuations $\Delta I = I(t) - \langle I \rangle$ in time around the average $\langle I \rangle$. The noise is defined as the mean square fluctuations of ΔI per unit frequency bandwidth, i.e. the spectral density of the fluctuations. Experimentally the fluctuations are measured within a finite frequency bandwidth determined by a band-pass filter restricting frequencies to an interval $[\omega - \Delta\omega/2, \omega + \Delta\omega/2]$. Mathematically, we express the fluctuations in this interval as follows [12]:

$$\Delta I_{band}(t) = \frac{1}{2\pi} \int_{\omega-\Delta\omega/2}^{\omega+\Delta\omega/2} \left[\Delta\widehat{I}(\omega) e^{-iwt} + \Delta\widehat{I}^{*}(\omega) e^{iwt} \right] d\omega, \qquad (1.1)$$

where $\Delta\widehat{I}(\omega)$ is the Fourier transform of $\Delta I(t)$. The second term in the integral arises from frequencies with negative sign. For $\Delta\omega \ll \omega$ the mean squared fluctuations $\left\langle (\Delta I)^2 \right\rangle$ are proportional to the width of the frequency interval $\Delta f = \Delta\omega/2\pi$. Therefore, we obtain for the spectral density:

$$S_I(\omega) := \left\langle (\Delta I_{band})^2 \right\rangle / \Delta f. \qquad (1.2)$$

To derive the frequency-dependence of Eq. (1.2), we need to know on which time scale the fluctuations take place. This is described by the correlation function that connects the fluctuations at two different instants t_0 and $t_0 + t$:

$$\Psi_I(t_0, t_0 + t) := \langle \Delta I(t_0) \Delta I(t_0 + t) \rangle. \qquad (1.3)$$

The averaging is performed over an ensemble of identical systems. In the ergodic case, this is equivalent to averaging over t_0, meaning that Ψ_I depends only on the time difference t. From the Wiener-Khintchine theorem we know that the spectral density is exactly twice the Fourier transform of Ψ_I [13]:

$$S_I(\omega) = 2\widehat{\Psi}_I(\omega) = 2 \int_{-\infty}^{\infty} \langle \Delta I(t_0) \Delta I(t_0 + t) \rangle e^{iwt} dt. \qquad (1.4)$$

Usually physical systems have a certain relaxation time τ, after which all correlations are lost. Therefore, the correlation function $\Psi_I(t)$ tends to zero for $t \gg \tau$ and the noise becomes frequency-independent for $\omega \ll 1/\tau$ (white noise). Normally in an electric transport experiment the sampling rate is much slower than any characteristic relaxation time. This does not mean that the fluctuations vanish or cancel out. They are still present as a white background noise. The most prominent examples are shot noise (Section 1.2.2) and thermal noise (Section 1.2.3). A different case is realized for an ensemble of two-level systems, which fluctuate thermally activated. The characteristic transition time is calculated from the quantum-mechanical tunneling probability and can be very high. The frequencies are broadly distributed, the spectral density is not white any longer, but typically has a $1/f$-dependence [14]. At low temperatures however most of these two-level systems freeze out and give no significant contribution at the usual measuring frequencies.

1.2.2 Shot noise

The discreteness of electrical charge is the origin of fluctuations termed shot noise. This effect was first described by Walter Schottky [15]. If we assume that the electrons pass completely independent through a conductor, then the number of charge quanta N in a time interval T fluctuates and can be described by Poissonian statistics. The average number is given by the mean current $\langle N \rangle = \langle I \rangle T/e$ and the mean square deviation is $\left\langle (\Delta N)^2 \right\rangle = \langle N \rangle$, which is used to calculate the current fluctuations:

$$\left\langle (\Delta I)^2 \right\rangle = \frac{e^2 \left\langle (\Delta N)^2 \right\rangle}{T^2} = \frac{e \langle I \rangle}{T}. \tag{1.5}$$

With Eq. (1.3) and Eq. (1.4), we can determine the universal shot noise expression in the zero-temperature limit:

$$S_I = 2e\,|I|\,. \tag{1.6}$$

The shot noise power is twice the product of the charge quantum and the mean current flowing through a device. This effect can be observed in vacuum tubes or in tunnel junctions where the charge quanta are transferred independent of each other. Interestingly, correlation phenomena like the Pauli principle or Coulomb interaction can substantially suppress shot noise in mesoscopic systems. If on the other hand, several electrons are transferred simultaneously, shot noise is increased, e.g. Andreev-reflection at an NS-junction [16]. Since shot noise depends on the correlation of charge

quanta, a measurement gives additional information about the electrical transport which is not accessible via conductance measurements.

1.2.3 Thermal noise

Every resistor, which is in thermal equilibrium with its environment, displays fluctuations due to thermal activation, even if no bias voltage is applied. This was first observed by Johnson [17]. To explain it with a simple model we assume the resistor R to be shunted by a capacitor C (Fig. 1.1), in which the equilibrium energy $\frac{1}{2}C\langle U^2\rangle = \frac{1}{2}kT$ is stored. An instantaneous voltage fluctuation U at time t_0 decays with a characteristic time RC thus producing a fluctuating current in the resistor:

$$I(t) = \frac{U}{R}e^{-(t-t_0)/RC} \qquad \text{for} \qquad t > t_0. \tag{1.7}$$

Introducing this $I(t)$-behaviour into Eq. (1.4) we get:

$$S_I = 2\int_{-\infty}^{\infty} \langle \Delta I(t_0)\, \Delta I(t_0+t)\rangle\, e^{iwt}dt = 4\int_0^{\infty} \frac{\langle U^2\rangle}{R^2} e^{-t/RC}e^{i\omega t}dt. \tag{1.8}$$

Using $\langle U^2\rangle = kT/C$, we obtain:

$$S_I = \frac{4kT}{R}\frac{1}{1-i\omega RC}. \tag{1.9}$$

Since a real resistor always has a parasitic capacitance, the frequency $(RC)^{-1}$ is therefore the natural frequency cut-off of the thermal noise. For an ideal resistor we get white noise by making the transition $C \to 0$ and

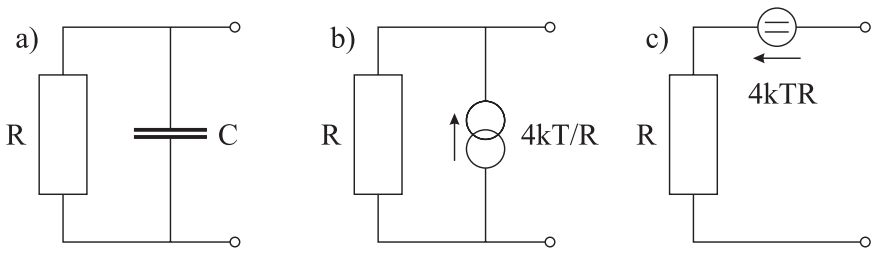

Abbildung 1.1: a) RC-circuit used to derive the thermal noise of a resistor in thermodynamical equilibrium with its environment. b) Equivalent circuit with a current noise source in parallel. c) Equivalent circuit with a voltage noise source in series to the resistor.

we obtain the thermal noise of a resistor R:

$$S_I = \frac{4kT}{R}. \tag{1.10}$$

In a device like a tunnel junction both thermal and shot noise are present. At zero applied voltage the noise is determined by thermal noise, whereas for $eV \gg kT$ shot noise dominates. The crossover is described by:

$$S_I = 2e\,|I| \coth\left(\frac{e\,|V|}{2kT}\right). \tag{1.11}$$

1.3 The Landauer-Büttiker formalism

1.3.1 General

A very successful theory to describe electric charge transport in mesoscopic devices has been developed by Landauer and Büttiker [18, 19, 20, 21]. The electrical conduction of a device is reduced to a scattering problem. The device is represented as a scattering region, whereas the contacts are described by ideal reservoirs with given chemical potential μ and in thermodynamical equilibrium at temperature T. The reservoirs are connected to the scattering region via ideal leads, where no scattering takes place (see Fig. 1.2). The leads consist of 1-dimensional conducting channels which are the subbands or transversal modes of the leads and are described by a quantum-mechanical wavefunction. Every channel contains incoming and outgoing states. When reaching the scattering region, an electron in an incoming state is scattered into one of the outgoing states and is finally absorbed by another reservoir. In the reservoirs the electrons scatter inelastically, lose all phase information and are thermalized. Thus only electrons injected from the same reservoir can exhibit interference effects. Every occupied mode, i.e. every subband below the chemical potential, injects a current from the reservoir into the lead, which reads:

$$I = \frac{e}{h}\mu. \tag{1.12}$$

Now we define $T_{ij,mn}$ as the probability that an electron in mode n coming from reservoir j is scattered into mode m of reservoir i. With $T_{ij} = \sum_{m=1}^{M_i}\sum_{n=1}^{M_j} T_{ij,mn}$, which is the sum of all transmission probabilities from reservoir j to reservoir i, a fundamental relation between applied chemical potentials and currents is given by:

$$I_i = \frac{e}{h}\sum_{i\neq j} T_{ij}\left(\mu_i - \mu_j\right). \tag{1.13}$$

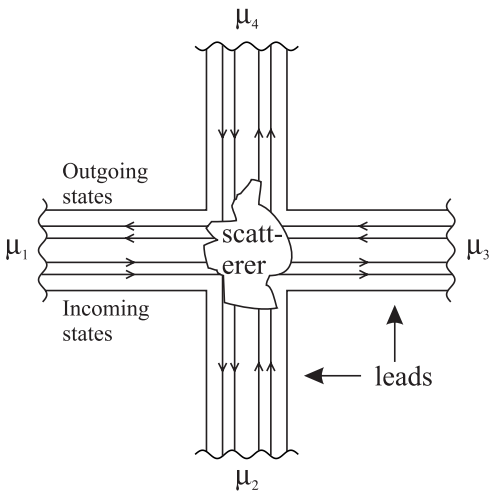

Abbildung 1.2: Four-terminal device with two modes. The incoming states from the reservoirs are scattered into outgoing states.

This equation is the mesoscopic analogon to the second Kirchhoff law. With the knowledge of T_{ij} every circuit in mesoscopic physics can be described.

Since $\mu_1 - \mu_2 = eV$, the conductance for a two-terminal conductor is given by:

$$G = G_0 \sum_{n=1}^{N} T_n, \tag{1.14}$$

with $G_0 := \frac{e^2}{h}$ and T_n being the transmission probability of channel n from one reservoir to the other and N the number of occupied channels. For a perfect wire, which has no scattering, all the transmission probabilities equal one and the conductivity is quantized in units of G_0: $G = N \cdot G_0$. Since there is no scattering in such a wire, fluctuations (noise) are absent in a perfect wire. However for $0 < T < 1$, the uncertainty of whether an electron is transmitted or not gives rise to current fluctuations, which are proportional to $T(1-T)$. The noise at zero temperature (again for the two-terminal conductor) is given by [22, 23, 24, 25, 26]: [1]

$$S_I = 2e\,|V|\,\frac{e^2}{h}\sum_{n=1}^{N} T_n\,(1-T_n)\,. \tag{1.15}$$

[1] Note, that a more general expression of Eq. (1.15) is $S_I = 2e\,|V|\,\frac{e^2}{h}\ \mathrm{Tr}\ \mathrm{tt}^\dagger(1-\mathrm{tt}^\dagger)$, where t is the transmission matrix, that connects the quantum mechanical wavefunction of the incoming states with those of the outgoing states. Therefore, Eq. (1.15) is only correct if $tt^\dagger$ is diagonal, i.e. the modes are chosen to be eigenfunctions of $tt^\dagger$ and the transmission probabilities T_n are its eigenvalues.

The noise is therefore largest for a channel with $T = \frac{1}{2}$. If all the transmission probabilities are small ($T_n \ll 1$), e.g. for a tunnel barrier, we obtain the classical value $S_I = 2e\,|I|$. In this case the tunnel events are so rare that successive events are uncorrelated which results in full shot noise.

1.3.2 The ballistic regime

With the help of Eq. (1.15) we are able to calculate the noise in the shortest possible wire, a ballistic wire, where only scattering with the walls are allowed (Fig. 1.3). A realization of such a conductor is the quantum

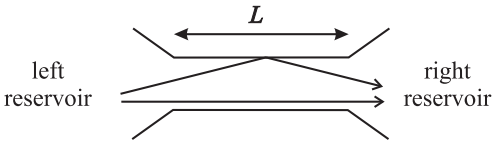

Abbildung 1.3: Two possible trajectories in a ballistic wire, where only elastic scattering with the walls are permitted.

point contact, which is obtained by confining a two-dimensional electron gas (2DEG) at a very small constriction on the order of the Fermi wavelength. By varying the gate voltage the number of transversal modes can be adjusted. Every occupied mode has full transmission and contributes a conductance of $2G_0$ (the factor 2 comes from the spin degeneracy). The

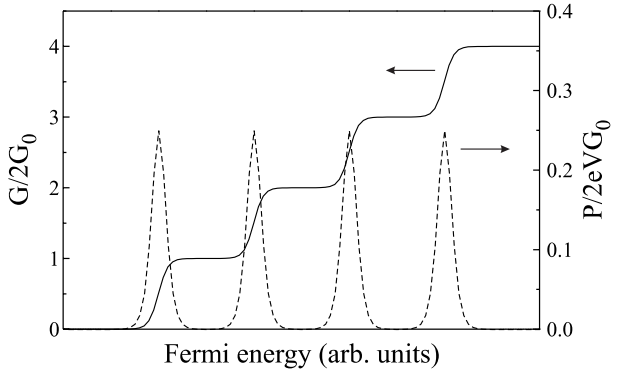

Abbildung 1.4: Conductance and shot noise in a quantum point contact (ballistic wire) as a function of the Fermi energy. The conductance (solid line) is quantized in steps of $2G_0 = 2e^2/h$ corresponding to the number of modes below the Fermi level. Whenever the Fermi energy crosses a new mode, a noisy channel with a transmission probability between 0 and 1 contributes to the noise power (dotted line).

conductance is therefore quantized in units of $2G_0$ [8]. Every unoccupied mode has zero transmission meaning that only noiseless channels are present except if the highest mode is crossing from unoccupied to occupied and has therefore a transmission probability between 0 and 1 (see Fig. 1.4). This was confirmed by Reznikov *et al.* and Kumar *et al.* [27].

1.3.3 The diffusive regime

If the wire length L exceeds the typical elastic scattering length l_e, the motion of the electrons changes from ballistic to diffusive. The electrons are scattered at atomic defects and grain boundaries. The energy is hereby conserved, whereas the direction of the momentum and the phase is changed. The propagation of the electron can be considered as a random walk and therefore a certain probability exists for an electron to be reflected back into the injecting reservoir (Fig. 1.5). The exact knowledge of all the trans-

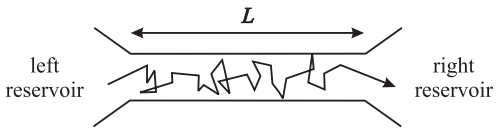

Abbildung 1.5: Random walk of an electron in a diffusive wire due to elastic scattering at impurity atoms or grain boundaries.

mission probabilities is no longer possible, since every wire has a different random distribution of defects and the number of channels is huge. Nevertheless a statistical prediction can be made for a large number of parallel channels. As mentioned above the transmission probabilities are the eigenvalues of the scattering matrix. By taking a large number of unitary random matrices and calculating their eigenvalues, an ensemble average can be performed which results in a probability distribution for the transmission probabilities [28]:

$$p(T) = \frac{Nl_e}{2L} \frac{1}{T\sqrt{1-T}}. \tag{1.16}$$

This is the main result of random matrix theory (RMT), which was initially used to describe the energy level statistic in a nuclear core. Eq. (1.16) is a bimodal function with the two peaks at $T = 0$ and $T = 1$, meaning that most of the channels are noiseless. Inserting Eq. (1.16) into Eq. (1.15) and integrating over T yields:

$$\langle P \rangle = \frac{1}{3} \cdot 2e\,|I|\,. \tag{1.17}$$

Hence shot noise is suppressed by a factor of 3 with respect to the classical value [29]. The brackets around P denote an ensemble average. This is valid if the number of modes $N \gg 1$. In a metallic nanowire with cross-sectional dimensions of 50 nm x 50 nm, there are about 10^4 parallel channels. This can be estimated using $N \simeq A/\lambda_F^2$, where A is the cross-section of the wire and λ_F the Fermi wavelength.

1.4 The semiclassical approach

1.4.1 Non-interacting regime, $L \ll l_{e-e}$

Nagaev proposed a semiclassical approach to determine the noise in a diffusive wire [30]. Starting from a kinetic equation for the electron occupation probability $f(E,x)$, current noise is shown to be related to the fluctuations of the occupation number given by $f(1-f)$. Explicitly, the following equation was derived:

$$S_I = 4G \left\langle \int_{-\infty}^{\infty} f\left(E,x\right)\left[1-f\left(E,x\right)\right] dE \right\rangle_{wire}. \tag{1.18}$$

In this approach, phase coherence is not required in contrast to random matrix theory. Furthermore, it has the advantage that inelastic scattering processes can easily be included. They are introduced by scattering integrals I_{ee} for electron-electron scattering and I_{ph} for electron-phonon scattering. f can be obtained by the following diffusion type equation:

$$D\frac{d^2}{dx^2} f\left(E,x\right) + I_{ee}(E,x) + I_{ph}(E,x) = 0. \tag{1.19}$$

D is the diffusion coefficient of the electrons [31]. The boundary conditions are given by Fermi-Dirac distributions with $f\left(E,0\right) = \left[\exp(E/kT)+1\right]^{-1}$ for the left reservoir and $f\left(E,L\right) = \left[\exp\left((E-eV)/kT\right)+1\right]^{-1}$ for the right reservoir. It is assumed that the reservoirs keep the two ends of the wire at constant electrochemical potential 0 and eV, resp., and at a constant temperature T (Fig. 1.6 bottom left). If inelastic scattering is absent (non-interacting regime), the solution of Eq. (1.19) is a linear combination of the two reservoir distribution functions ($0 \le x \le L$):

$$f\left(E,x\right) = \frac{L-x}{L} f\left(E,0\right) + \frac{x}{L} f\left(E,L\right), \tag{1.20}$$

which has the shape of a two-step function (Fig. 1.6 bottom right). At zero temperature $f = 0$ for $E > eV$ and $f = 1$ for $E < 0$. Only in the range $0 < E < eV$, f can assume a value between 0 and 1 and can therefore

contribute to fluctuations. In this range f depends only on x: $f = x/L$. From Eq. (1.18) we deduce the noise as

$$S_I = 4G \cdot eV \cdot \langle f(1-f) \rangle_x = \frac{1}{3} 2e\,|I|\,. \tag{1.21}$$

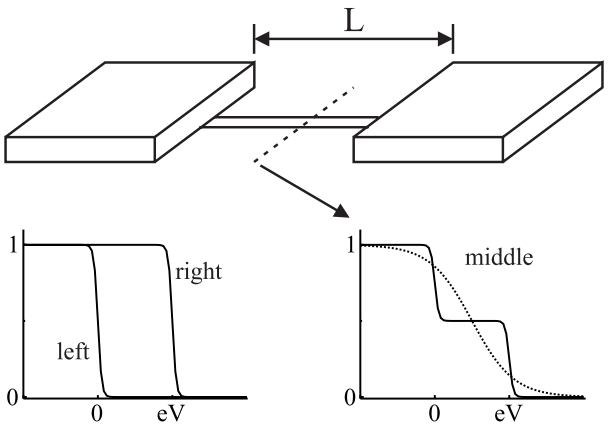

Abbildung 1.6: The electron distribution function of a wire connected to two large reservoirs at its ends is shown for the case of an applied voltage V. In the reservoirs and at the wire ends the distribution function is a Fermi-Dirac distribution at the chemical potential 0 and eV (bottom left). Within the wire it is a two-step function if no inelastic scattering is present, $L \ll l_{e-e}$ (solid line) or it is a Fermi-Dirac distribution with an effective electron temperature kT_e being of the order eV if $L \gg l_{e-e}$ (dashed line).

The same suppression factor is found like in the Landauer-Büttiker formalism. Moreover, the sequential transfer of electrons through a series of tunnel barriers has also been shown to lead to exactly the same noise reduction factor of 1/3 in the limit of a large number of barriers [32]. Recently the universality of the 1/3-suppression factor has been extended to multiterminal diffusive conductors with arbitrary shape and dimension [33]. Note that this reduction factor does not depend on any geometrical parameter like length, width or thickness nor on the sample resistance.

The fact, that the same reduction factor of 1/3 is derived from a quantum mechanical and a classical model, could be ascribed, on first sight, to a numerical coincidence. However this identity is not so astonishing, if one considers that the Drude conductance $G = G_0 N l_e/L$ can also be deduced quantum mechanically (from Eq. (1.16)) as well as classically. Both conductivity and noise rely on the same principles [34].

1.4.2 Interacting regime, $L \gg l_{e-e}$

Another special case arises if $L \gg l_{e-e}$. The electrons can exchange energy among each other and are therefore in a local thermodynamic equilibrium. Hence, the occupation probability $f(E,x)$ is described by a Fermi-Dirac distribution with a *local* electron temperature $T_e(x)$ at the electrochemical potential $\mu(x) = \frac{x}{L}eV$:

$$f(E,x) = \frac{1}{e^{\frac{E-\mu(x)}{kT_e(x)}}+1}. \tag{1.22}$$

The temperature profile $T_e(x)$ along the wire can again be calculated from Eq. (1.19), which reduces to a heat-flow equation. If no electron-phonon scattering is present, it reads as:

$$\frac{\mathcal{L}_0}{2}\frac{d^2T_e^2}{dx^2} = -\left(\frac{V}{L}\right)^2, \tag{1.23}$$

where $\mathcal{L}_0 = \frac{\pi^2}{3}\left(\frac{k}{e}\right)^2$ is the Lorenz number. Eq. (1.18) turns now into $S_I = 4k\left\langle T_e\right\rangle_x/R$. Hence, the excess noise can now solely be interpreted as thermal noise of the hot electrons and S_I is determined by the electron temperature averaged over the whole wire length. An analytical solution exists for the temperature profile:

$$T_e(x) = \sqrt{T^2 + \frac{x}{L}\left(1-\frac{x}{L}\right)\frac{V^2}{\mathcal{L}_0}}. \tag{1.24}$$

For zero temperature it yields

$$S_I = 4k\langle T_e\rangle/R = \frac{\sqrt{3}}{4}\cdot 2e\left|I\right|. \tag{1.25}$$

The noise is again proportional to the current, but has a somewhat higher suppression factor of $\sqrt{3}/4 \simeq 0.43$.

If we allow electron-phonon scattering, there is an additional term in Eq. (1.23). Since the electron temperature is higher than the phonon temperature, there is an energy transfer from the electron to the phonon gas. This reduces the mean electron temperature and therewith the noise in the wire. But as the noise is no more proportional to the current, it is not possible to specify a reduction factor. For $L \gg l_{e-ph}$, the noise is proportional to $L^{-2/5}$ at constant current I and constant wire resistance R and vanishes therefore in the macroscopic limit $L \to \infty$.

1.5 Overview of the different length regimes

Fig. 1.7 illustrates the different length regimes of shot noise. It serves as a guide through this thesis. After a report on how the samples used in this thesis have been prepared (Chapter 2), the experiment described in Chapter 3 is an example for current fluctuations in the ballistic regime. We have used a quantum point contact as a mesoscopic beam splitter and performed an experiment, which is the fermionic analogon to the famous Hanbury-Brown and Twiss experiment. Chapter 4 concentrates on the range $L \sim l_{e-e}$. Steinbach *et al.* [35] have previously confirmed the $\sqrt{3}/4$-suppression for $L \gg l_{e-e}$, but got a value between $1/3$ and $\sqrt{3}/4$ for $L \ll l_{e-e}$. We were able to measure the $1/3$-shot noise suppression. A detailed discussion is given, under which circumstances this is possible. Chapter 5 describes the crossover from $L \ll l_{e-ph}$ to $L \gg l_{e-ph}$, which has been unexplored before. A differential equation for the heat-diffusion in a wire with $L \gg l_{e-e}$ is given. Solving it provides the temperature profile in the wire [36]. Finally in the limit $L \gg l_{e-ph}$ noise can be used as a tool to measure the electron temperature in a heated wire [37]. This is used in Chapter 6 to study the electron-phonon interaction and in Chapter 7 to measure the thermopower in AuFe spin glass wires.

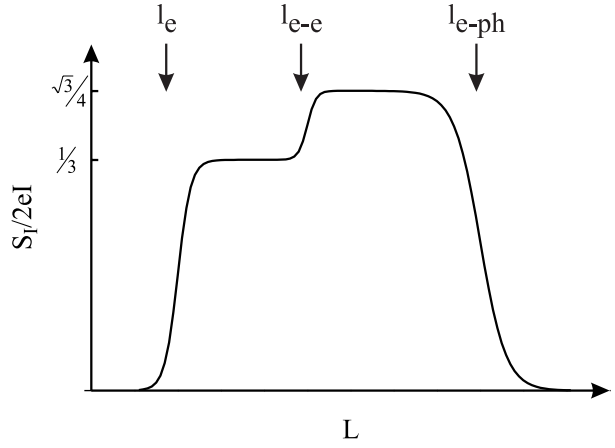

Abbildung 1.7: Noise suppression factor $S_I/2e\,|I|$ as a function of the wire length. Only for ballistic and macroscopic large wires the shot noise vanishes. On a mesoscopic scale there are two universal values: $1/3$ for $l_e \ll L \ll l_{e-e}$ and $\sqrt{3}/4$ if $l_{e-e} \ll L \ll l_{e-ph}$. A noise measurement is therefore a tool to determine scattering lengths like l_{e-e} and l_{e-ph}.

Kapitel 2

Sample fabrication and measurement techniques

2.1 Micro- and nanostructuring

As mentioned in Section 1.1 the mesoscopic samples have to be confined in size in at least one dimension to the order of characteristic length scales like the electron wavelength or typical scattering lengths. At low temperature these are normally of the order of 1 μm or smaller. Thin film evaporation provides a straight-forward tool to fabricate a two-dimensional quantum system on an insulating substrate. In principle no limit is given for the smallness of the film thickness. Many of the interesting quantum effects however are only present in systems with even lower dimensionality like quantum wires for the one-dimensional case or quantum dots for the zero-dimension limit. For the manufacturing of these structures lithographic techniques have to be used [38].

The most common used technique in mesoscopic physics is electron beam lithography. A high-energetic electron beam is focussed onto a resist layer spun on top of the substrate. The beam can be deflected to any point within a given writing field. A computer controls its position such that it follows a predefined pattern, which is developed chemically afterwards. For mass production of large areas, however, optical and X-ray lithography are more suitable, since it is a parallel process, where the whole sample is exposed simultaneously. A previously defined mask is positioned over the resist and is illuminated by UV- or X-ray radiation. Contrary to e-beam lithography, the exposure time is independent of the structure size. But for every pattern a mask has to be produced by e-beam lithography before.

Since in research the pattern has to be changed very often, electron-beam lithography is preferably used due to its higher flexibility and its better resolution.

After the development of the resist, the pattern has to be transferred into a desired material. Two standard processes are described in Fig. 2.1. The left column explains the lift-off process, which is a typical additive process, whereas the right column represents a subtractive process. In the first case a resist layer is spun directly onto the substrate. The desired areas are then exposed to the electron beam. After the chemical development a thin layer is evaporated and makes direct contact to the substrate at the exposed region. In a last step the remaining resist is removed. In contrary in a subtractive process the thin layer of the desired material is evaporated on the substrate before a resist layer is spun on top of it. After the exposure and development step, an etching process is used to remove the material layer at all the places, which have been exposed before. The remaining resist is then removed as well.

All the samples, which were relevant for this work, were manufactured with electron beam lithography combined with the lift-off process. Therefore only this technique is described further in the rest of this chapter.

2.2 Electron beam lithography

2.2.1 Substrate and resist

Monocrystalline pieces from a Si-wafer are usually used as a substrate. They are commercially available as disks with a typical diameter of a few inches and a thickness of a few hundred microns. The polished side has a very small roughness and is therefore suitable for spinning a resist on it.

Before the Si-wafer can be used, its surface has to be cleaned from contaminations. Organic particles can be removed using organic solvents or with a mixture of acids, e.g. H_2SO_4:H_2O_2=3:1. If the Si-wafer has been exposed to oxygen, and this is normally the case, a thin layer of native SiO_2 is present, which saturates the dangling bonds of the Si. If this is undesired, it can be removed with HF, thus leaving a clean surface, where the unsaturated Si bonds are terminated with a hydrogen atom instead. In many cases however a SiO_2 layer is useful as an insulator. In such a case a thick oxide layer can be grown, which is done in an oxygen environment in a high temperature furnace.

The resist layer, which is placed on the substrate, consists in most cases of long polymeric chains. The exact composition depends on the used radiation and the desired spatial resolution. One distinguishes between positive

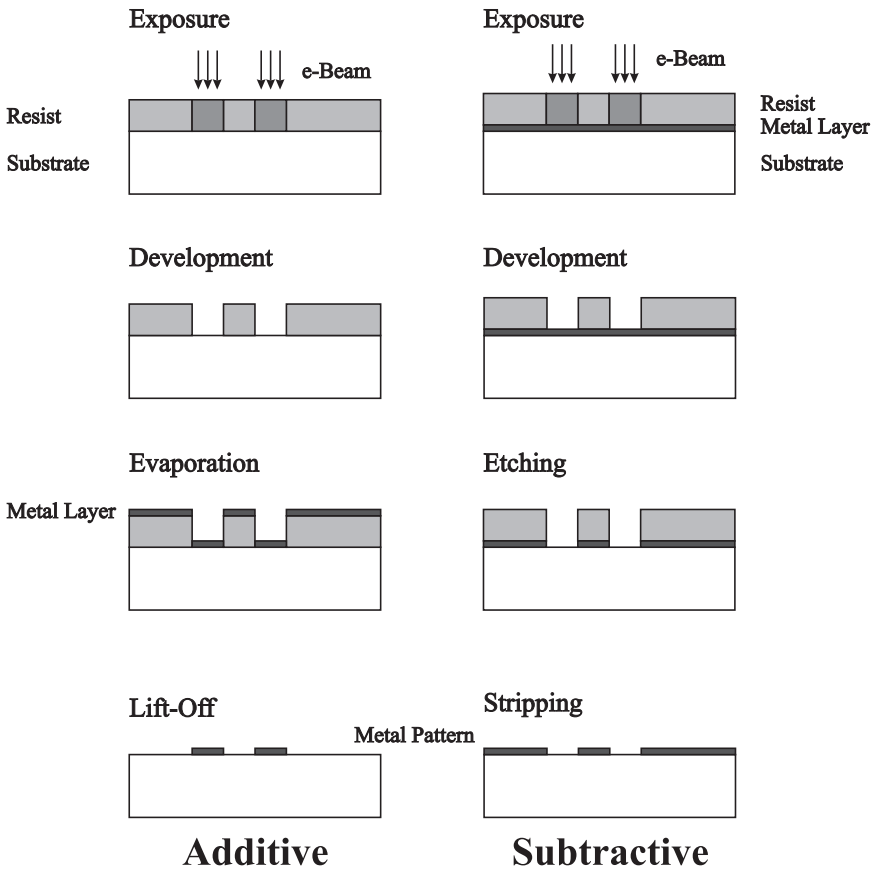

Abbildung 2.1: Two different approaches for a pattern transfer from the resist (grey) into the metal (black). In the lift-off process (left column), the metal layer is evaporated on the developed resist and after dissolution of the resist the remaining metal pattern is the same as the written pattern. In a subtractive process (right column) a full metal layer is evaporated on the substrate and afterwards the undesired pieces are etched away.

and negative resist (Fig. 2.2). In the positive case the electrons entering

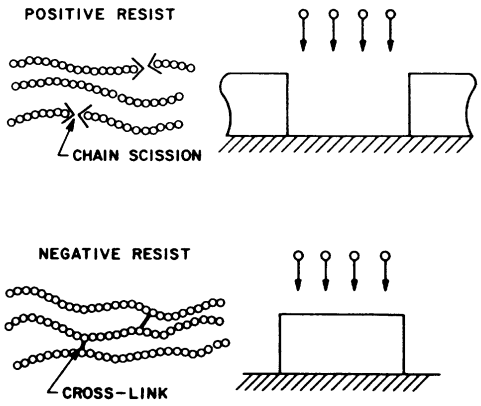

Abbildung 2.2: Schematics of the polymer chains of a positive and a negative resist. In the first case the electrons cut the polymer chains, whereas in the latter case, a cross-linking between polymer chains takes place [39].

the resist cut the polymeric chains into smaller pieces. On the other hand for a negative resist, additional cross-links between the chains are produced by the electrons, thus increasing the molecular weight of the exposed resist. In both cases the developer fluid dissolves the components with lower molecular weight. In a positive resist the exposed area is removed while the unexposed remains and vice versa for the negative resist. For electron-beam lithography poly-methyl-methacrylate, abbreviated as PMMA, has been established as a standard positive resist.

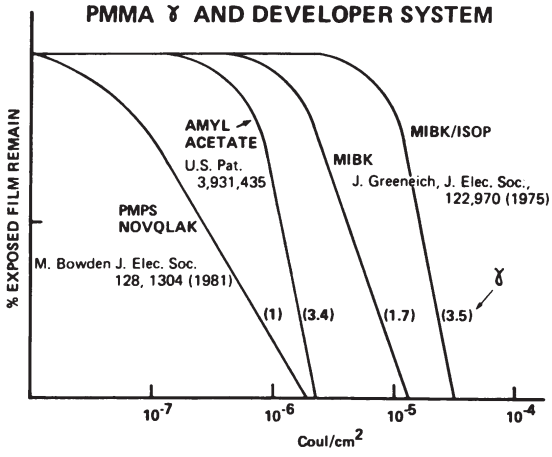

Abbildung 2.3: Plot of the film thickness after development as a function of dose. The three curves to the right correspond to PMMA with different developers, the left curve corresponds to PMPS-Novolak resist. The contrast parameter γ represents the steepness of the curves [40].

2.2.2 Exposure and development

Every resist and its development process can mainly be characterized by two parameters: the clearance dose, given in charge per unit area, which describes the required dose needed to fully remove the exposed resist in the development process, and the contrast parameter γ, which represents the range of exposure dose where the resist changes from exposed to unexposed (Fig. 2.3). For high resolution lithography a high contrast is required. This is normally combined with a high clearance dose, which results in a long exposure time. Those two parameters can be tuned by the molecular weight of the polymers and the composition of the developer.

As shown in Fig. 2.4 the electrons are scattered in the resist (forward scattering) as well as backscattered from the substrate back into the resist. Along their trajectories secondary electrons are emitted, which are responsible for the cutting or cross-linking of the polymeric chains. The exposed area is therefore not limited to the beam diameter, but widens up depending on the typical scattering lengths. The intensity as a function of the distance r from the center of the beam can be described by a two-gaussian

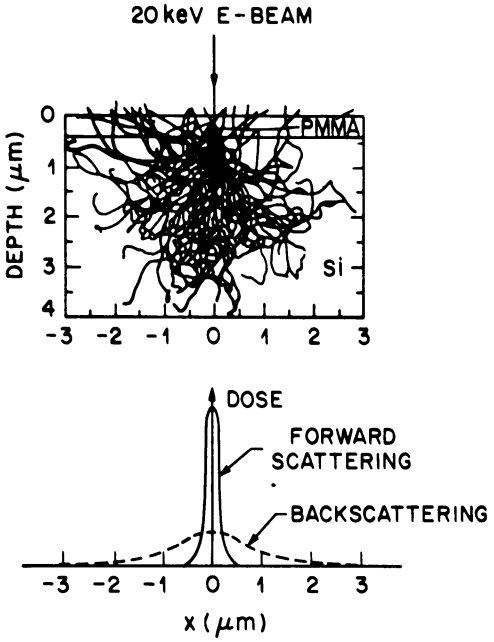

Abbildung 2.4: Top: Monte-Carlo simulation of 100 electron trajectories in PMMA for a 20-keV electron beam [41]. Bottom: Dose distribution for forward scattering and backscattering at the resist-substrate interface [39].

function [42]:

$$I(r) = \frac{1}{\pi\,(1+\eta)}\left[\frac{1}{\alpha^2}e^{-r^2/\alpha^2} + \frac{\eta}{\beta^2}e^{-r^2/\beta^2}\right]$$

where α and β are the typical lengths for forward scattering and backscattering, respectively and η is the relative weight of the backscattering dose. For an electron energy of 35 keV, which was used throughout this work, α is about 75 nm in a PMMA resist. The parameter β depends on the used substrate material as well. In the case of a Si substrate, β amounts to about 5.8 μm. The resolution of e-beam lithography is mainly determined by those two parameters.

2.2.3 Electron beam writer

Fig. 2.5 shows the schematic of an electron beam lithography system. Like in a scanning electron microscope, an electron beam is generated and focussed onto the substrate. A filament is set to a high negative voltage and is heated by a current such that thermal electrons are emitted (thermal emitter). Materials like tungsten (W) or single-crystal lanthanum hexaboride (LaB_6) provide a suitable current. A higher current density can be obtained, when using a sharp filament tip in ultra high vacuum. The radius of the tip has to be so small (a few nm), such that the electric field is high enough enabling the electrons to tunnel into the vacuum (field emitter).

Magnetic coils are used to focus the electron beam on an aperture, which limits the current. The electrons passing through the aperture are focussed with strong magnetic image lenses onto the substrate to a spot of the order of 10 nm. Electrostatic plates are placed between electron gun and aperture and are used to turn on and off the electron beam at a rate of MHz (beam-blanker). Below the aperture, deflection coils direct the electron beam to a predefined location within the scan field. The sample itself can be moved by a motorized stage to allow for a sequential writing on a larger area than the scan field. Beam-blanker, deflection coils and motorized stage are controlled by a computer, where the pattern to be exposed is stored.

The probe current can be adjusted by the aperture angle. A larger angle leads to a higher current but also to a larger spot size, since the spherical abberations become higher. Therefore small structures, which need high resolution, are written with a small probe current, whereas for large areas, high probe currents are used resulting in a small exposure time.

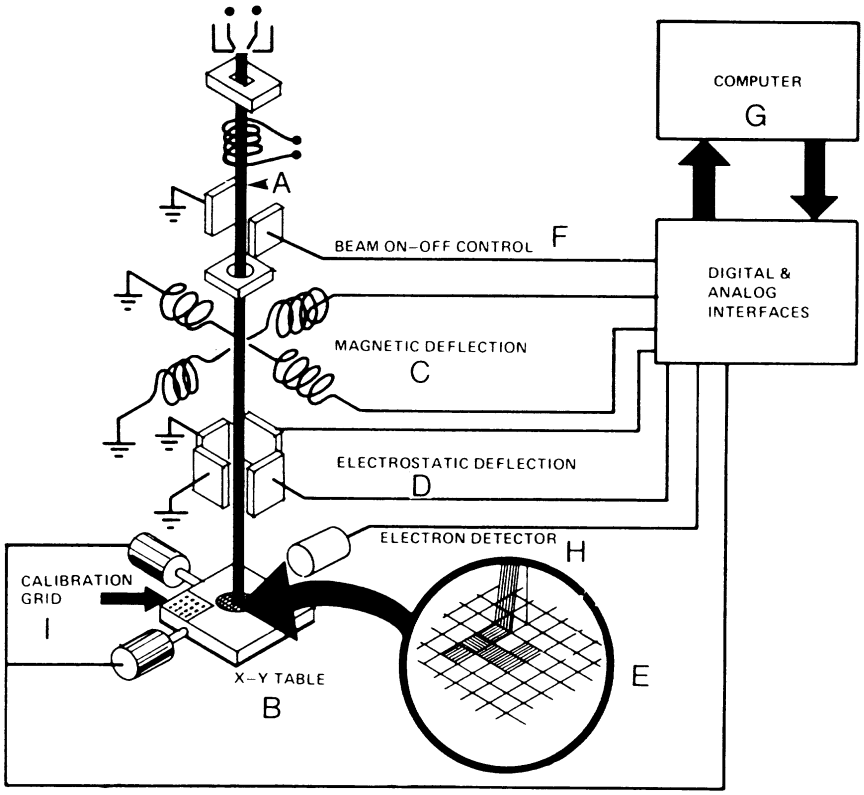

Abbildung 2.5: Schematics of a professional electron beam writer [43].

2.3 Pattern transfer

2.3.1 Thin film evaporation

The structure written in the resist has to be transferred into a layer of the desired material, in our case a polycrystalline metal film. In the lift-off process, this is made by evaporating a thin metal film on the developed resist (see Fig. 2.1). For a successful removing of the resist afterwards, the resist profile has to be undercut. If the walls of the resist are perpendicular to the substrate or even overcut, the film on the substrate and the one on the resist are connected. Due to the electron scattering mechanism, such an undercut profile is normally obtained with electron beam lithography. From Fig. 2.4 it is evident that the exposed region widens up in the resist, thus producing a nice undercut profile. A picture of a typical profile is

shown in Fig. 2.6.

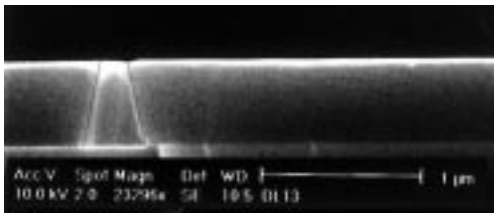

Abbildung 2.6: PMMA-resist profile after development in MiBK:IPA=1:3 for 45 s. The sample was cleaved after the development and inspected under the SEM.

The metal evaporation takes place in a high vacuum environment with a base pressure of typically 10^{-8} to 10^{-7} mbar (see Fig. 2.7). The metal to be evaporated is heated. This increases its vapor pressure and atoms are then thermally emitted into all directions and form a thin film when reaching the sample surface. The heating of the material can be performed using various approaches. A straight-forward method is to place the material in a current-heated boat made of a high-melting material such as

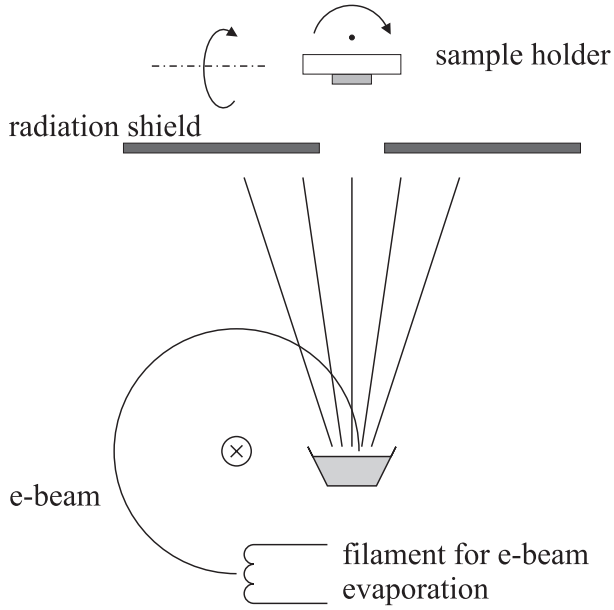

Abbildung 2.7: Schematics of an evaporation facility. A radiation shield prevents the sample stage from being heated by radiation from the pocket. The sample holder can be tilted by two axis to allow for shadow evaporation.

tungsten or molybdenum. A more common method is to accelerate an electron beam on the material, which is placed in a water-cooled pocket. The temperature gradient between the material to be evaporated and the pocket allows to evaporate high-melting materials like niobium without material from the pocket being evaporated simultaneously. When using several pockets with different materials, a sequence of several layers can be evaporated without breaking the vacuum. The combination of more than one evaporation source enables to co-evaporate different materials simultaneously. This yields alloy films with a stoichiometry determined by the relative evaporation rate. Parameters like evaporation rate or sample temperature determine the disorder of the evaporated film and with it its low temperature electrical resistivity.

In Fig. 2.8 a sample after thin film evaporation, but before lift-off is shown. Two lines are written into the resist, which results in small slits after the development. Two metallic lines are evaporated on the substrate through the slits. As a last step the residual resist is removed within a solvent like acetone.

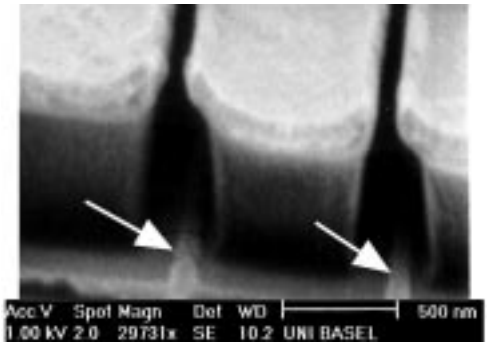

Abbildung 2.8: Scanning electron micrograph of a sample after thin film evaporation and before lift-off. Two metallic lines (indicated by arrows) are evaporated through the two slits. The picture was made with an acceleration voltage of only 1 kV in order to avoid resist damage during imaging.

2.3.2 Multilayer e-beam, alignment

For most of the samples more than just one layer has to be evaporated. If the same pattern is required for different materials, this can be done in one lithography step with the subsequent evaporation of the desired materials without breaking the vacuum. This ensures a good contact between the layers. For most metals, e.g. Au, Al, Cu, a thin film of Ti or Cr has to be evaporated on the substrate before as an adhesion layer. In most cases however, the patterns are different, e.g. a nanowire sample previously

made has to be attached to contact pads of macroscopic size. Only in very special cases this can be performed in one lithography step using the tilt angle evaporation technique (Section 5.2). In most cases two lithography steps have to be performed. After the first structure has been made, a new resist is spun on the substrate and is exposed by the electron beam as well. To align both layers with respect to each other, some alignment marks have to be written in the first lithography step. Usually large alignment marks are placed on the substrate as so-called global marks in order to roughly find the position of the samples. Smaller alignment marks are placed next to each structure such that the second layer can be placed with a high accuracy. This procedure allows to produce a lot of structures in a first step and to select those to be contacted for measurements later (see Fig. 2.9).

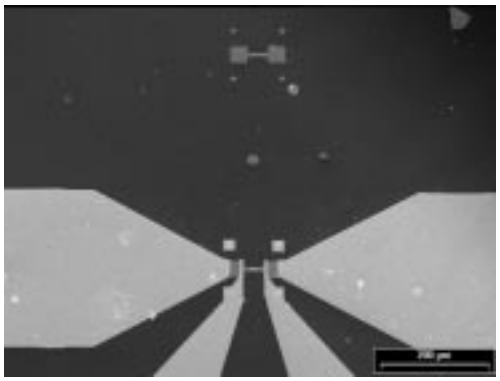

Abbildung 2.9: Scanning electron micrograph of two samples, from which one has been contacted with large pads in a second lithography step in order to enable a four-terminal measurement.

2.3.3 Resolution

The resolution of an imaging system is defined by the smallest distance, at which two points can be separated. In analogy for a lithography system the resolution is determined by the minimum separation of two written lines. For e-beam lithography it is given by the width of the dose distribution function, which is mainly the parameter α. The width of a single line however is a function of the applied line dose and can be significantly smaller. The inset of Fig. 2.10 shows the dose profile as a function of the distance from the middle of the line. The width of the line is then given by the distance of the two points, where the dose profile function equals the clearance dose. Since this function is best described by a gaussian function, there is a logarithmic behaviour between the line dose and the line width.

A typical curve is shown in Fig. 2.10. A doubling of the line dose results in

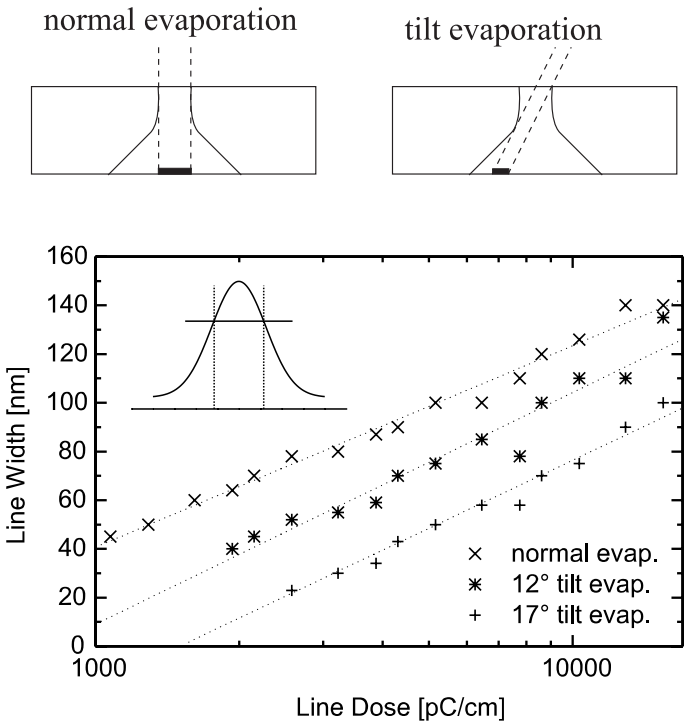

Abbildung 2.10: Due to the shape of the developed area in the resist, the line width can be reduced when evaporating under a tilt angle. The graph shows the measured line width of a Au wire under normal, 12° and 17° tilt angle. Except for the smallest wire around 20 nm, which consisted of partially unconnected Au grains, the lines were homogenous.

a line width increase of about 20 nm. Therefore the line dose is not a very critical parameter for the exposure and can be varied over a large range.

A parameter, which has not been considered up to now, is the angle of the sample with respect to the evaporation source. Usually the evaporation is done under normal incidence angle. Due to the special shape of the exposed area in the resist (Fig. 2.4), a change of the tilt angle can have a substantial influence on the wire width. This is shown in Fig. 2.10. For two different tilt angles the measured line width is plotted again as a function of the line dose. Again a logarithmic behaviour is found and the line width is significantly lower than at normal incidence. With this method, wires smaller than 50 nm are feasible. Fig. 2.11 shows a wire with a width of

27 nm.

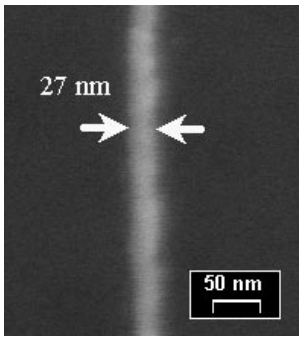

Abbildung 2.11: Narrow Au-wire written with e-beam lithography combined with the lift-off process.

2.4 Bonding and testing

The samples produced with the techniques described above have to be contacted. For that, large contact pads with a size of a few 100 μm^2 have to be evaporated, which make contact to the sample. The substrate is then glued into a chip carrier (see Fig. 2.12) and the pads of the chip carrier are connected with the pads on the substrate using an ultrasonic wire bonder. These connections are made of a well conducting material. The chip carrier itself can be inserted into the chip-carrier socket located in the experimental set-up, e.g. the sample stick for the cryostat.

Before cooling down to low temperatures the sample is normally checked at room temperature. Measuring its resistance provides relevant information, namely whether the sample is conducting at all and whether all bond contacts are low-ohmic. This can however only be done if the Si-substrate has an insulating barrier on top, otherwise the slightly doped Si substrate acts as a shunt resistor. At low temperatures on the other hand, the conduction carriers of the substrate freeze out and the supplied current flows only through the sample.

2.5 Low temperature measurements

2.5.1 Cryogenic liquids

As mentioned in Section 1.1 most of the mesoscopic effects are restricted to low temperatures. All the relevant energies are of the order of meV or

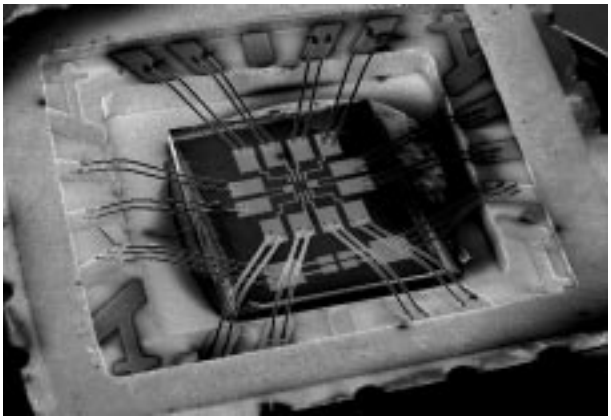

Abbildung 2.12: Device for measurement of the thermopower in AuFe spin glasses. The substrate is glued into a chip carrier. Two or three wires connect the contact pads of the chip carrier with those of the sample.

smaller, which correspond to temperatures of the order of a few K. This means that a great effort has to be made to achieve low temperatures. For this purpose various types of cryostats have been developed [44].

Most of today's cryostats use cryogenic liquids to cool down the sample. Easy to handle and relatively cheap is liquid nitrogen N_2, with which temperatures down to its boiling temperature of 77 K can be achieved. For lower temperatures the more expensive He-4 has to be used. At a pressure of 1 bar, it has a boiling temperature of 4.2 K, which can further be reduced when lowering the pressure. In a He-4 cryostat this is realized with permanent pumping at the He-4 bath, resulting in a lower temperature limit of about 1.3 K. This is however not satisfying for many measurements in mesoscopic physics. Subkelvin temperatures are feasible with the even more expensive He-3, whose vapour pressure curve is shifted towards lower temperatures compared to He-4 (see Fig. 2.13). Its boiling temperature decreases from 3.2 K at a pressure of 1 bar to 0.3 K at 10^{-3} mbar. In a dilution refrigerator a mixture of He-4 and He-3 provides temperatures as small as 10 mK. Even lower temperatures can be achieved with paramagnetic demagnetization of the nuclear core spins.

2.5.2 The He-4 cryostat

The He-4 cryostat used in our laboratories was manufactured by Cryogenics Ltd. Its schematics is shown in Fig. 2.14 left. The He-4 is stored in a

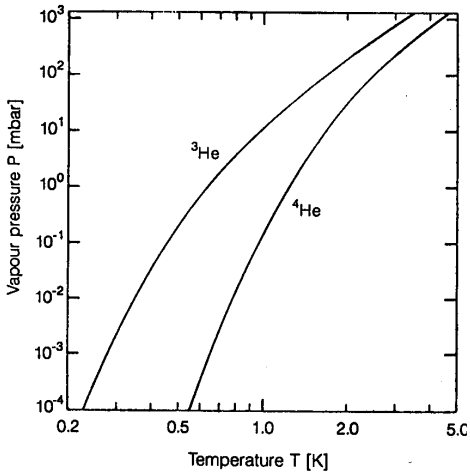

Abbildung 2.13: Vapour pressure of He-4 and He-3 [44].

large reservoir in the interior of the cryostat. Various features are built in to minimize the heat intruding the cryostat and to keep the helium consumption small. The He-4 bath is surrounded by a radiation shield which is thermally connected to the liquid N_2 reservoir and therefore held at 77 K. This protects the He-4 from room temperature heat radiation. The He-4 reservoir, the radiation shield and the outer wall of the cryostat are separated by vacuum, such that no heat conduction can take place. Furthermore all metallic connections are made of stainless steel, which has a small heat conductivity, furthermore the cross sections in vertical direction are minimized to reduce the heat flowing down into the cryostat through heat conduction.

In the middle of the cryostat, a tube is placed, which reaches from the bottom to the top of the cryostat. Into this so called variable temperature insert (VTI) a sample stick can be loaded from the top of the cryostat. The VTI is connected to the He-4 bath with a needle valve through which liquid He-4 enters the VTI. If it is pumped from outside, the He-4 evaporates and the required latent heat is extracted from the environment. This means that the sample stick is cooled to the boiling temperature of the He-4 at the actual pressure. Two thermometers are placed inside the VTI, the first is next to the needle valve, the second one on the sample stick, in close contact to the sample. The sample temperature can be varied by adjusting the power of a heater loop. In order to apply high magnetic fields, a superconducting magnetic coil made of Nb_3Sn is placed in the He-4 bath around the VTI. With a maximum current of 120 A a magnetic

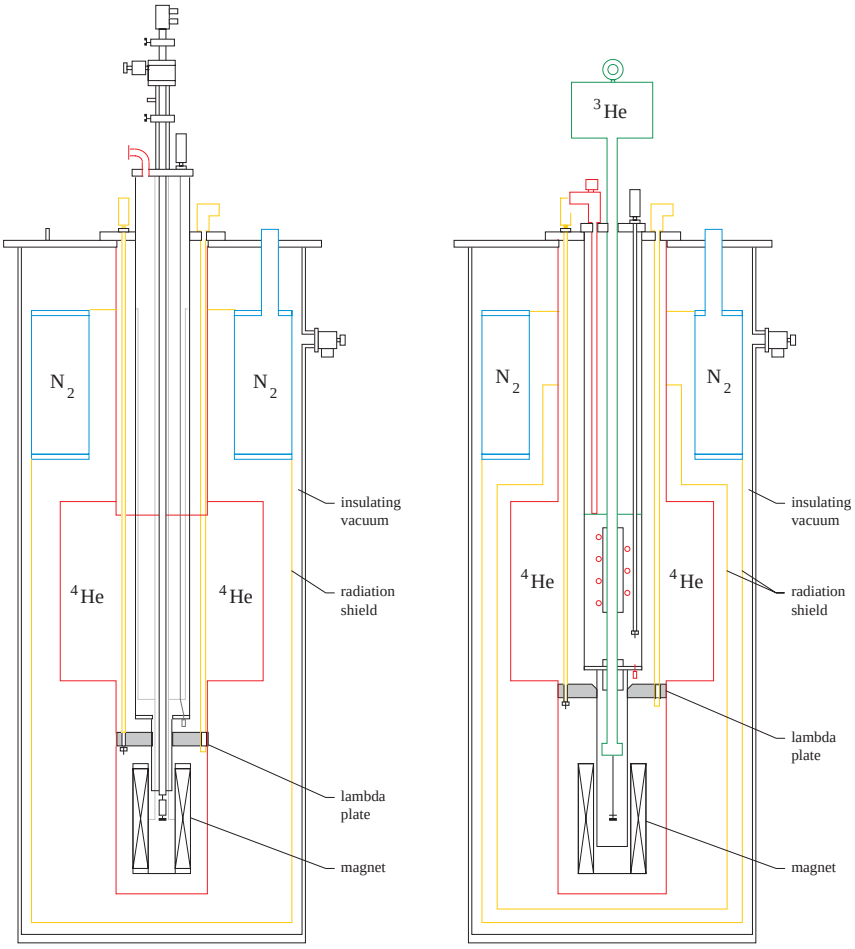

Abbildung 2.14: Schematics of the He-4 cryostat (left) and the He-3 cryostat (right).

field of 9 T can be established. Furthermore the He-4, which surrounds the magnet, can be cooled down to 2.2 K when pumping at the so-called λ-plate. This increases the critical current of the superconducting coil and therefore the maximum field to 11 T.

2.5.3 The He-3 cryostat

As mentioned above, the use of He-3 provides much lower temperatures since its vapour pressure is higher at the same temperature (Fig. 2.13). The costs for He-3 however are astronomically high, such that the He-3 has to be contained in a volume and is recycled. Running a He-3 cryostat consists of two steps. First the He-3 has to be condensed and in a second step the liquid He-3 is pumped on resulting in a base temperature of 0.3 K. The cooling power for the condensing process is provided by a He-4 bath in which the He-3 volume is embedded. Therefore the design of the outer part of a He-3 cryostat (see Fig. 2.14 right) can be borrowed from the He-4 cryostat. At 4.2 K the He-3 is gaseous, in order to condense it, it has to be cooled down to a temperature lower than about 2 K (confer Fig. 2.13). This temperature can be achieved with the same process used in the He-4 cryostat. A needle valve connects the He-4 bath with the so-called 1K-stage, a small pot which is pumped on and reaches a temperature down to 1.3 K. This stage is in thermal contact with the He-3 volume such that a heat exchange takes place. The He-3 is hereby cooled down and condenses into the He-3 pot placed at the bottom of the He-3 volume. After about 30 minutes the He-3 gas has fully condensed and the second step can start. Using a charcoal pump built into the He-3 volume, the pressure is reduced to about 10^{-3} mbar resulting in a base temperature of 0.3 K. This lowest temperature can be maintained during a typical time of about 12 h before all of the He-3 has been evaporated and the condensing step has to be performed again. Below the He-3 pot a sample stage is mounted, which has the same base temperature. With the help of a heater wire, the sample temperature can be adjusted. The He-3 pot and the sample stage are separated from the He-4 bath by vacuum, such that heat exchange with the "warm" He-4 bath is reduced to blackbody radiation, which is however small at these temperatures.

2.5.4 Noise measurement setup

The circuit used to measure noise is displayed in Fig. 2.15. The sample has to be biased by a small current, which is provided by a floating DC voltage source with high series resistors. Two of them are at room temperature, the others are mounted next to the sample on the stick and are therefore at

low temperature. Two capacitors to ground are further used, which build a low-pass filter with a time constant of about 0.1 s. They filter out the high-frequency noise coming from the voltage source and the thermal noise of the resistors at room temperature.

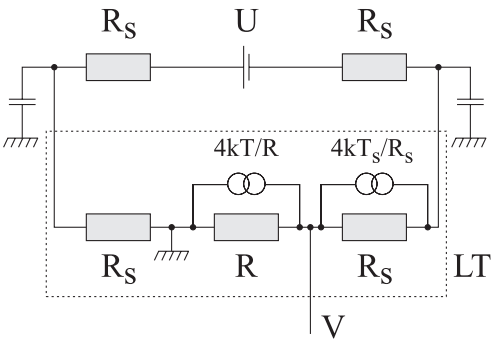

Abbildung 2.15: Schematics of the noise measurement setup. A constant voltage source is connected in series with two large resistors R_s (10 kΩ or 100 kΩ) to provide a constant current. The voltage over the resistor is amplified by two independent preamplifiers (EG&G 5184) and are then correlated using a spectrum analyser (HP 89410A).

To measure the voltage fluctuations over the sample, one end is connected to ground and the voltage at the other end is amplified with a gain of 1000 by two independent low-noise preamplifiers (EG&G 5184) operating at room temperature. The noise spectrum is then obtained by a cross-correlation of the two amplifier signals. Only the common noise signal originating from the sample contributes to the cross-correlation whereas the individual noise of each preamplifier is hereby averaged out. Note that noise measurements are always two-terminal type in the sense that the noise of all contact resistances contribute to the measured noise. Therefore the voltage contacts have to be as low-ohmic as possible to reduce additional voltage noise.

In our setup we measure voltage fluctuations S_U, which are connected to the current fluctuations S_I by $S_U = S_I \cdot R^2$. If we fix the temperature T, the measured thermal noise $S_U = 4kTR$ is proportional to the resistance R. The same dependence is given when measuring shot noise $S_I = 2eVR$ at fixed voltage V. A high enough sample resistance R is therefore very crucial to have an appropriate measurement accuracy.

For an absolute noise measurement, a calibration of the complete setup is unavoidable. The noise signal is diminished by shunt capacitances from the leads in the cryostat by a factor of $1/\sqrt{1+(\omega RC)^2}$. In both cryostats, the capacitance is about 660 pF. Since the reduction depends on R and ω, for every sample a separate calibration has to be performed in the specific

measurement frequency window. For that, the thermal noise of the sample as a function of temperature is measured and compared to $4kT/R$. Current noise of the preamplifiers and external noise sources, e.g. from ground loops, result in a constant noise offset, which is corrected hereby as well.

Kapitel 3

The fermionic Hanbury-Brown Twiss experiment

3.1 Introduction

Experiments aiming at quantum-statistical properties date back to the 1950s [45]. By then Hanbury-Brown and Twiss developed the methods for measuring intensity fluctuations and their correlations between two photon beams. Their invention was driven by the need to improve the so-called Michelson interferometer which was used to measure the size of a star. Measuring the spatial coherence of the electromagnetic field at two distant points yields directly the size of the light source. Hanbury-Brown and Twiss replaced this interference experiment by an intensity correlation experiment. Two telescopes separated by a distance d and oriented towards the same star measure the time-dependent photon intensities $I_1(t)$ and $I_2(t)$ (Fig. 3.1). A correlator determines the time averaged correlation function $\langle \Delta I_1(t) \Delta I_2(t) \rangle$ of the deviations $\Delta I_{1,2} = I_{1,2}(t) - \langle I_{1,2}(t) \rangle$. If the photons incident on the two detectors are completely independent of each other, the correlation function is zero. For distances d smaller than the spatial coherence length, however, a *positive* correlation was measured. Hanbury-Brown and Twiss tested their method in the laboratory first. The light of a mercury vapor lamp was partitioned by a half-silvered mirror into a transmitted and a reflected beam whose intensities were measured by the two detectors. In this experiment a positive correlation is measured as well

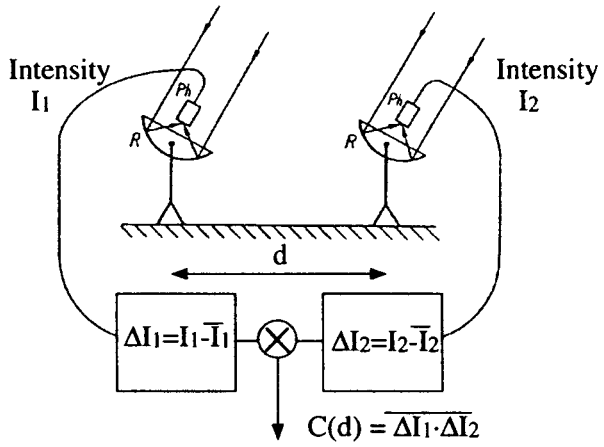

Abbildung 3.1: The Hanbury-Brown and Twiss experiment used to determine the size of a star.

as long as the transmitted and the reflected beam are phase-coherent.

3.2 Quantum statistics

The positive correlation found in both experiments may be interpreted as an enhanced detection probability in a two-photon coincidence experiment. This is a generic property for particles obeying Bose-Einstein statistics. Often the effect is illustrated by saying that bosons have the tendency for bunching (see Fig. 3.2). On the other hand for a stream of classical particles described by Maxwell-Boltzmann statistics, the correlation function is expected to vanish. What about fermions? Due to the Pauli-exclusion principle every fermionic state can be occupied by only one particle. Therefore, a degenerate beam of fermions, which is described by Fermi-Dirac statistics, is expected to show anti-bunching behaviour in contrast to the bunching of bosons. This would result in a negative correlation of the intensity fluctuations in a beam splitter, since an electron being transmitted cannot be reflected at the same time, and vice versa. Although such an experiment was proposed for measuring fermionic properties of electrons [46], a realization was impossible so far. This is because the electron density for a free electron beam, which is generated by thermal or electric-field emission, is so low, that the Pauli exclusion principle does not matter in the beam and the electrons can be described by Maxwell-Boltzmann statistics. Instead of improving on the free-electron beam, this correlation experiment can

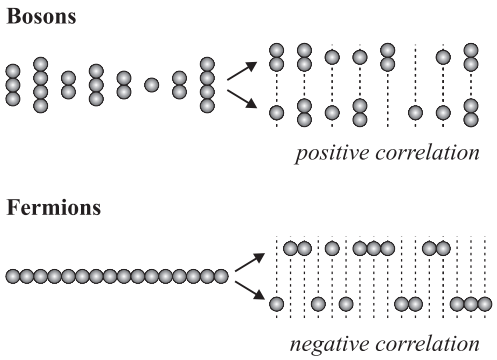

Abbildung 3.2: Particles obeying Bose-Einstein-statistics are known to occur in bunches with an enhanced probability. The correlation of the two branches of a splitted boson beam is positive. In contrary a fermionic state can only be occupied by one particle. This anti-bunching behaviour leads to a negative correlation.

be realized in a semiconductor nanostructure. In the context of shot-noise phenomena in solid state nanostructures, such correlation experiments have been considered so far theoretically [24, 25, 26].

Assume a beam with mean particle number $\langle n \rangle$ incident on a beam splitter with transmission probability T. The average particle number in the transmitted and reflected channel is $\langle n_t \rangle = \langle n \rangle T$ and $\langle n_r \rangle = \langle n \rangle (1-T)$, respectively. For the auto-correlation of the fluctuation $\Delta n_t = n_t - \langle n_t \rangle$ we obtain:

$$\langle (\Delta n_t)^2 \rangle = \langle n \rangle T \mp (\langle n \rangle T)^2. \tag{3.1}$$

The upper (lower) sign denotes fermionic (bosonic) statistics. For a degenerate beam of fermions ($\langle n \rangle = 1$) the autocorrelation is proportional to $T(1-T)$ in accordance with Eq. (1.15). If we set $T = 1$, i.e. a conductor with no scattering, we get the fluctuations of the incoming current $\langle n \rangle \mp \langle n \rangle^2$, which vanishes in the case of a degenerate fermionic beam.

In contrast to the autocorrelation function, which is always positive, the sign of the cross-correlation of the transmitted and reflected beam is specific for the particle statistics:

$$\langle \Delta n_t \Delta n_r \rangle = \mp \langle n \rangle^2 T(1-T). \tag{3.2}$$

If we dilute our fermionic or bosonic gas by making the transition $\langle n \rangle \to 0$, the crosscorrelation decreases faster than the particle number implying that no correlations are left. The autocorrelation approaches the same value for both kind of statistics: $\langle n \rangle T$. In this limit fermionic, as well as bosonic statistics can be approximated by Maxwell-Boltzmann statistics.

While several experiments have measured the autocorrelation (i.e. regular noise) in mesoscopic tunnel junctions and in point contacts [47, 27],

we present in this work the first measurements of a correlation between the transmitted and reflected current in a mesoscopic beam splitter revealing the anti-bunching property of electrons.

3.3 Experiment

In our experiment we use a 2DEG (two-dimensional electron gas) in the quantum Hall regime. A lithographically patterned metallic gate serves as a tuneable beam splitter for the incoming electrons. A constant voltage source with a series resistor injects the electrons at reservoir IN, which is coupled to ground with a capacitor to keep the electrochemical potential constant and to filter out external noise sources (Fig. 3.3). An injected elec-

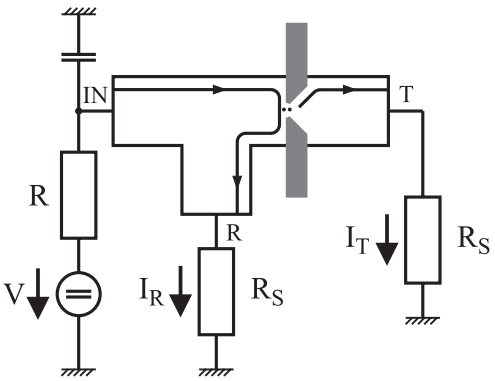

Abbildung 3.3: Experimental set-up for the correlation measurement in a quantum Hall bar with split gate. The electrons are injected into reservoir IN and move along the edge channel until they arrive at the split gate, where they can be either transmitted or reflected. The transmitted and reflected current $I_{T,R}$ and its deviation from the average $\Delta I_{T,R}$ are measured over R_s (1 kΩ).

tron is confined into one of the one-dimensional edge channels and travels along the edge until it reaches the split gate, where it is either transmitted with probability T and leaves the sample at reservoir T or it is reflected and reaches reservoir R. Note that in the case of zero magnetic field, where no edge channels are formed, it would be impossible to separate the incoming from the reflected beam. The transmitted and reflected current $I_{T,R}$ and their deviation from the time-average $\Delta I_{T,R}$ are measured as the voltage drop over R_s. From Ref. [26] we can calculate the cross-correlation of the transmitted and reflected current to be

$$\langle \Delta I_T \Delta I_R \rangle = -2e|I|\Delta f \cdot T(1-T). \tag{3.3}$$

with Δf the measurement bandwidth. It is clear that if one channel carries no current ($T = 0$ or $T = 1$), the cross-correlation is zero, whereas a maximum is attained if $T = \frac{1}{2}$. The prefactor $2e|I|$ is the classical shot noise value proportional to the incoming current I.

In a first experiment the magnetic field is adjusted for a filling factor $\nu = 4$ corresponding to four edge states. Sweeping the gate voltage while measuring the transmitted current reveals a conductance plateau around $V_g = -0.42\ V$, with $I_t/I = \frac{1}{2}$ corresponding to two fully transmitted and two fully reflected channels (Fig. 3.4, point A). Assuming no spin-splitting, two channels with $T = \frac{1}{2}$ and two noiseless channels with $T = 0$ are obtained for $I_T/I = 1/4$ (Fig. 3.4, point B).

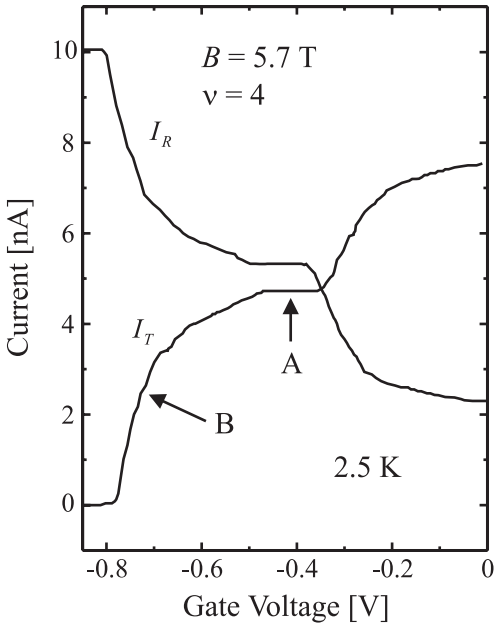

Abbildung 3.4: Transmitted and reflected current at filling factor $\nu = 4$. The plateau at point A corresponds to two fully transmitted ($T = 1$) and two fully reflected channels ($T = 0$). At point B the transmission coefficients are twice $\frac{1}{2}$ and twice 0.

Fig. 3.5 shows the cross-correlation of the fluctuations ΔI_T and ΔI_R versus bias current I for this situation. A nearly linear dependence with a *negative* slope is found proving that the fluctuations are indeed *anti-correlated*. Moreover the autocorrelation of the transmitted channel $\langle(\Delta I_T)^2\rangle$ and the reflected channel (not shown here) have a positive slope, which is in magnitude equal to the cross-correlation. Using the relation $\langle(\Delta I_{IN})^2\rangle = \langle(\Delta I_T + \Delta I_R)^2\rangle = \langle(\Delta I_T)^2\rangle + \langle(\Delta I_R)^2\rangle + 2\langle\Delta I_T \Delta I_R\rangle$ our experiment confirms that the incoming electron beam is noiseless, which is a consequence

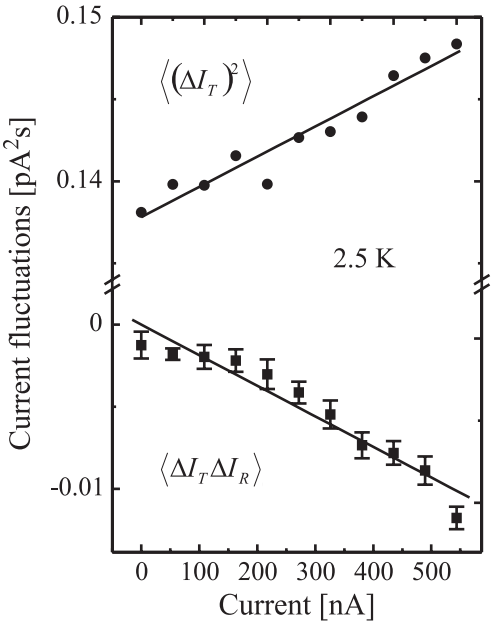

Abbildung 3.5: Autocorrelation of the transmitted and crosscorrelation of both channels versus bias current. The offset of the upper curve is due to the thermal noise of the 1 kΩ-resistor. The absolute slope of both lines is $0.07 \cdot 2eI$.

of the Pauli exclusion principle for a degenerate Fermi-gas. Though the absolute slopes of $\langle \Delta I_T \Delta I_R \rangle$ and $\langle (\Delta I_{T,R})^2 \rangle$ as a function of input current I are identical to within measurement accuracy, the magnitude is too small by a factor of 3.5 compared to Eq. (3.3). This is possibly caused by interchannel mixing or by fractional charge quanta. Similar experiments at $\nu = 2$ produce slopes, which are reduced by only about 25 % compared to the theoretically expected value.

3.4 Thermal fluctuations

Up to now the experiments were in the regime $eV \gg k\Theta$ such that thermal fluctuations are negligible, hence a non-equilibrium experiment has been performed. Can thermal fluctuations at two different reservoirs be correlated, too? From Ref. [26] we expect for the equilibrium correlation of two different reservoirs at zero applied voltage $\langle \Delta I_\alpha \Delta I_\beta \rangle = -2k\Theta G_0 \Delta f (T_{\alpha\beta} + T_{\beta\alpha})$ as a contribution from every edge state. $T_{\beta\alpha}$ ($T_{\alpha\beta}$) is the transmission probability from contact α to β (β to α). This expression predicts that thermal fluctuations at different contacts are also anticorrelated, provided $T_{\beta\alpha}$ or $T_{\alpha\beta}$ are non-zero. For the equilibrium case, however, the negative

sign is not specific to the statistics, it is a mere consequence of particle conservation. In our three-terminal device used before we have a direct transmission from contact T to contact R ($T_{RT} = T$), while for the opposite direction the electrons have to pass through contact IN and hence $T_{TR} = 0$. We expect therefore:

$$\langle \Delta I_T \Delta I_R \rangle = -2k\Theta G_0 \Delta f \cdot T. \tag{3.4}$$

The measured correlations for a filling factor $\nu = 2$ are shown in Fig. 3.6 for three different temperatures (solid symbols). Again negative correlations are observed, which are proportional to the transmission probability T as expected from theory. The inset shows the correlation for fixed $T = 0.5$ and varying temperatures.

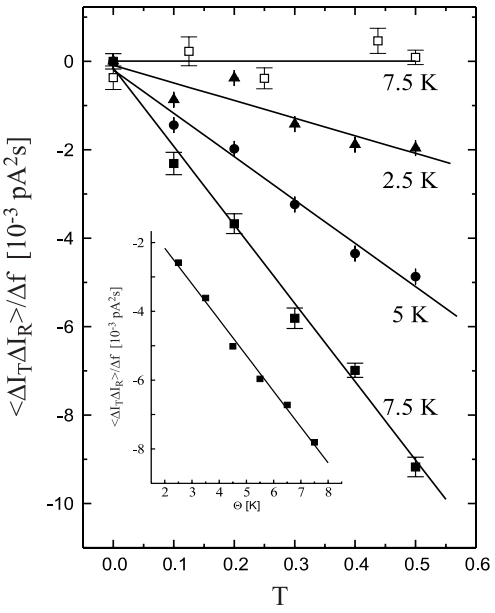

Abbildung 3.6: Correlation of thermal fluctuations at three different temperatures for a three-terminal device (solid symbols) and for a four-terminal device (open symbols). The inset shows the correction as a function of temperature.

In a next step we introduce an additional reservoir between contact T and contact R resulting in a four-terminal circuit (Fig. 3.7). This eliminates any direct transmission between T and R and one would therefore expect that the thermal fluctuations of these contacts are not correlated any longer. This is however only true, if the intermediate reservoirs IN and IN* are fixed at a constant chemical potential via a capacitor connected to ground. In this case the correlations are indeed zero (Fig. 3.6 open

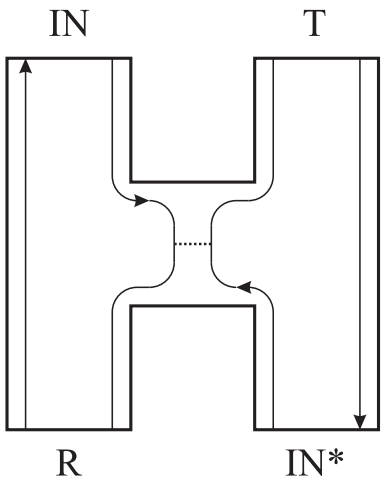

Abbildung 3.7: Schematics of the four-terminal device with no direct transmission between the contacts T and R.

symbols). Otherwise the correlations are still present although the electrons are scattered inelastically between contacts T and R. But in this case the reservoirs cannot be considered as ideal any more, since their chemical potentials are not fixed (cf. Subsection 1.3.1). The chemical potential of reservoir IN (IN*) fluctuates in the same way as the one of reservoir R (T) which is equivalent to a direct transmission from R to T (from T to R).

3.5 Conclusion

We have performed the first shot-noise correlation experiments for a fermionic beam, demonstrating anti-correlation in a two-particle coincidence experiment for fermions caused by quantum-statistical properties of the incident beam. This can be described by the antibunching behaviour of fermions in analogy to the bunching property of bosons which has been explored in the seminal Hanbury-Brown and Twiss experiment. The thermal fluctuations of different reservoirs were also found to be anti-correlated for the case of a direct transmission between both reservoirs. While in a two- or three-terminal device at finite temperature, the equilibrium fluctuations between the two contacts are always anti-correlated and non-zero, in a multiterminal device different contacts may fluctuate independently if there is no direct transmission possible between the two contacts.

Kapitel 4

The 1/3-shot noise suppression in diffusive nanowires

4.1 Introduction

The granularity of charge flow, due to the discreteness of electrical charge in units of e, causes the electrical current to fluctuate around its average value I. The spectral density of these fluctuations S_I are known as noise [11]. In equilibrium ($I = 0$) at temperature T, thermal fluctuations give rise to Johnson-Nyquist noise [17] $S_I = 4kT/R$ for a wire with resistance R. For a non-equilibrium situation, in which a net-current flows, excess noise appears in addition to equilibrium noise. This so called shot noise is directly related to the degree of randomness in carrier transfer caused by the electron scattering in the wire. From shot noise one can therefore obtain information on the conduction mechanism not accessible from conventional resistance measurements. If the number of transferred electrons in a given time interval is determined by a Poissonian distribution, the current shows shot noise with a value given by the well known Schottky formula $S_{\mathrm{Poisson}} = S_I = 2e\,|I|$ [15]. This classical shot noise is observed in tunnel junctions or vacuum tubes, for example [47]. Shot noise for wires connected to electron reservoirs on each end is lower than the classical shot-noise value S_{Poisson} by a factor that depends on the ratio of the wire length L with respect to characteristic scattering lengths like the elastic (l_e), electron-electron (l_{e-e}) and electron-phonon (l_{e-ph}) scattering lengths. In

a ballistic wire ($L \ll l_e$), shot noise vanishes, since scattering is completely absent [27, 48]. In the diffusive regime ($L \gg l_e$), excess noise varies linearly with current only if $L \ll l_{e-ph}$. Two limiting cases can then be distinguished. In the interacting (electron-) regime, i.e. $L \gg l_{e-e}$, the electrons assume a Fermi-Dirac distribution with a locally varying temperature above the phonon temperature. The noise is given by the Johnson-Nyquist noise of the mean electron temperature averaged over the whole wire length. Independent of material and geometric parameters, shot noise is reduced by a factor of $\sqrt{3}/4$ from the classical value [35]. On the other hand in the non-interacting (electron-) regime, i.e. $L \ll l_{e-e}$, the distribution function f is no longer a Fermi-Dirac function. For this regime various theories predict a fundamental shot noise reduction factor of 1/3. Using random-matrix theory, Beenakker and Büttiker have calculated this factor first [29]. In their derivation, the conductor is implicitly assumed to be phase coherent and the factor is obtained as the ensemble-averaged value. In a semiclassical picture, where no phase-coherence is required, the fluctuations of the distribution function f yield surprisingly the very same suppression factor [30]. Moreover, the sequential transfer of electrons through a series of tunnel barriers has also been shown to lead to exactly the same noise reduction factor of 1/3 in the limit of a large number of barriers [32]. Recently the universality of the 1/3-suppression factor has been extended to multiterminal diffusive conductors with arbitrary shape and dimension [33]. Note that this reduction factor does not depend on any geometric parameter like length, width or thickness nor on the sample resistance.

The fact, that the same reduction factor of 1/3 is derived from a quantum-mechanical and a classical model, could be ascribed, on first sight, to a numerical coincidence. However this identity is not so astonishing, if one considers that the Drude conductance $G = G_0 N l_e/L$ can also be deduced quantum mechanically as well as classically. Both conductivity and noise rely on the same principles [34].

Despite the remarkable universality of the reduction factor 1/3 obtained from various theoretical models for the non-interacting electron-regime, a clear experimental confirmation in the asymptotic limit $eV \gg kT$, in which shot noise is much larger than thermal noise, is lacking. To clearly distinguish the non-interacting from the interacting regime by noise measurements, a relatively high accuracy is needed allowing to separate the two close-lying reduction factors 1/3 and $\sqrt{3}/4$ from a measurement of noise, which by itself is a small quantity of order 10 pV/$\sqrt{\text{Hz}}$.

The first experiment in this field was done by Liefrink *et al.* [49] using a two-dimensional electron gas, which was electrostatically confined into a wire. A linear variation of the noise with current was found. The measured reduction factors however were ranging from 0.2 to 0.45. Steinbach *et al.*

[35] found excellent agreement with the $\sqrt{3}/4$-theory for a Ag wire of 30 μm length, but reported a value between 1/3 and $\sqrt{3}/4$ for a 1 μm long wire, although theory [50] predicts $L \ll l_{e-e}$ for this length at 50 mK. Schoelkopf *et al.* were the first to study high-frequency (quantum-) shot noise of diffusive wires [51]. By comparing measured differential-noise dS_I/dI with the 1/3 and $\sqrt{3}/4$ theories, good agreement was found for the non-interacting regime. However, the absolute slope, i.e. the 1/3-reduction factor, was not measured in the asymptotic limit $eV \gg kT$. A novel approach enabling to distinguish between the interacting and the non-interacting regimes, was introduced by H. Pothier *et al.*, who measured directly the distribution function $f(E, x)$ of a wire by tunneling spectroscopy [52].

We will show in the present chapter that the electron reservoirs connected to the wire are of great importance for the confirmation of the 1/3-suppression factor. Bounded by the limiting values 1/3 and $\sqrt{3}/4$, the measured noise-reduction factor can in principle distinguish between the non-interacting ($L \ll l_{e-e}$) and the interacting regime ($L \gg l_{e-e}$). This is, however, only true, if heating in the electron reservoirs is absent. Our experiments demonstrate, that noise-reduction factors close to $\sqrt{3}/4$ can be measured, even though the wires are in the non-interacting regime! This is demonstrated to be caused by unavoidable reservoir heating, which results in a significantly increased measured slope of the shot noise in the asymptotic limit. We discuss noise measurements of three Au wires that mainly differ in the size of the attached electron reservoirs. The sample with the thickest reservoirs, i.e. the highest reservoir heat conductivity, closely approaches the universal 1/3-shot noise reduction factor.

4.2 Theory

4.2.1 Noise in diffusive conductors

The current flowing through a wire exhibits fluctuations $\Delta I = I(t) - I$ around the average current I. The spectral density of these current fluctuations, i.e. current noise, can be written as the Fourier transform of the current autocorrelation function [12]:

$$S_I(\omega) = 2\int_{-\infty}^{\infty} dt e^{i\omega t}\langle \Delta I(t+t_0)\Delta I(t_0)\rangle_{t_0}. \tag{4.1}$$

In thermodynamical equilibrium Eq. (4.1) yields $S_I = 4kT/R$, called thermal or Johnson-Nyquist noise [17]. Under current bias the individual charge pulses of the electrons give rise to out-of-equilibrium noise known as shot noise. If the electrons pass rarely and completely random in time governed

by a Poissonian process, one obtains the classical shot noise $S_I = 2e\,|I|$ as derived by Schottky [15]. If in contrast the electron stream is denser, correlations due to many-particle statistics induced by the Pauli principle or due to Coulomb interaction can significantly reduce shot noise [11]. For $\hbar\omega \ll kT$ thermal and shot noise display a white spectrum (frequency independent). In contrast, resistance fluctuations related to the dynamics of impurities in the sample display in general so called $1/f$-noise proportional to $1/\omega$ over a large frequency range [12]. We restrict ourselves to a frequency range, which is high enough to safely neglect the $1/f$-noise.

An elegant framework to describe the shot noise power of a mesoscopic device is the Landauer-Büttiker formalism [18, 19, 20, 21]. It is valid in linear response and in the absence of inelastic scattering. The current is carried by independent parallel channels with a transmission probability T_n. The conductance is then written as $G = \frac{e^2}{h}\sum_n T_n$ and the shot noise at zero temperature reads [22, 23, 24, 25, 26]: [1]

$$S_I = 2e\,|V|\,\frac{e^2}{h}\sum_n T_n(1-T_n). \tag{4.2}$$

A diffusive wire is described as an ensemble of many parallel channels. Random matrix theory predicts a bimodal distribution function for transmission probabilities, which leads to a suppression of shot noise by a factor of $1/3$ compared to its classical value [29]:

$$S_I = \frac{1}{3}2e\,|I|\,. \tag{4.3}$$

Nagaev proposed a semiclassical approach to determine the noise in a diffusive wire [30]. Starting from a kinetic equation for the electron occupation probability $f(E,x)$, current noise is shown to be related to the fluctuations of the occupation number given by $f(1-f)$. Explicitly, the following equation was derived:

$$S_I = 4G\left\langle \int_{-\infty}^{\infty} f\,(E,x)\,[1-f\,(E,x)]\,dE \right\rangle_{wire}. \tag{4.4}$$

In this approach, phase coherence is not required in contrast to random matrix theory. Furthermore, it has the advantage that inelastic scattering processes can easily be included. They are introduced by scattering

[1] Note, that a more general expression of Eq. (4.2) is $S_I = 2e\,|V|\,\frac{e^2}{h}\,\mathrm{Tr}\,\mathrm{tt}^\dagger(1-\mathrm{tt}^\dagger)$, where t is the transmission matrix, that connects the quantum mechanical wavefunction of the incoming states with those of the outgoing states. Therefore, Eq. (4.2) is only correct if $tt^\dagger$ is diagonal, i.e. the modes are chosen to be eigenfunctions of $tt^\dagger$ and the transmission probabilities T_n are its eigenvalues.

integrals I_{ee} for electron-electron scattering and I_{ph} for electron-phonon scattering. f can be obtained by the following diffusion equation:

$$D\frac{d^2}{dx^2}f\left(E,x\right)+I_{ee}\left(E,x\right)+I_{ph}\left(E,x\right)=0. \tag{4.5}$$

D is the diffusion coefficient of the electrons [31]. The boundary conditions are given by Fermi-Dirac distributions with $f\left(E,0\right)=\left[\exp(E/kT)+1\right]^{-1}$ for the left reservoir and $f\left(E,L\right)=\left[\exp\left((E-eV)/kT\right)+1\right]^{-1}$ for the right reservoir. It is assumed that the reservoirs keep the two ends of the wire at constant electrochemical potential 0 and eV, resp., and at a constant temperature T (Fig. 4.1 bottom left). If inelastic scattering is absent (non-interacting regime), the solution of Eq. (4.5) is a linear combination of the two reservoir distribution functions ($0\leq x\leq L$):

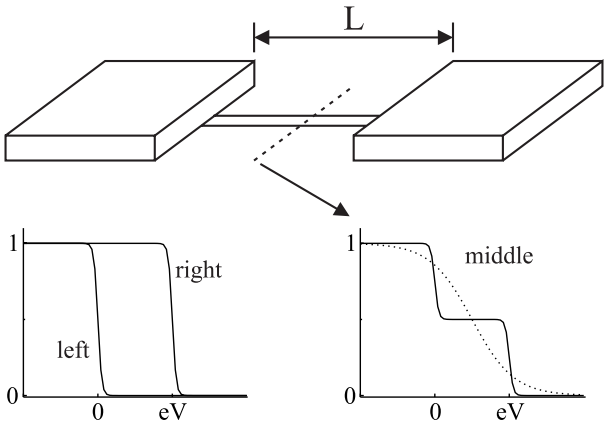

Abbildung 4.1: The electron distribution function of a wire connected to two large reservoirs at its ends is shown for the case of an applied voltage V. In the reservoirs and at the wire ends the distribution function is a Fermi-Dirac distribution at the chemical potential 0 and eV (bottom left). Within the wire it is a two-step function if no inelastic scattering is present, $L\ll l_{e-e}$ (solid line) or it is a Fermi-Dirac distribution with an effective electron temperature kT_e being of the order eV if $L\gg l_{e-e}$ (dashed line).

$$f\left(E,x\right)=\frac{L-x}{L}f\left(E,0\right)+\frac{x}{L}f\left(E,L\right). \tag{4.6}$$

which has the shape of a two-step function (Fig. 4.1 bottom right). Inserting this into Eq. (4.4) one obtains for the noise:

$$S_I = \frac{2}{3}\left[\frac{4kT}{R} + \frac{eV}{R}\coth\left(\frac{eV}{2kT}\right)\right]. \tag{4.7}$$

This equation is identical to the result obtained with the Landauer-Büttiker formalism and describes the crossover from thermal noise at $V = 0$ to an asymptotic shot noise behaviour $S_I = \frac{1}{3}\cdot 2e\,|I|$ for $eV \gg kT$. As mentioned above, the same reduction factor also results from a model using sequential tunneling through a series of tunnel barriers. Although various theories predict a universal 1/3-noise reduction factor for the non-interacting regime, no experiment has yet confirmed the 1/3-slope in the asymptotic limit $eV \gg kT$.

Another special case arises if $L \gg l_{e-e}$. The electrons can exchange energy among each other and are therefore in a local thermodynamic equilibrium. Hence, the occupation probability $f(E,x)$ is described by a Fermi-Dirac distribution with a *local* electron temperature $T_e(x)$ at the electrochemical potential $\mu(x) = \frac{x}{L}eV$:

$$f\,(E,x) = \frac{1}{e^{\frac{E-\mu\,(x)}{kT_e\,(x)}}+1}. \tag{4.8}$$

The temperature profile $T_e(x)$ along the wire can again be calculated from Eq. (4.5), which reduces to a heat-flow equation:

$$\frac{\pounds_0}{2}\frac{d^2T_e^2}{dx^2} = -\left(\frac{V}{L}\right)^2 + , \ \left(\frac{k}{e}\right)^2\left(T_e^5 - T^5\right), \tag{4.9}$$

where $\pounds_0 = \frac{\pi^2}{3}\left(\frac{k}{e}\right)^2$ is the Lorenz number and , is a parameter describing electron-phonon scattering. Eq. (4.4) turns now into $S_I = 4k\left\langle T_e\right\rangle_x / R$. Hence, the excess noise is now solely due to thermal noise of the hot electrons and S_I is determined by the electron temperature averaged over the whole wire length. For $L \ll l_{e-ph}$ the electron-phonon term can be neglected and an analytical solution exists for the temperature profile (inset Fig. 4.2) [53]:

$$T_e\,(x) = \sqrt{T^2 + \frac{x}{L}\left(1-\frac{x}{L}\right)\frac{V^2}{\pounds_0}}. \tag{4.10}$$

This leads to:

$$S_I = \frac{2kT}{R}\left[1 + \left(\nu + \frac{1}{\nu}\right)\arctan\nu\right], \tag{4.11}$$

with $\nu = \sqrt{3}eV/2\pi kT$. For $eV \gg kT$ one obtains $S_I = \sqrt{3}/4\cdot 2e\,|I| \simeq 0.43\cdot 2e\,|I|$.

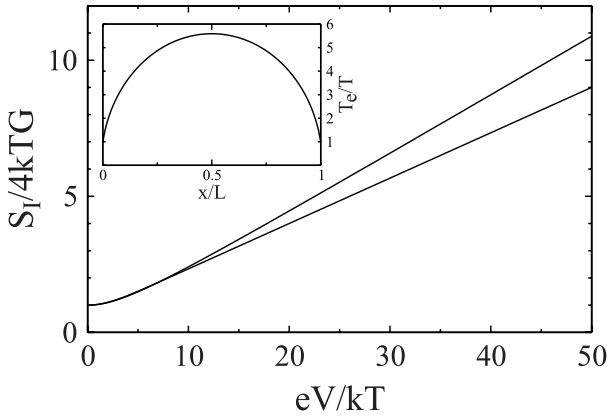

Abbildung 4.2: Calculated noise power for the non-interacting regime $L \ll l_{e-e}$, (lower curve) and for the interacting regime where $L \gg l_{e-e}$ (upper curve). To distinguish between the two regimes in the asymptotic limit a ratio of at least $eV/kT \simeq 10$ is required. The inset shows the temperature profile in the interacting regime along the wire for $eV/kT = 20$.

Fig. 4.2 displays the expected noise versus applied voltage for the non-interacting regime according to Eq. (4.7) and for the interacting electron picture according to Eq. (4.11). Both curves start at $V = 0$ with thermal noise and separate into two straight lines with different slopes for $eV \gg kT$. The figure suggests that at least $eV/kT \geq 10$ is necessary in order to distinguish the two regimes by the measured asymptotic slopes. An experiment under such highly non-equilibrium conditions requires special care in the treatment of dissipation due to the large unavoidable power input. In particular, one has to consider how energy is removed in the reservoirs attached to the wire.

4.2.2 Reservoir heating

The theory described above assumes ideal boundary conditions for the electrons at the immediate wire end. The electrons in the reservoirs are described by a Fermi-Dirac distribution with a constant electrochemical potential μ and a constant bath temperature T independent of the current flowing through the wire. This assumption is only correct for reservoirs of infinite size with infinite electric and heat conductivities. For real reservoir materials, e.g. Au, Ag, Cu, the actual size and heat conductance of the reservoirs will matter. In the following we discuss the different con-

tributions that can give rise to a temperature increase in the reservoirs caused by the generated power V^2/R which has to dissipate in the reservoir and substrate. It will turn out that noise is substantially affected

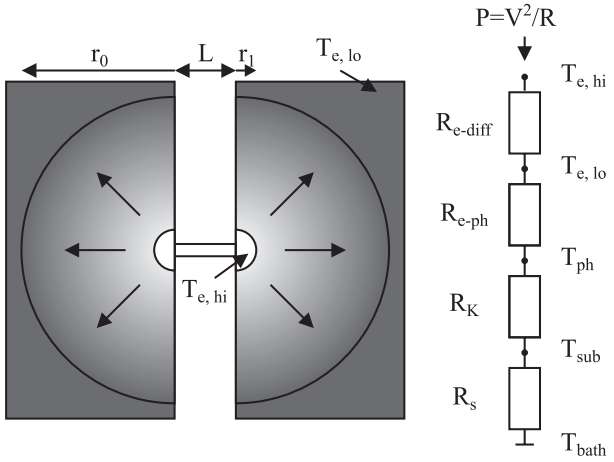

Abbildung 4.3: The power V^2/R produced in the wire has to be dissipated in the reservoirs and in the substrate. For that it has to pass a series of thermal resistors. First, it is distributed in the reservoir by diffusion. Then, the heat is transferred by electron-phonon scattering into the phonon system of the reservoir from where it flows into the substrate and finally into the cryogenic bath kept at the constant temperature T_{bath}. Over every thermal resistor a temperature drop proportional to the resistance and power is induced.

in the non-interacting regime, if the reservoir temperature rises. The heat flows through a chain of different thermal resistors connected in series (see Fig. 4.3). We start at the top of the heat chain where the electronic heat spreads out radially into the whole reservoirs. We take the radius of the two inner semicircles to be $r_1 = l_{e-e}/2$. For the non-interacting regime these semicircles may be considered as part of the wire itself (the inner white part in Fig. 4.3). This is justified since the 1/3-suppression has been shown to hold independent of the wire geometry, as long as the wire is shorter than l_{e-e} [33]. Since a change in temperature is only defined over distances larger than l_{e-e}, we assume a constant temperature in this inner region. This is the highest temperature and denoted with $T_{e,hi}$. Going radially outwards, the power spreads by electronic heat diffusion in the electron gas which is described by a thermal spreading resistance R_{e-diff}, similar to well known electrical spreading resistances. The transfer of energy from

the electron gas to phonons in the reservoirs can be neglected up to a radius of order l_{e-ph}. For higher radii the electron-phonon scattering length provides a natural cutoff for the electronic heat diffusion. We therefore define the largest radius r_0 to be the smaller of either l_{e-ph} or the planar reservoir size L_{res}. At this distance the electron temperature has dropped to $T_{e,lo}$. In the heat-chain model, the thermal resistance for the conversion of energy from electronic to lattice degrees of freedom follows next. First, energy flows into the phonon system of the reservoir resulting in a difference between $T_{e,lo}$ and the reservoir phonon temperature T_{ph}. The corresponding thermal resistance is denoted by R_{e-ph}. Then, a thermal-boundary resistance R_K (Kapitza resistance) may give rise to a difference in phonon temperatures of reservoir T_{ph} and substrate T_{sub}. Finally, the generated heat is transferred into the cryogenic bath, held at the constant bath temperature T_{bath}. This thermal anchor to the bath has the thermal resistance R_s. The temperature difference over each thermal resistor is proportional to the thermal resistance and the power P flowing through it. The minimization of all thermal resistances in the complete heat chain is essential to prevent $T_{e,hi}$ to rise and thus to prevent the injection of hot electrons into the wire. This is in particular important for the non-interacting regime, since it turns out, that a temperature rise in this regime results in substantial additional noise in the asymptotic limit. This can be understood from the asymptotic behaviour of Eq. (4.7) for $eV \gg kT$ which contains a temperature dependent offset in addition to the term linear in I:

$$S_I = \frac{1}{3} 2e\,|I| + \frac{8}{3} kT/R. \tag{4.12}$$

For the temperature T, we have to insert $T_{e,hi}$ into Eq. (4.12) as the temperature of the injected electrons. If $T_{e,hi}$ scales linearly with the current I, the measured slope will be larger than 1/3. It is quite remarkable that in the interacting regime an increase of $T_{e,hi}$ has only a minor effect for the measured noise. As the linear asymptote for $eV \gg kT$ passes through the origin, the correction to the slope is only of second order in kT/eV.

Next we estimate the increase of the four temperatures in the heat chain T_{sub}, T_{ph}, $T_{e,lo}$ and $T_{e,hi}$, when a heat current flows through the chain. The connection between sample and cryogenic bath determines the increase of T_{sub}. We will see later in the experimental section that its dependence on the power P is phenomenologically best described as:

$$T_{sub} = \left(T_{bath}^2 + a \cdot P\right)^{1/2}, \tag{4.13}$$

where a describes the thermal coupling of the sample to the cryogenic bath.

A possible difference between T_{ph} and T_{sub} is due to a Kapitza resistance and can be written as [54]:

$$T_{ph} = \left(T_{sub}^4 + \frac{P}{A\sigma_K} \right)^{1/4}. \tag{4.14}$$

A denotes the area of the reservoir and σ_K is a parameter specific for the interface between reservoir and substrate. Because of the large size of the reservoirs in this work, this is a small effect, but was added here for completeness.

To calculate the difference between electron temperature $T_{e,lo}$ and phonon temperature T_{ph} in the reservoir, we assume for simplicity that the electron temperature is constant over the whole reservoir. When we multiply Eq. (4.9) with the electrical conductivity σ, the second term on the right-hand $\sigma \left(\frac{k}{e}\right)^2$, $\left(T_{e,lo}^5 - T_{ph}^5\right)$ is the power per volume dissipated by electron-phonon scattering and can be set equal to $\frac{V^2}{RAt}$. σ is now the electrical conductivity of the reservoir and t its thickness. We obtain:

$$T_{e,lo} = \left(T_{ph}^5 + \frac{V^2}{R} \frac{R_\square}{, A} \left(\frac{e}{k}\right)^2 \right)^{1/5}, \tag{4.15}$$

where we have introduced the sheet resistance of the reservoir $R_\square = 1/(\sigma t)$. The parameter , is known from noise measurements on long diffusive wires ($L \gg l_{e-ph}$) [54, 37, 36] and can be used to determine the electron-phonon scattering length [54] $l_{e-ph} = 1.31/\sqrt{T^3, .}$

Finally, in order to determine the temperature in the wire $T_{e,hi}$, we have to calculate the temperature gradient in the reservoir due to radial electronic heat diffusion from the inner semicircles with radius r_1 to the outer ones with radius r_0 (see Fig. 4.3). Using cylindrical symmetry the heat flow density is given by

$$\vec{j} = -\kappa \vec{\nabla} T = \frac{P}{2\pi r t} \vec{e}_r, \tag{4.16}$$

where r is the radius of a semicircle between r_1 and r_0, t the thickness of the reservoir and κ the electronic thermal conductivity derived from the Wiedemann-Franz law $\kappa = \pounds_0 T\sigma$, the latter has been shown to be valid in small wires [35, 36]. Integrating over the temperature gradient $\vec{\nabla} T$ with the boundary condition $T(r_0) = T_{e,lo}$, yields for $T_{e,hi} = T(r_1)$:

$$T_{e,hi}^2 = T_{e,lo}^2 + b^2 V^2, \tag{4.17}$$

with

$$b = \sqrt{\frac{1}{\pi \pounds_0} \frac{R_\square}{R} \ln \frac{r_0}{r_1}}. \tag{4.18}$$

For large applied voltages, the second term on the right-hand side of Eq. (4.17) dominates and a linear dependence of the electron temperature with respect to the applied voltage is obtained:

$$T_{e,hi} = b \cdot V. \tag{4.19}$$

When inserting Eq. (4.19) into Eq. (4.12), the increase in noise ΔS_I can be calculated and one obtains for the additional slope:

$$\frac{\Delta S_I}{2eI} = \frac{4}{3}\frac{k}{e} \cdot b = \frac{4}{3}\sqrt{\frac{3}{\pi^3}\frac{R_\square}{R}\ln\frac{r_0}{r_1}}. \tag{4.20}$$

Hence in the independent-electron regime the measured slope is always larger than 1/3! The increase in slope is determined by the ratio $R_\square/R$ and the geometrical parameters r_0 and r_1. The electrical parameters $R_\square$ and R are known accurately. For the radii natural cutoffs have been introduced: $l_{e-e}/2$ for r_1 and the smaller of either l_{e-ph} or the reservoir size L_{res} for r_0. Though the assumed values for r_0 and r_1 are correct on physical grounds, a more rigorous theory may give a slightly different prefactor. Since r_0 and r_1 enter Eq. (4.20) only logarithmically, corrections are small. Both $l_{e-e}(T)$ and $l_{e-ph}(T)$ display a power-law dependence on temperature T effectively resulting in the cutoff term $ln\,(r_0/r_1)$ to be temperature dependent as well, albeit weakly, only proportional to $ln(T)$. This weaker temperature dependence will be neglected in the following. For r_0 and r_1 values typical for the experiment will be used.

In the following we compare the magnitude of the temperature increase caused by electronic heat diffusion using Eq. (4.17) and electron-phonon scattering using Eq. (4.15). In Fig. 4.4 the relative increase $\Delta T/T$ is plotted as a function of bath temperature T for fixed $eV/kT = 20$, which is a typical value used to distinguish between the interacting and non-interacting regime. Within the above mentioned assumption, the contribution from electronic heat diffusion is independent of T, the two plotted values (dashed lines) correspond to a ratio of $R/R_\square = 250$ and $R/R_\square = 1000$ with $r_0/r_1 = 100$. In contrast, the electron-phonon coupling strongly depends on T. Its thermal resistance increases with decreasing temperature, since the electron-phonon scattering rate is proportional to T^3. This results in a drastic increase of $\Delta T/T$ at low temperatures in Fig. 4.4 (solid curves correspond to different lateral reservoir sizes as denoted). Due to this sharp rise the study of non-equilibrium effects at very low temperatures becomes increasingly difficult [37]. The large temperature increase due to the vanishing coupling of the electrons to phonons at low temperatures can only be compensated by enlarging the reservoir volume. Note that both contributions depend on the reservoir thickness, which is included in the reservoir sheet resistance $R_\square$.

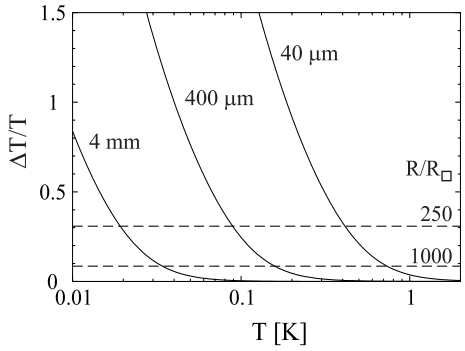

Abbildung 4.4: The relative temperature difference $\Delta T/T$ is plotted for $eV/kT = 20$ as a function of T for various types of reservoirs. The relative increase due to R_{e-diff} (dashed lines) strongly depends on the ratio wire resistance R to reservoir sheet resistance $R_\square$. The contribution from electron-phonon scattering (solid lines) is strongly temperature dependent and increases with decreasing temperature. Its magnitude depends mainly on the reservoir's lateral size (denoted next to the curve), the electron-phonon scattering parameter (here , $= 5 \cdot 10^9$ $\mathrm{K}^{-3}\mathrm{m}^{-2}$) and the ratio $R/R_\square$ (here 250).

Up to now, as a first approximation, we have treated electronic heat diffusion and electron-phonon scattering independently. This is certainly not fully correct. The electron temperature, which is relevant for the electron-phonon scattering, is not constant over the reservoir as previously assumed. To determine the temperature profile self-consistently, we can combine the electronic heat diffusion and the electron-phonon scattering term in one equation, which has a similar form as Eq. (4.9), but now in cylindrical coordinates. We assume that the voltage drop across the reservoirs is negligible, so that the heat-generating term can be omitted:

$$\frac{\pounds_0}{2}\left[\frac{d^2T_e^2}{dr^2} + \frac{T_e}{r}\frac{dT_e}{dr}\right] = , \left(\frac{k}{e}\right)^2 \left(T_e^5 - T_{ph}^5\right). \tag{4.21}$$

The power enters the system at a semicircle of radius r_1 defining the first boundary condition. According to Eq. (4.16) it is given by:

$$\frac{\pounds_0}{2}\frac{d}{dr}T^2\left(r_1\right) = \frac{P}{2\pi r_1}R_\square. \tag{4.22}$$

We now assume the reservoir to be terminated by a semicircle of radius r_0. The heat flow at the end of the reservoir must vanish and the second

boundary condition reads:

$$\frac{\pounds_0}{2}\frac{d}{dr}T^2\,(r_0) = 0. \tag{4.23}$$

The differential equation (4.21) together with the boundary conditions (4.22) and (4.23) cannot be solved analytically. To obtain quantitative estimates for $T_{e,hi}$, we have performed a simulation using the method of finite elements. We have varied the power P, the electron-phonon scattering parameter , and the reservoir outer and inner radii r_0 and r_1. The main results are as follows: The electron temperature decays approximately exponentially from $T_{e,hi}$ at the inner radius r_1 to a base temperature $T_{e,lo}$ at r_0. The decay length, over which $T_e - T_{ph}$ is reduced by a factor e, is about $l_{e-ph}/4$, where l_{e-ph} is the electron-phonon scattering length at $T_{e,lo} \simeq T_{ph}$. The resulting temperature profile of two simulations with different , is plotted in Fig. 4.5. The inset shows the difference $T_e - T_{ph}$ on a logarithmic scale. The two straight slopes indicate the exponential decay of the temperature T_e to T_{ph}. The decay length depends only slightly on

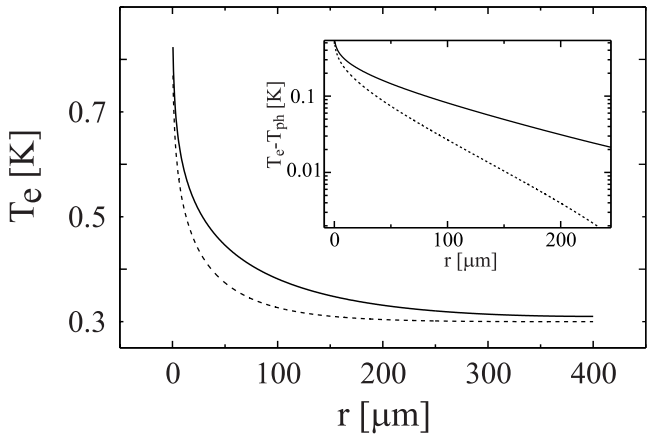

Abbildung 4.5: Resulting temperature profile in the reservoir obtained from a computer simulation using the method of finite elements. For an incoming power of 200 nW and a reservoir sheet resistance $R_\square = 42$ mΩ, the electron temperature $T_{e,hi}$ rises from 0.3 K to 0.8 K. The curves are calculated with different electron-phonon scattering parameters: , $= 5 \cdot 10^9$ K^{-3}m^{-2} for the dashed line ($l_{e-ph} = 110$ μm) and , $= 1 \cdot 10^9$ K^{-3}m^{-2} for the solid line ($l_{e-ph} = 250$ μm). The inset shows the logarithmic behaviour of the same graphs but after subtracting the phonon temperature of 0.3 K from the electron temperature.

the power P. If $r_0 \geq 2 \cdot l_{e-ph}$ no significant raise of $T_{e,lo}$ with respect to T_{ph} is found and $T_{e,hi}$ depends only on the incoming power and the reservoir sheet resistance. This corresponds to the limit described above, where the electron-phonon contribution is small compared to the one from electronic heat diffusion. It can be used as a design criteria for reservoirs appropriate in minimizing dissipative reservoir heating. The reservoir size, which is required for this is plotted as a function of T_{ph} in the inset of Fig. 4.6. The simulation also shows that the functional behaviour of $T_{e,hi}$ with applied voltage V can be described like in Eq. (4.17). The relation $b \propto \sqrt{R_\square / R}$ is still valid consistent with Eq. (4.18) and the proportionality factor corresponds to a ratio of about $r_0/r_1 = 100$, which is very reasonable. Such a ratio would also follow from our simple analytical model, when the electron-phonon scattering length is inserted for r_0 and the electron-electron scattering length for r_1 taken at subkelvin temperatures. This discussion shows that large reservoirs are needed to minimize the increase in reservoir temperature. In particular, if $L_{res} \gg l_{e-ph}$ is followed in the design of the reservoirs, the main contribution for the relative temperature rise $\Delta T/T$ is caused by electronic heat diffusion, which is displayed in Fig. 4.6 as a function of the applied voltage for three different ratios of $R/R_\square$. As can be seen, the temperature increase can be substantial.

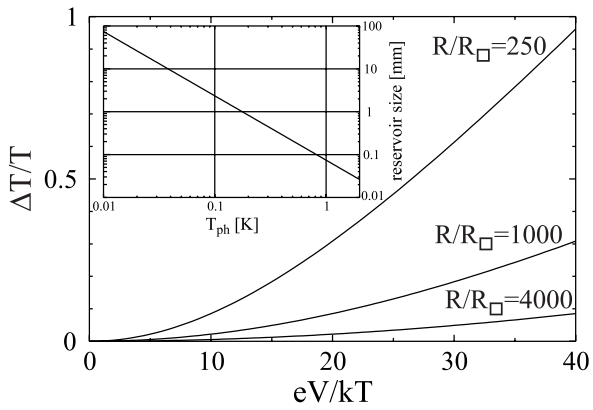

Abbildung 4.6: Calculated temperature increase $\Delta T/T$ due to electronic heat diffusion as a function of applied voltage. A linear variation follows if $eV/kT \gg \sqrt{R/R_\square}$. The inset shows the lateral reservoir size necessary to prevent a temperature increase due to electron-phonon scattering. It is given by $4l_{e-ph} = 5.24/\sqrt{T^3}$, with , $= 5 \cdot 10^9$ K^{-3}m^{-2}.

4.3 Experiment

4.3.1 Design

In the experiments described below we explore the 1/3-shot noise suppression in the non-interacting regime and study the influence of different reservoir configurations. In view of the important role of the reservoirs discussed above a careful design of the experiment is crucial. The non-interacting regime requires $L \ll l_{e-e}$. For an estimate of l_{e-e} we use Altshuler's formula valid for a one-dimensional wire:

$$l_{e-e} = \left[\left(\frac{\sqrt{2}}{k_B} \right) \left(\frac{\hbar}{e} \right)^2 \frac{D \cdot w}{T \cdot R_\square^w} \right]^{1/3} . \tag{4.24}$$

where w is the width and $R_\square^w$ the sheet resistance of the wire [50]. For a typical Au wire with a thickness of 15 nm, diffusion coefficient $D = 120$ cm^2/s, width $w = 100$ nm and $R_\square^w = 2.3\ \Omega$, we find a scattering length $l_{e-e} = 4.2\ \mu$m at 0.3 K. Using standard e-beam lithography, a wire with a length of 1 μm connected to two reservoirs is feasible. Shorter wires are difficult to fabricate because of proximity-effect from exposing the large areas of the two reservoirs.

As mentioned above, in order to distinguish the 1/3 from the $\sqrt{3}/4$-regimes a ratio of at least $eV/kT \simeq 10$ is necessary. A low base temperature is required, since otherwise the applied voltage becomes too high and electron-phonon scattering in the wire is unavoidable. To get an estimate of the influence of electron-phonon scattering on noise we have to compare the wire length with the electron-phonon scattering length at temperature eV/k. We find that a deviation in noise of about 1% would result if $L \simeq 4 \cdot l_{e-ph}$. For a 1 μm long wire with , $= 5 \cdot 10^9$ m^{-2}K^{-3} this relates to a maximum voltage, which corresponds to 17.6 K. For a ratio of $eV/kT = 40$ (the largest ratio used in the experiment), the bath temperature shall be lower than 440 mK. As explained above the reservoir heating strongly depends on the ratio $R_\square/R$, which ought to be as small as possible to avoid heating. In our experiment we will vary this ratio. As we have fixed the length of the wire, its width and thickness should be small to achieve a high wire resistance. On the other hand, the reservoirs have to be as thick as possible and made of a highly-conductive metal to reduce $R_\square$.

The size of the reservoirs has to be chosen according to the electron-phonon scattering length l_{e-ph} in the reservoir. Its radius r should be about twice l_{e-ph} to avoid a significant difference between electron and phonon temperature, see inset of Fig. 4.6. With , $= 5 \cdot 10^9$ m^{-2}K^{-3} we obtain $l_{e-ph} = 1.31/\sqrt{T_e^3}$, $= 110\ \mu$m at 0.3 K, which means that two rectangles

with 200 μm $\times$ 400 μm on each side are sufficient [36]. Note, that for 50 mK this length even exceeds 1.5 mm.

An estimate has also to be made for the temperature increase due to a Kapitza resistance. As a worst case estimate for σ_K we use 100 W/m^{2}K^4. With a heating power of 50 nW we expect a temperature increase of only 25 mK, which is small compared to the applied voltage $eV/k = 12$ K.

In our experiment, a possible increase of the substrate temperature T_{sub} is taken into account, since we can measure T_{sub} directly with noise thermometry using an additional monitor wire on the same substrate.

4.3.2 Sample fabrication

The samples were produced with standard e-beam lithography. A 600 nm thick PMMA-resist was spun on an oxidized Si(100)-wafer and structured with a JEOL JSM-IC 848 at an acceleration voltage of 35 kV. The pattern consisted of a line (line dose $\sim$ 1.8 nC/cm) and of two areas on each side of the line. To correct for the proximity-effect the area dose was increased in steps from the wire ends ($\sim$ 200 μC/cm^2 $\equiv$ 100 %) to the outer part of the 50 μm writing field (140 %). The pattern with the corresponding dose distribution is shown in Fig. 4.7. These small structures were written

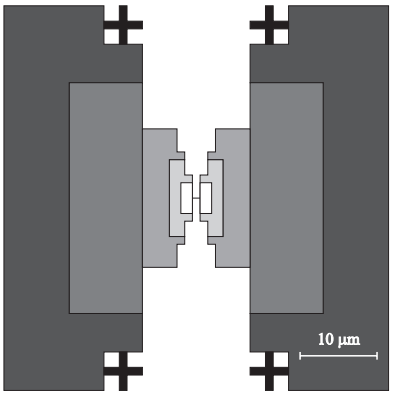

Abbildung 4.7: Dose distribution of the pattern in a 50 μm writing field in order to correct proximity-effect. The innermost area (100 %) has a typical dose of 200 μC/cm^2.

with a probe current of 40 pA, whereas for the large pads written within a 500 μm writing field a probe current of 16 nA was used. In order to enable a second lithography step 8 alignment marks were written. This structure was repeated up to 40 times on the same substrate. The resist was developed in $MiBK : IPA = 1 : 3$ during 45 s. Metal evaporation was performed with the two-angle evaporation technique as described in Section 5.2. First a 15 nm Au-layer was evaporated under normal incidence.

Then for the reservoirs a second 200 nm Au-layer was evaporated at a tilt angle of 30° without breaking the vacuum. This ensures a good contact between the wire and the reservoir. Even larger reservoirs were produced in a second lithographic step in which 1 μm thick Cu layers were aligned over the previous reservoirs. Relevant parameters of the three samples are summarized in Table 4.1.

4.3.3 Noise measurement setup

The lower inset of Fig. 4.8 shows the noise measurement set-up. The sample with resistance R is biased by a current provided by the constant voltage source connected to large series resistors $R_s \gg R$. The voltage over

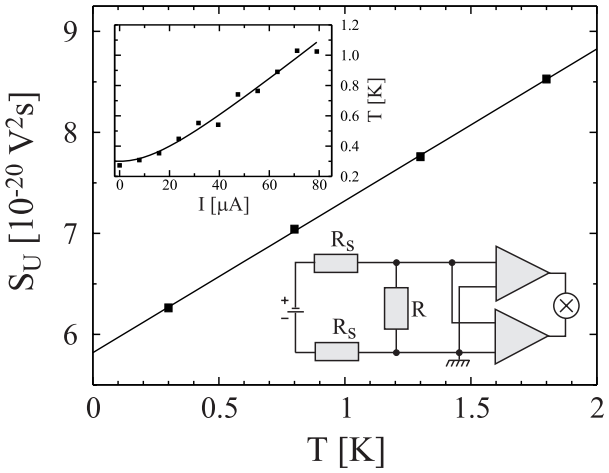

Abbildung 4.8: Thermal noise of sample AI used for the calibration of the noise measurement set-up sketched in the lower inset. The upper inset shows the substrate temperature measured on an additional unbiased monitor wire as a current flows through the sample.

the sample is then amplified with a gain of 1000 by two independent low-noise preamplifiers (EG&G 5184) operated at room temperature. The noise spectrum is obtained by a cross-correlation of the two amplifier signals using a spectrum analyzer (HP 89410A). This correlation scheme effectively removes voltage-offset noise from the preamplifiers [55]. For every data point the signal is averaged over a frequency bandwidth of 70 kHz at a typical center frequency of 300 kHz (at this frequency $1/f$-noise is absent). With a measuring time of 60 s a sensitivity of 10^{-22} V^{2}s for each wire is achieved. As we measure the voltage fluctuations $S_V = S_I \cdot R^2$, the

signal $S_V = \frac{1}{3} 2eV \cdot R$ is proportional to R. We aimed at a precision of 1% at a ratio $eV/kT = 40$, which gives us a lower limit for the sample resistance of $R = 90\ \Omega$. Within the geometrical requirements the typical resistance is however in the range of $10 - 20\ \Omega$. To increase the sample resistance and with it the precision, we use a series of many identical wires, all attached to individual reservoirs. The resistance of each wire was first measured at room temperature to obtain the scattering ΔR around the average resistance $\overline{R}$.

For an absolute noise measurement, a calibration of the complete setup is unavoidable. The measured noise signal is affected by shunt capacitances from the leads in the cryostat which partially diminish the dynamical signal. We calibrate the measured excess noise against the thermal noise of the same sample measured within the same frequency bandwidth. This is done for every sample separately, since the resistance varies from sample to sample. A typical calibration is shown in Fig. 4.8. The thermal noise of the sample varies linearly with temperature T according to $S_U = 4kTR$ with an offset, which arises from current noise of the preamplifiers. Since the resistance R is known from an independent DC-measurement, the slope and offset of the line in Fig. 4.8 provides us with the absolute calibration.

As mentioned above, the substrate heating is determined from the thermal noise of an unbiased monitor wire on the same substrate. A typical measurement is displayed in the upper inset of Fig. 4.8. The dependence of the data could best be accounted for by the phenomenological relation $T_{sub} = \left(T^2 + a \cdot P\right)^{1/2}$. It yields as fit parameter $a = 1.31 \cdot 10^5$ K^2/W, which is specific for the cryostat.

4.4 Results and discussion

We now discuss the experimental results for three different samples which mainly differ in the heat conductance of their reservoirs. In Fig. 4.9 the measured shot noise of the samples (AI, B, AII) is plotted. The solid lines are calculated assuming non-interacting electrons (lower curve, slope 1/3) and interacting electrons (upper curve, slope $\sqrt{3}/4$). Two corrections are included in these theoretical lines: the increased substrate temperature using the parameter a and the relative scattering of the wire resistances around its average $\Delta R/\overline{R}$, which has however only a small influence of around 1%. The relevant sample parameters are summarized in Table 4.1.

Sample AI consists of 28 wires with an average resistance of $\overline{R} = 11.8\ \Omega$ and 200 nm thick Au reservoirs resulting in a reservoir sheet resistance of $R_\square = 42$ mΩ. In Fig. 4.9a the measured noise of this sample as a function of current is shown. Within the accuracy of the experiment, the data points

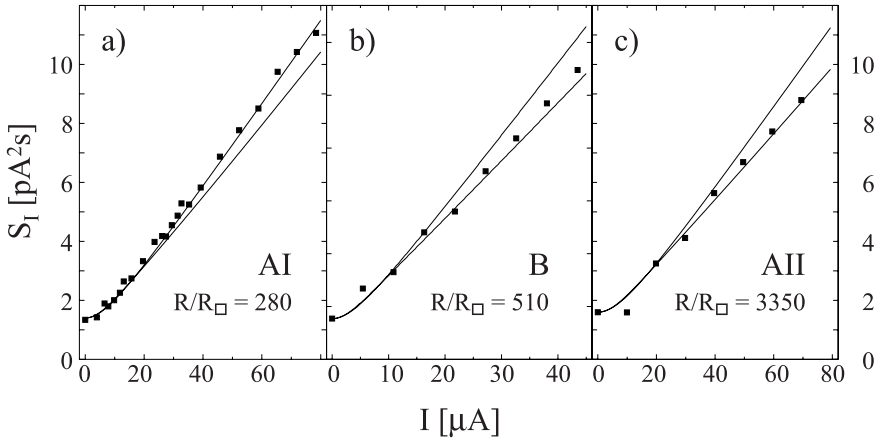

Abbildung 4.9: Shot noise measurements for three different samples with different ratio $R/R_\Box$ at a bath temperature $T_{bath} = 0.3$ K. The upper line corresponds to the prediction of $L \gg l_{e-e}$ (asymptotic slope $\sqrt{3}/4$), the lower one to $L \ll l_{e-e}$ (slope 1/3). The measured noise is significantly increased due to reservoir heating depending on $R/R_\Box$.

lie on the $\sqrt{3}/4$-curve and one may on first sight infer that the length of the wire (910 nm) is much longer than the electron-electron scattering length in contradiction to Eq. (4.24). This conclusion is, however, only valid if reservoir heating is completely absent.

For sample B the same wire length and reservoir thickness are used. Since the wires of this sample are narrower, their resistances R are higher, so that we expect to have less heating as compared to sample AI, since $R_\Box/\overline{R}$ is reduced. As is evident from Fig. 4.9b the measured noise is indeed much lower lying closer to the 1/3-curve than to the $\sqrt{3}/4$-curve. For the highest applied voltage we have $eV/kT \simeq 35$ in both cases.

	R_{tot} [Ω]	#	$\overline{R}$ [Ω]	L [nm]	w [nm]	$R_\Box$ [mΩ]	$(R_\Box/\overline{R})^{1/2}$
AI	329	28	11.8	910	160	42	0.060
B	129	6	21.5	940	100	42	0.044
AII	74.6	8	9.3	910	170	2.8	0.018

Tabelle 4.1: Sample parameters at 0.3 K. Samples AI and B had 200 nm Au reservoirs, whereas for Sample AII an additional layer of 1 μm Cu has been evaporated.

In order to increase $R/R_\square$ even further, we have fabricated thicker reservoirs with a much lower sheet resistance. Sample AII has initially been the same as sample AI, but in a second lithography step a 1 μm thick Cu layer has been evaporated onto the reservoirs in addition to a thin Au layer preventing oxidation of the Cu reservoir (see Fig. 4.10). This reduces the reservoir sheet resistance considerably to 2.8 mΩ. During the second processing of the sample, several wires were lost and only 8 of them remained for the measurement of sample AII. Because of the reduced total resistance R_{tot}, the measured noise voltage is lower, thus increasing the scatter in the data points, but a clear reduction of the slope is visible when comparing with the measurement of sample AI (see Fig. 4.9a and Fig. 4.9c, respectively). The data points are now consistent with the 1/3-prediction.

Since an asymptotic slope of 1/3 is the prediction for the non-interacting electron regime, sample AII has to be in this regime and therefore also AI (same wires), even though the latter displays a significantly increased noise indistinguishable from an asymptotic $\sqrt{3}/4$-slope. Since the wires used for sample B are made from the same material with a similar length, sample B must be in the independent regime as well. All three samples are in the non-interacting regime according to the theoretical estimate given above. However, only for sample AII with the highest conducting reservoirs the measured noise corresponds to the prediction for this regime. For the other two samples additional noise is detected, which increases as $R/R_\square$ becomes smaller.

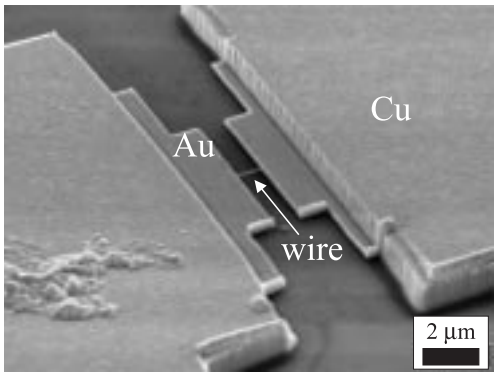

Abbildung 4.10: SEM micrograph of sample AII. The Au wire is terminated by 200 nm thick Au reservoirs. In an overlaid second lithography step an additional layer of 1 μm Cu is evaporated to increase the reservoir thermal conductance.

We explain this increase of noise with electron heat diffusion in the reservoirs. Since we have estimated R_{e-diff} to be the dominant thermal resistance for all reservoirs in this work, we expect from our model, that the temperature of the electrons injected into the wires to vary as

$T_{e,hi} = \left(T_{sub}^2 + b^2 \cdot V^2\right)^{1/2}$ according to Eq. (4.17). Inserting this voltage-dependent temperature into Eq. (4.7) we can treat b as a fit parameter which describes the magnitude of the heating. If our heating model is valid, $b \propto \sqrt{R_\square/R}$. In Fig. 4.11 the fitted values of b are plotted as a function of $\sqrt{R_\square/R}$ for the three samples. Within the error bars it is consistent with the proportionality to $\sqrt{R_\square/R}$ as we have proposed it with our heating model. The plotted line is a least square fit with the assumption that for $\sqrt{R_\square/R} = 0$ (i.e. ideal reservoirs) no heating is present. The values of b are higher by a factor of 1.8 than expected from our model. A higher thermal resistance between electron and phonon temperature R_{e-ph} would scale with $\sqrt{R_\square/R}$ as well. Such a contribution can however be ruled out. Although the relevant parameter , $= 5 \cdot 10^9$ m^{-2}K^{-3}, which was obtained in a 20 nm thick Au film, could be smaller in the reservoir due to a larger diffusion coefficient, such an increase would be negligible. A contribution from a Kapitza resistance would be independent of $R_\square/R$. A calculation using $\sigma_K = 100$ W/m^{2}K^4 would explain in maximum an increase of 22 mK corresponding to a change in b of about 23 K/V, which again is negligible.

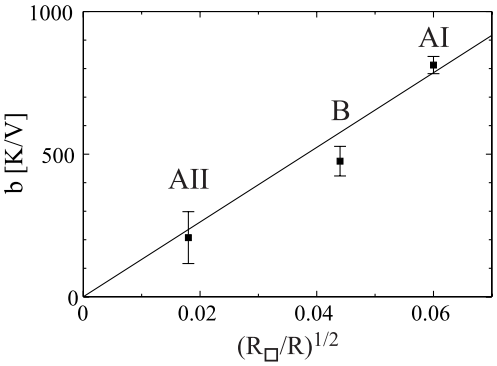

Abbildung 4.11: The parameter b, which describes the enhancement of the measured noise by heating, is extracted from the data of Fig. 4.9. It is proportional to $\sqrt{R_\square/R}$. The origin of the graph corresponds to a slope of 1/3 expected for ideal reservoirs $R_\square = 0$.

In view of the current debate of a possibly enhanced electron-electron interaction, it is important to identify whether the additional shot noise originates from heating or from electron-electron scattering. A possible contribution to the noise arising from electron-electron scattering is however independent of $R_\square/R$ and would thus shift the values of b by a constant offset. From Fig. 4.11 we can estimate such a contribution in our data to be less than 100 K/V corresponding to an increase of $0.01 \cdot 2e\,|I|$ in the asymptotic limit (see below).

The nearly linear dependence of b with $\sqrt{R_\square/R}$ proves that the major

part of the additional noise in our experiment can solely be explained by thermal heating due to a temperature gradient in the reservoir and that the wires are indeed in the non-interacting regime.

Our measurements support experimental results by Schoelkopf *et al.* [51] who compared measured differential noise on short diffusive wires with the interacting and non-interacting theories and found good agreement only for the non-interacting regime, hence the 1/3-theory. These experiments were performed at lower voltages where heating effects are less important (Fig. 4.6). However, the absolute slope of S_I in the asymptotic limit could not be extracted in that work. An absolute value has been reported by Steinbach *et al.* The measured slope was however found to be significantly larger than 1/3. They explained the increase of noise partly by heating and partly by residual electron-electron interactions and proposed to use the shot noise measurement for an independent measurement of the electron-electron interaction in thin metal films. The uncertainty on how large the electron-electron scattering really is, has led to the experiment by H. Pothier *et al.* [52] who directly measured the electron distribution function by tunneling spectroscopy. Based on those results we have estimated the residual contribution from electron-electron scattering in our wires. The only relevant parameter is the ratio of the dwell time of an electron in the wire $\tau_D = L^2/D = 70$ ps to the scattering parameter $\tau_0 = 1$ ns from Ref. [52]. A numerical simulation is used to calculate the electron-distribution function $f(E, x)$ in the wire. Inserting this distribution into Eq. (4.4), we obtain the shot noise which is now slightly larger than $1/3 \cdot 2e\,|I|$ in the asymptotic limit. This increase due to electron-electron scattering is however only of the order of $0.07 \cdot 2e\,|I|$. As mentioned above our data displayed in Fig. 4.11 is not in contradiction, since the error bars would allow for an offset independent of $R_\square/R$ of the order of $0.01 \cdot 2e\,|I|$.

4.5 Conclusion

We have shown, that for a metallic diffusive wire a shot noise power consistent with the universal value $1/3 \cdot 2e\,|I|$ is experimentally obtained in the asymptotic limit $eV \gg kT$ if the reservoirs are designed to minimize a temperature rise as current flows through the wire. This implies that the ratio between wire resistance R and reservoir sheet resistance $R_\square$ should be large, i.e. of the order of 1000 to avoid a large temperature gradient due to electronic heat diffusion from the wire region into the reservoirs. The lateral reservoir size is set by the electron-phonon scattering length. To avoid a difference between the electron and phonon temperatures, the radius of the reservoir should be at least $2l_{e-ph}$. In a very striking man-

ner, our experiment demonstrate that shot-noise reduction factors close to $\sqrt{3}/4$ can be measured in the asymptotic limit even for wires that *must* be in the independent-electron regime! Though we have a hold of the universal $1/3$ noise-suppression factor for diffusive wires in the non-interacting electron regime, another lesson can be drawn from the present experiments: In all highly non-equilibrium electric-transport experiments conducted at low temperatures one has to include the complete environment up to macroscopically large distances. In this respect experiments differ markedly from the approach of a theorist, who can separate the wire from the environment by imposing ideal boundary conditions. However, ideal boundaries (reservoirs) are non-trivial in real experiments!

Kapitel 5

The crossover from $L \ll l_{e-ph}$ to $L \gg l_{e-ph}$

5.1 Introduction

In this chapter the electron heating measured with noise thermometry is described for wires in the range from $L \ll l_{e-ph}$ to $L \gg l_{e-ph}$. The local increase of the electron temperature can be essential already for small currents and is well described by a heat-diffusion equation for the electrons. Depending on the electron thermal conductance and the electron-phonon coupling in the wire, different length regimes are identified. The quantitative knowledge of the electron temperature is important for the analysis of nonequilibrium effects involving current heating in mesoscopic wires.

If an electrical current flows through a mesoscopic wire, the electron temperature rises above the phonon temperature. Especially at low temperatures this increase can be substantial and may influence the measurements of electronic transport properties.

Several methods have been developed to measure the electron temperature. An indirect technique was first used by Giordano [56], who used the temperature dependence of the electrical resistance as a thermometer. Analogously Dorozhkin *et al.* [57] estimated the electron temperature by exploiting the known temperature dependence of the weak localization. A very different technique was used by Molenkamp and de Jong [58], who measured the local electron temperature in a 2DEG quantum wire under dc bias current using the thermopower of a quantum point contact. Another direct tool for the determination of the electron temperature was first implemented by Roukes *et al.* [37] with the use of electric-noise measurements

in the limit $L \gg l_{e-ph}$.

In thermodynamical equilibrium at temperature T, when the time-averaged current I is zero: $S_I = 4kT/R$ (Johnson-Nyquist noise) [11]. Even for $I \neq 0$ the electrons are still in local equilibrium if the wire length L is much larger than the inelastic electron-electron scattering length l_{e-e}. Hence, the electrons still assume a Fermi-Dirac distribution, albeit with a spatially varying electron temperature T_e, which is increased above the phonon temperature T_{ph}. In this hot-electron regime, the noise is determined by the *mean* electron temperature $S_I = 4k\langle T_e\rangle/R$. In the steady state the current heating is balanced by the electronic heat conduction to the contact pads (Fig. 5.1a) and by the heat transfer to the phonon system, which is determined by the electron-phonon scattering length l_{e-ph}. For large applied voltages $V \gg kT_{ph}/e$, two limiting cases can be distinguished: $\langle T_e\rangle$ is either proportional to V if $L \ll l_{e-ph}$ [35] or to $V^{2/5}$ if $L \gg l_{e-ph}$ [37, 54]. In this chapter we bridge the gap between these limiting cases by experiments which are compared to theoretical predictions [31].

5.2 Sample fabrication

Using standard e-beam lithography we fabricated Au-wires with a length ranging from 0.84 μm to 200 μm on oxidized Si-wafers. In a first step a 2 nm Ti-layer was evaporated under a tilt angle of 30° to provide good adhesion for the contact pads. In a second step 20 nm Au were deposited under perpendicular evaporation (Fig. 5.1b). In a third step 200 nm Au were evaporated again under a tilt angle of 30°. The tilt angle of the first and third step was adjusted to the undercut angle of the resist such that no material was deposited in the wire region (Fig. 5.1c). The large, thick Au pads served on the one hand as thermal reservoirs for the electrons and on the other hand as contacts for ultrasonic wire bonding.

The 20 nm thick Au films had a typical sheet resistance of $R_\Box \simeq 1.7\,\Omega$ at 2 K, at which temperature the noise measurements were done. The voltage across the wire was amplified with a gain of 1000 by two independent low-noise preamplifiers (EG&G 5184) operating at room temperature. The noise spectrum was obtained by a cross-correlation of the two amplifier signals using a spectrum analyzer (HP 89410A). For every data point the signal was averaged in a frequency interval of 20 kHz at a typical frequency of 400 kHz where contributions from 1/f-noise and other noise sources can be neglected. The absolute amplitude of the noise signal was calibrated for every wire against thermal noise at zero current and temperatures ranging from 2 K to 10 K. The sensitivity of our measurement set-up for noise is of the order of 10^{-21} V^2s resulting in a precision of 50 mK for a 360 Ω-

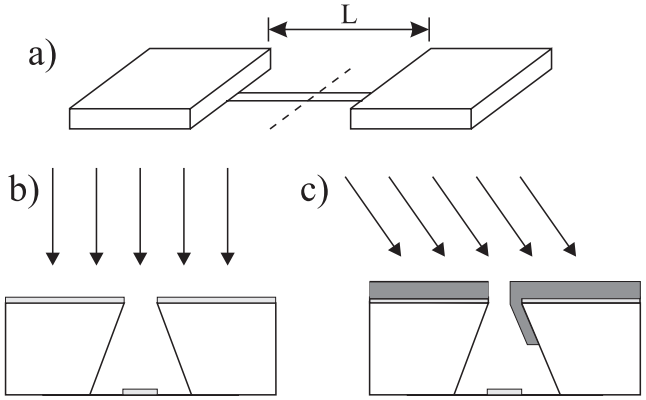

Abbildung 5.1: (a) Schematic of the wire fabricated for noise measurements; (b) perpendicular evaporation of the wire material, (c) evaporation of thick reservoirs under a tilt angle; (b) and (c) are cross sections along the dashed line in (a).

resistor. Since voltage noise is proportional to R, this implies a lower limit for the resistance and for the wire length of about 10 μm for a 50 nm wide Au-wire. To overcome this limit, series of up to 50 equal short wires were fabricated with reservoirs in between (Fig. 5.2) using the angle evaporation technique described above. The noise signal of a single wire is multiplied by the number of wires allowing to measure wires shorter than 1 μm.

5.3 Experiment

Figure 5.3 shows the spectral density of the noise and the corresponding mean electron temperature versus the applied electric field $\mathcal{E}$ for five different samples (A-E) corresponding to a-e. Three of them (A, B, E) are discussed here in detail as they represent three different length regimes. For better comparison of samples with different resistances we have plotted $S_I R = 4k\langle T_e\rangle$. The electric field determines the amount of energy locally transferred to the electron gas. Symbols denote measurement points and solid curves are theoretical fits. Sample A is a 50 μm Au-wire ($L \gg l_{e-ph}$), sample B consists of 5 wires of 10 μm length ($L \simeq l_{e-ph}$) and sample E consists of 30 wires of 0.84 μm length ($L \ll l_{e-ph}$).

The noise behaviour of all these regimes can be quantitatively explained by a nonlinear differential equation, which describes the spatial dependence of the electron temperature in a wire [31]:

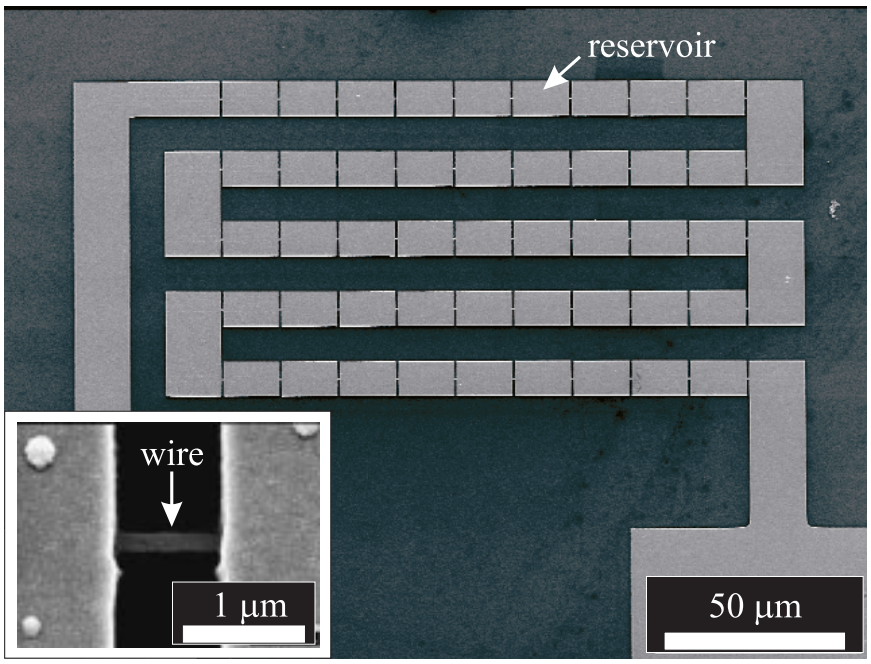

Abbildung 5.2: 50 wires with a length of 840 nm and a width of 140 nm each with large, thick thermal reservoirs in between were fabricated using the technique illustrated in Fig. 5.1. The inset shows one single wire.

$$\frac{\pi^2}{6}\frac{d^2T_e^2}{dx^2} = -\left(\frac{e\mathcal{E}}{k_B}\right)^2 + , \ (T_e^5 - T_{ph}^5), \tag{5.1}$$

where the parameter , is related to the electron-phonon scattering length $l_{e-ph} = 1.31/\sqrt{T_e^3}$, (Ref. [54]). Eq. (5.1) has the form of a heat-diffusion equation. The left hand side describes heat diffusion due to a gradient of T_e, the first term on the right hand side is a source term describing Joule heating, whereas the second term accounts for the heat transfer from the electron to the phonon system due to electron-phonon scattering. The inset of Fig. 5.3 shows the calculated temperature profile along the wire for the three different samples.

For the long wire limit ($L \gg l_{e-ph}$), the influence of the contact pads can be neglected and the electron temperature is nearly constant over the whole wire except close to the reservoirs, where T_e drops to the lattice temperature (inset of Fig. 5.3 upper curve). Therefore the left hand side of Eq. (5.1) can

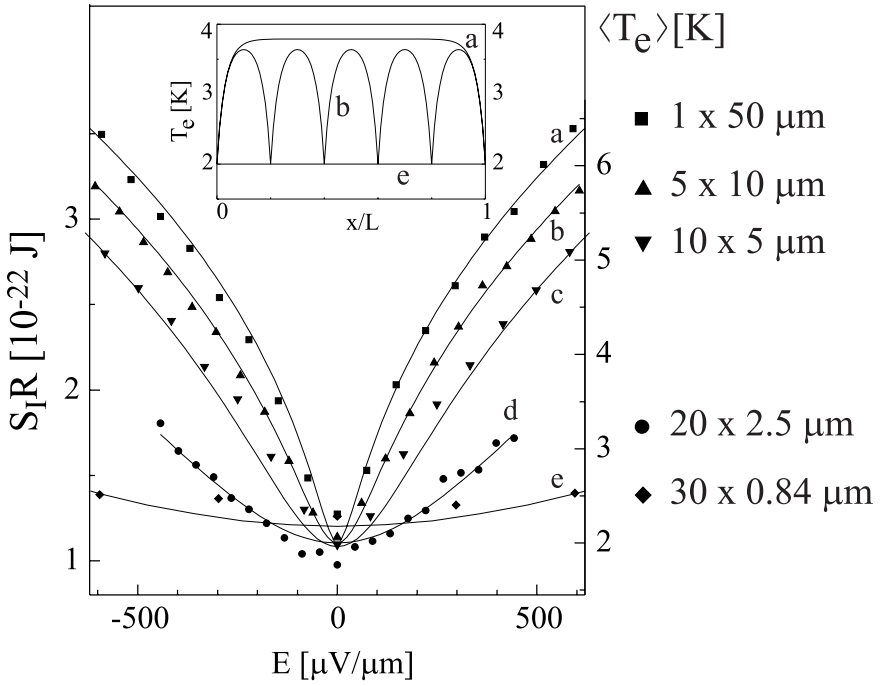

Abbildung 5.3: Measured noise power and corresponding electron temperature versus applied electric field for three different samples. Sample A is a 50 μm long Au-wire ($R = 812\ \Omega$, width $w = 110$ nm), sample B consists of 5 wires of 10 μm length in series ($R = 667\ \Omega$, $w = 120$ nm), sample E consists of 30 wires with a length of 0.84 μm ($R = 300\ \Omega$, $w = 140$ nm). a...e correspond to samples A...E, respectively. The typical current range is 45 μA. The thickness of the Au films is 20 nm, its sheet resistance $R_\Box \simeq 1.7\ \Omega$ at the measuring temperature $T = 2$ K (A,B) and $T = 2.2$ K (E). The solid lines are fits using Eq. (5.1). The inset shows the calculated temperature profiles along the wire for the three different samples for $\mathcal{E} = 160\ \mu\mathrm{V}/\mu\mathrm{m}$.

be omitted for long wires and $S_I = 4k_B(T_{ph}^5 + (e\mathcal{E}/k_B)^2/,)^{1/5}/R$. Using this approximation curve a) was calculated, which shows very good agreement with the experiment. Since for large voltages $T_e \gg T_{ph}$, we obtain the dependence $T_e \propto \mathcal{E}^{2/5}$ in this limit [37]. Even for the comparatively high phonon temperature of 2 K, a current of only 3 μA (corresponding to $\mathcal{E} \simeq$ 50 μV/μm) leads to an increase of T_e of $\simeq 25\%$ above T_{ph}. The heating effect becomes even more pronounced at lower temperatures. For $T_{ph} =$ 0.3 K Eq. (5.1) predicts for sample A a doubling of the mean electron temperature to 0.6 K induced by a current of only 300 nA.

If $L \simeq l_{e-ph}$, the influence of the contact pads can no longer be neglected and leads to a cooling of the electrons close to the reservoirs. In this intermediate regime Eq. (5.1) has to be solved numerically taking into account all the three terms. The reservoirs in a sample with N wires of length L effectively reduce the mean electron temperature compared to a single wire of length $N \times L$ although the overall resistance is the same (inset of Fig. 5.3). This cooling effect is clearly seen when comparing b) with a) in Fig. 5.3. The corresponding theoretical curve was obtained by solving Eq. (5.1) numerically and averaging the electron temperature T_e over the whole wire. The agreement with the experimental data points is again very satisfactory. The fits for samples A and B yield similar values for the electron-phonon coupling parameter: , $\simeq 5 \cdot 10^9$ K^{-3}m^{-2} corresponding to $l_{e-ph} \simeq 7$ μm at 2 K. Our value of , is in agreement with the values for Cu and Ag from Refs. [37, 35].

For sample E (30 wires with 0.84 μm length) the cooling of the reservoirs is so effective that nearly no heating takes place for the electric fields shown in Fig. 5.3. Nevertheless, T_e^2 varies along the wire and assumes a parabolic shape. Since $L \ll l_{e-ph}$ for each individual wire, the second term on the right hand side of Eq. (5.1) can be neglected and one obtains after spatial averaging:

$$S_I = (2k_B T_{ph}/R)(1 + (\nu + 1/\nu)\arctan\nu), \tag{5.2}$$

where $\nu = \sqrt{3}eV/2\pi k_B T_{ph}$. This leads to $S_I = (\sqrt{3}/4)2eI$, i.e. $\langle T_e \rangle \propto V$, for $eV \gg k_B T_{ph}$.

Sample C (5 μm wire length) and sample D (2.5 μm wire length) are further examples for the regime $L \sim l_{e-ph}$ and confirm the smooth crossover from $L \sim l_{e-ph}$ to $L \ll l_{e-ph}$ or the increase of the cooling power of the reservoir for decreasing wire length.

The measured noise for sample E in a wider current interval is shown in Fig. 5.4. The size of the squares represents the measurement accuracy. As expected for $eV \gg k_B T_{ph}$ a roughly linear variation of S_I is found at higher currents. For lower currents S_I rounds off and approaches the equilibrium thermal noise. The whole current range is accurately described

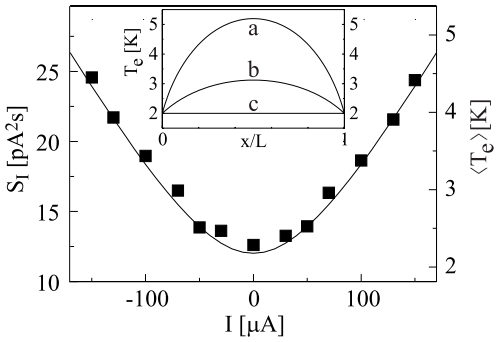

Abbildung 5.4: Noise measurement of sample E of Fig. 5.3 (30 wires in series with a length of 840 nm). The solid line is the prediction of Eq. (5.2), which has no adjustable fit parameter. The inset shows the temperature profile of a single wire for 0, 75 and 150 μA (from bottom to top).

by Eq. (5.2), which contains no adjustable fit parameters. This proves that electron-phonon scattering can be neglected in a metallic wire of this length at 2 K. The curves a, b and c of the inset show the calculated temperature profiles for 150, 75 and 0 μA, respectively.

5.4 Conclusion

In conclusion, we have demonstrated that noise measurements are a powerful tool to obtain information on electron heating effects in narrow metal wires. The measured electron temperatures are in excellent agreement with model calculations for all wire lengths ranging from $L \gg l_{e-ph}$ to $L \ll l_{e-ph}$. The experiments demonstrate, that electron heating depends crucially on the length of the wires and the presence of thermal reservoirs. Hence, our results have important implications for the sample layout of electric microcircuits at low temperatures.

Kapitel 6

Disorder dependence of electron-phonon scattering

6.1 Theory

Up to now we have assumed that for $T = 0$ the power transferred from the electron to the phonon system is proportional to T_e^5, corresponding to a behaviour $T_e \propto E^{2/5}$. As can be seen in Fig. 5.3 curve a, there are small, but significant deviations in the measured electron temperature from the theoretical $E^{2/5}$-curve. The data points at low electric fields are below the fitted curve, whereas those for high electric fields are above it. A $E^{0.45}$-relation would best describe these data. The deviations however are small compared to the cooling of the electrons for wires with $L \leq l_{e-ph}$, therefore the deviations considered here are not relevant for the main message of Chapter 5.

The power law $P \propto T^5$ is based on the T^3-dependence of the electron-phonon scattering rate τ_{e-ph}^{-1}, which is the case for a three-dimensional phonon gas in the clean limit at $T \ll \Theta_D$ [60]. In order to account for other possible power laws, we will use in the following the general expression $\tau_{e-ph}^{-1} \propto T^p$. The energy per volume needed to heat the electron system by a temperature difference dT is $dQ = C_e dT$ where $C_e = \frac{\pi^2}{3} k_B^2 N(\epsilon_F) \cdot T_e$ is the electronic specific heat, with $N(\epsilon_F)$ the density of states at the Fermi energy. This energy decays with a rate τ_{e-ph}^{-1}. The power dP needed to

raise the electron temperature by dT is then given by:

$$dP = \tau_{e-ph}^{-1} \cdot C_e \cdot dT. \tag{6.1}$$

The total power required to sustain an out-of-equilibrium situation with $T_e > T_{ph}$ is therefore:

$$P(T_e) - P(T_{ph}) := \int_{T_{ph}}^{T_e} \tau_{e-ph}^{-1} C_e dT \propto \int_{T_{ph}}^{T_e} T^{p+1} dT \propto (T_e^{p+2} - T_{ph}^{p+2}). \tag{6.2}$$

For $T_e \gg T_{ph}$ the dependence of the electron temperature on the electric field is therefore $T_e \propto E^{2/(p+2)}$. This proportionality can also be obtained by a different consideration [61]: the mean energy per scattering process transferred from an electron to the phonon gas is of the order of kT_e and must equal the mean energy gained due to the electric field between two electron-phonon scattering events: $kT_e \simeq eEl_{e-ph}$, where $l_{e-ph} = \sqrt{D\tau_{e-ph}}$ is the electron-phonon scattering length, from which the same relation $T_e \propto E^{2/(p+2)}$ is obtained. From our empirically deduced $E^{0.45}$-relation we can extract the exponent describing our data best to be $p = 2.5$.

Deviations from the clean limit prediction $p = 3$ have been a topic in the 80s and 90s, when people started to conduct electron heating experiments in small disordered films. The clean limit is defined by an the elastic scattering length l_e much larger than λ_T, the wavelength of a phonon with energy kT. In this case, the probability that an electron scatters elastically between two electron-phonon scattering events is small and the electron trajectory can therefore be viewed as ballistical. In the opposite limit, when $l_e \ll \lambda_T$, the electron's motion is diffusive (dirty limit). With the use of $q_T = 2\pi/\lambda_T$ as the wave vector of a phonon with energy kT, we can define the clean limit as $q_T l_e \gg 1$ and the dirty limit as $q_T l_e \ll 1$. Metallic bulk samples, especially at high temperatures, are indeed in the clean limit, but for most thin metal films at cryogenic temperatures $q_T l_e \simeq 1$. In the dirty limit the influence of electrons scattering with transversal phonons has to be taken into account, a process which is completely absent in the clean limit. A calculation including disorder has been made by Schmid *et al.* [62]. The result is a correction factor from the T^3-dependence of τ_{e-ph}^{-1} in the clean limit defined by $B(q_T l_e) = \tau_{e-ph}^{-1}/T^3$ (see Fig. 6.1). This factor reaches a constant value for $q_T l_e \gg 1$ consistent with the relation $\tau_{e-ph}^{-1} \propto T^3$ for the clean limit. In the dirty limit, however, B is proportional to $q_T l_e$ and since $q_T \propto T$ a T^4-behaviour of the electron-phonon scattering rate is expected. If $q_T l_e$ is of order unity, B decreases with increasing $q_T l_e$ resulting in an exponent $p \simeq 2.5$.

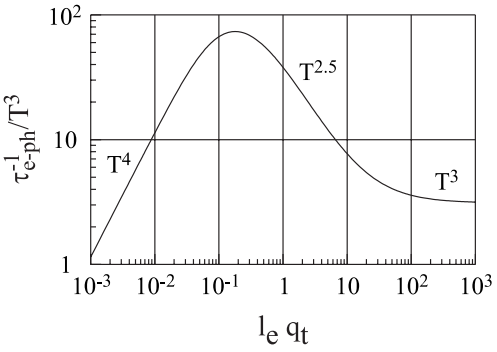

Abbildung 6.1: Electron-phonon scattering rate as a function of $q_T l_e$,which is the wavevector of a phonon with energy kT multiplied with the mean free path and is varied over 6 orders of magnitude in the plot.

Although several experiments have been conducted in order to verify this theory, a clear confirmation is still lacking. Nearly all the experiments aiming to determine τ_{e-ph}^{-1} measured the power needed to establish the non-equilibrium $T_e > T_{ph}$, which is now given by:

$$P(T_e) - P(T_{ph}) = \int_{T_{ph}}^{T_e} B(T, l_e) T^3 C_e dT. \tag{6.3}$$

Three different techniques were mainly used to determine the electron temperature: a direct method using noise thermometry [37, 54], and two indirect methods using the temperature-dependence of weak-localization [57, 63, 64, 65] or of the resistance [66, 67, 68, 69]. Except for Refs. [54, 57, 67] a possible increase of the phonon temperature due to the power dissipation in the wire has not been considered. Like in Subsection 4.2.2 we can construct a heat-chain model where the power V^2/R, which is transferred from the electron gas into the phonon system via the heat resistance R_{e-ph}, has to flow into the substrate over a possible Kapitza resistance R_K (see Fig. 6.2). In order to study electron-phonon scattering, we need $R_K \ll R_{e-ph}$, such that the phonon temperature does not increase significantly when raising the electron temperature. In the opposite limit $R_K \gg R_{e-ph}$, the phonon temperature is nearly as high as the electron temperature and the measured $T_e(E)$-curve is mainly determined by the Kapitza resistance. With the use of Eq. (4.14) we expect a $P \propto T_e^4$-behaviour in the latter case pretending an exponent $p = 2$ independent of the real temperature dependence of electron-phonon scattering. For $R_K \simeq R_{e-ph}$ the measured exponent lies between 2 and the real unknown p. The measured values for p in all the experiments performed range from $p = 2$ to $p = 3$ in agreement with the previous considerations, but a confirmation of the proposed disorder dependence is still lacking, since the phonon temperature in all these experiments

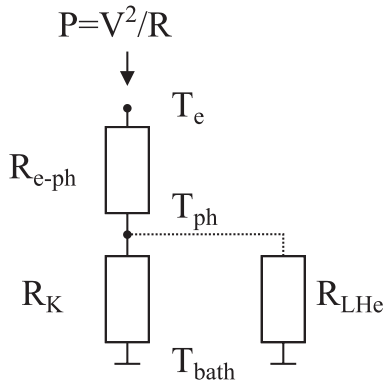

Abbildung 6.2: Schematics that shows how the power P produced in the wire is transferred from the electrons at temperature T_e first into the phonon system at temperature T_{ph}, before it reaches the substrate at T_{bath}. If the experiment is done below 2.17 K, a superfluid helium film transfers the power from the phonons into the bath.

has not been known.

6.2 Experiments

In order to check the prediction of Schmid we have performed heating experiments on metallic wires with varying film thickness, which determines the size of the grains and therefore the elastic scattering length. The parameter $q_T l_e$ could further be varied by increasing the electron temperature. Since phonons with an energy of the order of kT_e are emitted in the non-equilibrium, T_e is the relevant temperature that enters q_T.

Fig. 6.3 shows typical heating curves for a 15 nm thick Au wire measured in the He-4 cryostat. The shape of the curves for a bath temperature of 3 K,

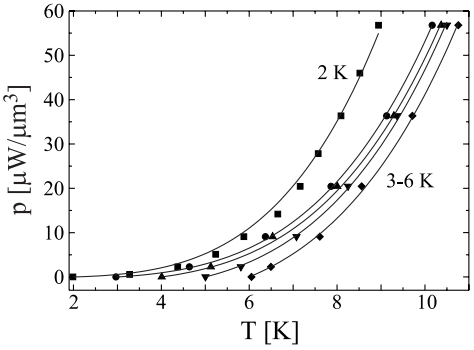

Abbildung 6.3: Power per volume necessary to elevate the electron temperature for a 60 μm long and 15 nm thick Au wire. A significant difference is seen for a bath temperature of 2 K, compared to $3-6$ K.

4 K, 5 K and 6 K is identical and are only shifted by an offset power $P(T_{ph})$, which is consistent with the expected dependence of Eq. (6.2) $P = P(T_e) - P(T_{ph})$. The curve at bath temperature of 2 K differs significantly. For the same power the electron temperature is much smaller in this case than for a larger bath temperature. We explain this effect with an additional cooling channel for the phonons (Fig. 6.2) provided by a film of superfluid He-4, which covers all the surfaces in the VTI, if the temperature is below the λ-point of He-4: $T_\lambda = 2.17$ K. For $3 - 6$ K, where only exchange gas is in the VTI, the phonon temperature rises therefore significantly above the bath temperature. For this case the curves can be fitted with $P \propto T^4$, showing that the major part of the temperature difference is over the Kapitza resistance. The same $P \propto T^4$-behaviour is found for a 20 nm thick Au wire measured in the He-3 cryostat, where the sample is in vacuum (Fig. 6.4). Since these measurements are subject to an increase in phonon temperature in the wire, which could not be measured, no conclusions can be drawn from them. Also for a bath temperature of 2 K the exact phonon temperature is not known. However the cooling power of the superfluid He-4 film leads to a clearly reduced phonon and hence also electron temperature. If the increase of T_{ph} above T_{bath} is not so dramatic, say only of the order of $T_e/2$, it can be neglected due to the high power of T^{p+2}. The curve obtained at 2 K can best be fitted with $p = 2.5$, which would be consistent with the prediction of disorder-dependent electron-phonon scattering as proposed in Ref. [62] for $q_T l_e = 1 - 10$, in which range the sample actually is at the measured electron temperatures.

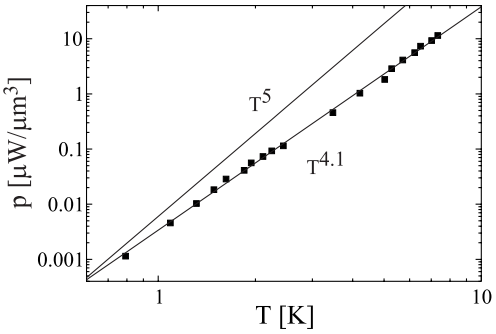

Abbildung 6.4: Power density required to elevate the electron temperature for a 200 μm long Au wire at a bath temperature of 0.3 K. The lower solid line is a least square fit yielding an exponent of 4.1.

A plot of the measurements for 6 wires, all measured at 2 K in the He-4 cryostat, is shown in Fig. 6.5. The sample parameters are collected in Table 6.1. The elastic scattering length l_e varies over nearly one order of magnitude. For every measurement point p/T^5 is plotted as a function of $q_T l_e$. It corresponds to the electron-phonon coupling strength and would

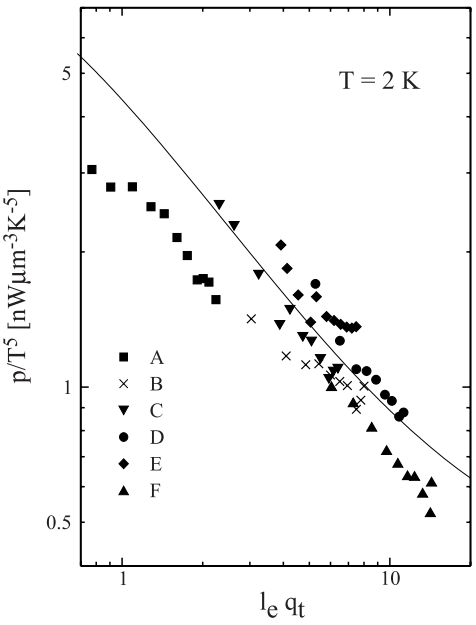

Abbildung 6.5: Electron-phonon interaction for six different samples as a function of the disorder parameter lq_t. The solid line is calculated assuming a disorder-dependent electron-phonon coupling with the use of Eq. (6.3). The offset of this line represents the absolute strength of the coupling and can vary from sample to sample.

be constant in the clean limit (p=3). All the wires separately however show a decreasing behaviour as a function of $q_T l_e$. The plotted solid line is calculated assuming disorder dependent electron-phonon scattering [62] using Eq. (6.3) and corresponds to the decaying part of $B(q_T l_e)$. To calculate the power the integral of Eq. (6.2) has to be evaluated by inserting the disorder dependent expression for τ_{e-ph}^{-1} [70]. Furthermore a comparison of the wires among each other shows that those with smaller l_e have a higher coupling strength. Therefore the wires can be described here nearly by one single universal curve independent of disorder and electron temperature.

Sample	Material	$l_e[nm]$	$t[nm]$	$L[\mu m]$	$w[nm]$	$\rho[\mu\Omega \cdot cm]$
A	AuFe	8.9	22	200	1130	11.1
B	Au	20	15	60	115	5.0
C	Au	26	20	150	450	4.0
D	Au	34	25	60	90	2.9
E	AuFe	44	32	1400	570	2.3
F	Au	63	30	450	210	1.59

Tabelle 6.1: Sample parameters at 2 K.

Our data are therefore in agreement with the theory of disorder-dependent electron-phonon scattering described in Ref. [62]. For a clear confirmation however a measurement of the phonon temperature is needed.

To get a rough estimate of the phonon heating in the vicinity of the wire, we have performed an experiment with two parallel wires with a distance of 380 nm apart from each other. While one of the wires is heated, the electron temperature of the unbiased wire, and thus its phonon temperature, is measured via noise thermometry. Such an experiment showed that the increase of the substrate temperature can be neglected, nevertheless it cannot be excluded that the phonons in the wire are at an even higher temperature.

6.3 Outlook

A possible concept to really measure T_{ph} in the wire is proposed here: Two wires have to be evaporated on each other with an insulating layer in-between. As the lower wire is heated, the phonon temperature of both wires are the same and also equals the electron temperature of the upper wire, which can then be determined again by noise thermometry. This method was used in Ref. [57] for two large films, the temperature was thereby measured using the temperature dependence of weak localization. This experiment has still to be performed for wires using noise as a thermometer.

Recently Zhong and Lin [71] have measured the electron-phonon scattering rate in the equilibrium case using weak localization and found a relation $\tau_{e-ph}^{-1} \propto lT^2$ for very disordered samples ($q_T l_e \simeq 10^{-1}$). The proportionality to l is in agreement with the theory of Schmid, however a T^4-power law is expected as a temperature dependence. Therefore it is also possible that the disorder dependence of electron-phonon scattering cannot be described by the single parameter $q_T l_e$.

Kapitel 7

Size dependent thermopower in mesoscopic AuFe spin glass wires

7.1 Introduction

This chapter reports on how noise thermometry is successfully used as a tool to measure the electron temperature in a heated wire. With this technique the thermopower of narrow AuFe spin glass wires is determined, which are thermally coupled at one end to the heated wire.

The scattering of conduction electrons at transition metal impurity spins (e.g. Fe, Cr, Mn) substantially alters the low temperature properties of noble metals (e.g. Au, Ag, Cu) [72]. For small concentrations ($\sim$ 100 ppm) of the magnetic dopant the Kondo effect gives rise to a logarithmic increase of the resistivity $\rho(T)$. Below the Kondo temperature T_K a compensation cloud of conduction electrons is formed around the impurity spins which gradually cancels their magnetic moment. At higher concentrations ($\sim$ 1at.%) the Ruderman-Kittel-Kasuya-Yosida (RKKY) interaction between the randomly distributed impurity spins competes with the Kondo effect and causes a freezing of the impurity spins into a disordered configuration called a spin glass. This is reflected by the appearance of a typical broad maximum in $\rho(T)$ since the spin scattering rate again decreases at the lowest temperatures due to the freezing process.

Recent experimental work has addressed the existence and relevance of intrinsic length scales for both the Kondo effect and the spin glass freezing process [73, 74, 75, 76, 77]. The results have so far been controversial: While some groups [73, 74] report a pronounced depression of the Kondo slope with decreasing film thickness and wire width, other authors claim that the observed size effects are small and can moreover be explained quantitatively in terms of disorder enhanced electron-electron interaction effects [76, 77]. It was also noted that structural disorder may have an important influence on the spin dependent part of the resistivity for Kondo alloys [78] as well as for more concentrated spin glass alloys where a damping of the RKKY interaction occurs [77, 79].

Theoretical calculations have shown that in the single impurity limit spin-orbit interactions can induce a size dependent magnetic anisotropy which results in a size dependent resistivity [80]. For more disordered samples, an interplay between weak localization and the Kondo effect has been predicted which can account for both a disorder effect and a size effect [81]. In order to address the open questions related to the size effects, it is obviously interesting to look at other transport properties which are affected by the spin scattering. An excellent candidate is the thermoelectric power (TEP), $S(T)$, which is known to be strongly enhanced in dilute magnetic alloys. While in bulk Au $S(T)$ is positive and small [82], it switches sign upon adding Fe impurities and its absolute value can be as high as 15 μV/K. Further increase of the Fe concentration into the spin glass regime again reduces $|S(T)|$ [83].

Up to now, reliable measurements of $S(T)$ could not be performed for mesoscopic samples. In this chapter, we present the first quantitative measurements of $S(T)$ in mesoscopic AuFe wires. Our measuring technique is based on current induced electron heating to produce the necessary thermal gradients and noise thermometry for a direct measurement of the electron temperature. We observe a clear reduction of $|S(T)|$ when the width of the AuFe wires is reduced from 300 down to 100 nm. Our measurements allow to directly test the theoretical models which link the size dependence to a surface induced magnetic anisotropy [80]. Previous experiments on mesoscopic AuFe wires revealed a pronounced asymmetry of the differential resistance as a function of the heating current [84] which is absent in pure Au and can be traced back to the enhanced thermoelectric power of the AuFe [85]. However, the functional dependence of the TEP on size and temperature could not be determined so far.

7.2 Experiment

The samples consist of pairs of AuFe wires of different width (forming thermocouples) connected at one end to a meandric wire which serves as a heater with resistance R_H (see Fig. 7.1). The electron temperature T_H in the heater is raised above the substrate temperature T_S when a dc current I flows through the heater. The other ends of the thermocouple wires are connected to large contact pads which are assumed to remain at T_S.

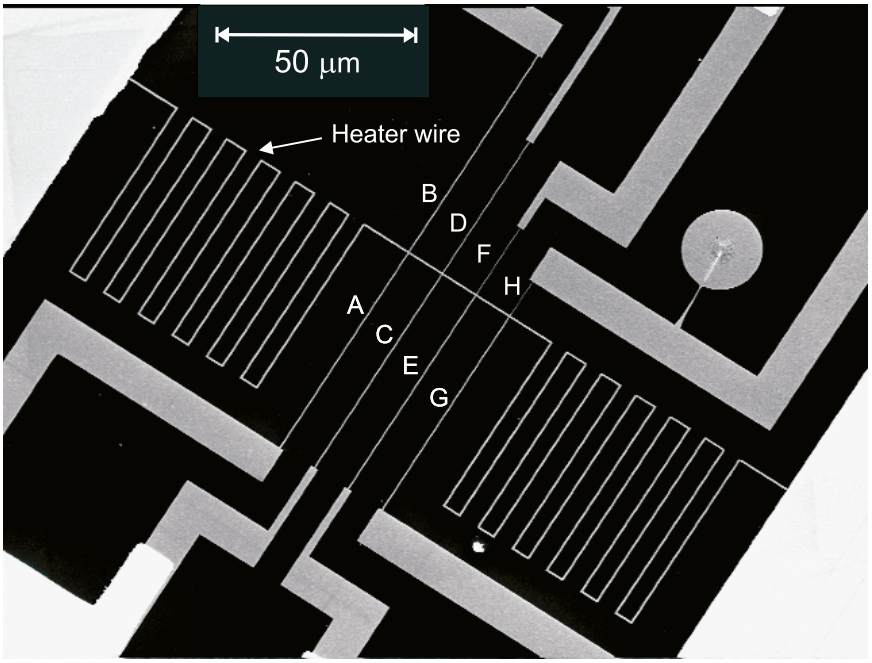

Abbildung 7.1: Scanning electron micrograph of a typical sample. The four different thermocouples are labelled AB, CD, EF, and GH.

The wires A, C, E, G on one side of the 510 nm wide heater have the same nominal width of 300 $\pm$ 15 nm and serve as a reference to detect small changes of the thermopower when varying the width of the wires labelled B, D, F, H on the other side. The latter wires have a width w of 305, 220, 140, and 105 nm, respectively, and their length increases with increasing w to keep the thermal conductance of all wires constant. The length of the narrowest wires as well as the distance between the junctions is 10 μm while the total length of the meandric heater is 1.4 mm. This geometry provides a nearly flat profile of T_H along the heater except at both ends of

the heater close to the large contact pads (see Chapter 5). We note that – regardless of the temperature profile in the sample – in the absence of a size effect in $S(T)$ no thermovoltages are expected to develop across our mesoscopic thermocouples made entirely from AuFe.

The samples have been prepared by electron beam lithography and evaporation of 99.999% pure Au. In a second step Fe ions have been implanted at several energies to provide a reasonably constant doping profile perpendicular to the film [76]. Two series of samples were prepared having nominal Fe concentrations of 50 and 3000 ppm, respectively. Prior to implantation, the 30 nm thick films had a sheet resistance $R_\Box$ of 0.3 Ω at 4.2 K. After implantation $R_\Box$ of the 50 ppm Kondo samples remained unchanged while $R_\Box$ of the 3000 ppm spin glass samples increased to 0.7 Ω. This corresponds to an elastic mean free path l_e of 90 and 40 nm, respectively. SEM and AFM images indicate that the films are polycrystalline with a grain size (20-30 nm) considerably smaller than the wire width. We emphasize that the size dependence, which we will report in this Letter, cannot be explained by a simple disorder effect since all wires are prepared simultaneously, resulting in a value of l_e which is independent of the wire width. Most of the measurements have been performed in a ^{3}He cryostat at a bath temperature of 300 mK.

The idea of our thermopower experiment is the following: If a current I is sent through the heater wire the electron temperature in the heater rises above the substrate temperature T_S. The temperature at the thermocouple junctions T_J will be slightly lower than the average temperature of the heater T_H because of the finite thermal conductance of the thermocouple wires. The resulting thermoelectric voltage across the thermocouples will be symmetric in I since $T_J(I)$ is symmetric in I:

$$V_{th}(I) = \int_{T_S(I)}^{T_J(I)} \Delta S(T) dT \quad , \tag{7.1}$$

where $\Delta S(T) = S_{wide}(T) - S_{narrow}(T)$ is the thermopower difference between the wide and narrow wire of the thermocouple. In order to increase the sensitivity of our measurements, we measure the differential resistance dV/dI rather than $V(I)$ across our thermocouples. Since $V_{th}(I)$ is symmetric in I, dV/dI will predominantly be antisymmetric in I. According to Eq. (7.1), the antisymmetric part of dV/dI is directly linked to $\Delta S(T)$:

$$\frac{dV_{th}}{dI} = \Delta S(T_J)\frac{dT_J}{dI} - \Delta S(T_S)\frac{dT_S}{dI} \quad . \tag{7.2}$$

The second term in Eq. (7.2) represents the contribution of the also elevated substrate temperature T_S at higher currents. To extract $\Delta S(T)$, Eq. (7.2)

has to be solved selfconsistently. Similar cross-shaped geometries have been used to measure mesoscopic TEP fluctuations in GaAs quantum wires [86] and the TEP of quantum point contacts [87]. However, in these experiments the electron temperature has not been measured independently.

The average temperature in the heater wire $T_H(I)$ has been determined by measuring the thermal noise $S_U = 4k_B\langle T_H(I)\rangle R_H$ of the heater wire as a function of current bias [36]. For typical heater resistances R_H of 1-2 kΩ the electron temperature could be determined with an accuracy of about 50 mK. With a heating current of 80 μA electron temperatures up to 4 K have been achieved. Figure 7.2 shows an example of $T_H(I)$ for the 3000 ppm sample together with a fit corresponding to the semi-empirical form $T_H(I) = (aI^2 + T_0^b)^{1/b}$, where $T_0 = 0.3$ K is the temperature of the sample stage. The parameters for the best fit were $a = 0.0386$ K$^b/\mu$A^2 and

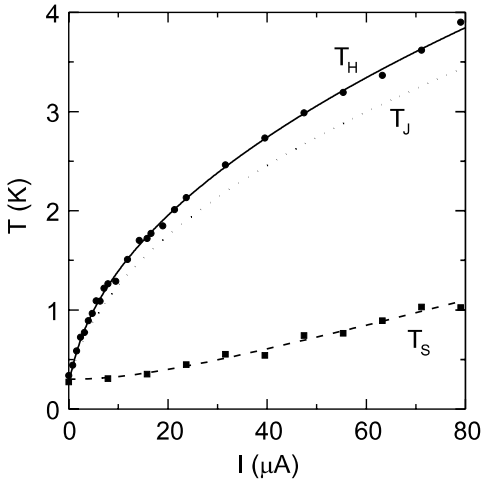

Abbildung 7.2: Electron temperatures $T_H(I)$ of the heater and $T_S(I)$ of the substrate monitor wire together with fits as described in the text. The dotted line corresponds to a value of $a = 0.0247$ K$^b/\mu$A^2 and indicates the temperature $T_J(I)$ at the thermocouple junctions.

$b = 4.1$. The exponent b is in agreement with the heating measurements performed on a 200 μm Au-wire in the He-3 cryostat (Section 6.2). From Figure 7.2 we can deduce $l_{e-ph} \simeq 200$ μm at an electron temperature of 0.3 K, which is small compared to the wire length $L = 1400$ μm. At elevated electron temperatures l_{e-ph} further decreases, hence we are for certain in the regime $L \gg l_{e-ph}$. Therefore T_e is constant over nearly the whole wire length, meaning that the measured average heater temperature $\langle T_H\rangle$ equals the temperature in the middle of the wire.

The temperature at the junction $T_J(I)$ has been determined by a numerical solution of the heat diffusion equation based on Ref. [31]. The calculation uses the measured $T_H(I)$ curve to take into account the cool-

ing through the electron-phonon scattering and the result is indicated by the dotted line in Fig. 7.2. A comparison of the current dependence of the resistivity for the different sections of the heater wire confirms that the local reduction of T_H remains smaller than 10 %. For the highest currents a power of $\simeq 10$ μW is dissipated in the heater, which is sufficient to also raise the substrate temperature up to $T_S \simeq 1$ K. The open symbols in Fig. 7.2 show T_S measured on an independent Au wire patterned close to the AuFe sample while current is sent through the heater wire. The dashed line is a fit of the form $T_S = \sqrt{a'I^2 + T_0^2}$ with $a' = 0.00017$ K$^2/\mu$A^2. This functional dependence is expected since the thermal coupling between the sample stage of the cryostat and the substrate is metallic with a thermal conductance depending linearly on temperature.

7.3 Results and discussion

In order to detect the response of the thermocouples a small ac current of 1 μA and 116 Hz is added to the dc heating current I and the corresponding ac voltage is detected with a lock-in amplifier. We first measured in detail the dV/dI signal for the 50 ppm thermocouples. As shown in the inset of Fig. 7.3, the thermocouple EF clearly reveals the presence of a signal which is antisymmetric in I and is of the order of 1 mΩ. The antisymmetric signal increases when the difference in width Δw increases, which can be linked to a decrease of the thermopower in the narrower AuFe wires. According to the Gorter-Nordheim rule [82] the measured TEP in our Kondo samples is strongly reduced by the non-magnetic scattering. The reduction factor is equal to the ratio of the total resistivity ρ_{tot} and the resistivity contribution ρ_{Fe} [88] of the Fe impurities. Relying on the reported resistivity ρ_{Fe} for bulk samples [72, 89], we estimate $\rho_{tot}/\rho_{Fe} \simeq 12$. According to Eq. (7.2) and the available data for the thermopower in bulk Kondo alloys [83] we find that for the thermocouple EF the observed thermopower signal $\Delta S(T)$ is of the order of 6% of the bulk thermopower. Unfortunately, the poor signal to noise ratio for our Kondo samples does not allow to draw more quantitative conclusions concerning the width dependence of the thermopower.

For the 3000 ppm samples a comparison with the data for bulk alloys [72, 89] indicates that $\rho_{tot} \simeq \rho_{Fe}$ for our relatively clean samples. Consequently, the thermoelectric voltages are considerably larger than for the Kondo samples and a quantitative data analysis becomes possible. Figure 7.3 shows the antisymmetric part of the dV/dI signal from the thermocouples AB, CD, EF, and GH, respectively (see Fig. 7.1). For the thermocouple GH which has the largest difference in width Δw, dV/dI rises very sharply from zero, shows a maximum around 7 μA and slowly decreases for

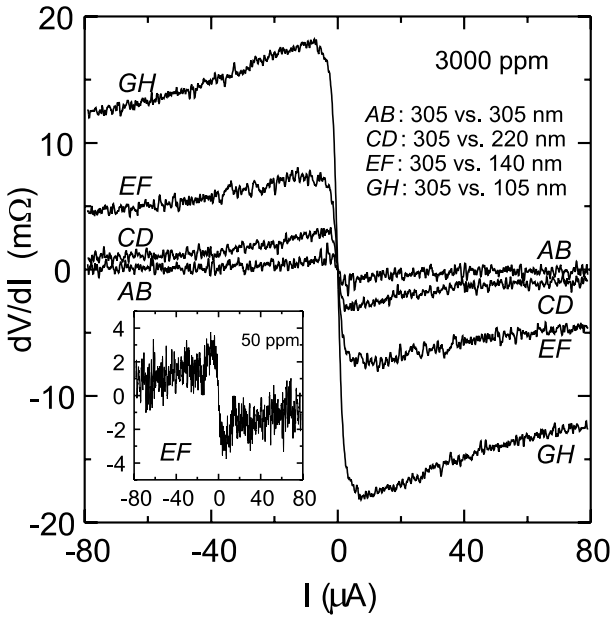

Abbildung 7.3: Antisymmetric part of the differential resistance for the different thermocouples. Voltage contact V_+ was connected to one of the reference wires *A, C, E, G* (nominal $w = 300$ nm) while V_- was connected to one of the narrow wires *B, D, F, H* ($w = 305$, 220, 140, and 105 nm, respectively). Trace *AB* is an average of several 300/300 nm combinations. Inset: Asymmetric part of dV/dI for thermocouple *EF* of a sample with 50 ppm Fe.

higher currents. For decreasing Δw in the thermocouples *EF* and *CD* the asymmetry is systematically reduced while the overall shape of the dV/dI signal remains similar. For the thermocouple *AB*, where Δw is nominally zero, a residual small asymmetry is observed which is of random sign for different samples and can be attributed to small size differences related to imperfections of the lithographic patterning.

In Fig. 7.4 we have plotted the temperature dependence of $\Delta S(T)$ for the different 3000 ppm thermocouples according to Eq. (7.2). For the Kondo as well as for the spin glass samples $\Delta S(T) = S_{wide} - S_{narrow}$ is negative, implying that $|S(T)|$ becomes smaller when reducing the width of the wires. For the 3000 ppm data (see Fig. 7.4) $\Delta S(T)$ displays a nearly linear variation above 1.5 K which is close to the spin glass freezing temperature T_f for 3000 ppm [72]. The inset of Fig. 7.4 shows $|d\Delta S(T)/dT|$

for the linear regime as a function of the width of the narrower wire of the thermocouples. At lower temperatures $|\Delta S(T)|$ decreases more rapidly and is nearly zero at 0.4 K. The measured values of $|\Delta S(T)|$ range up to 0.8 μV/K which should be compared with the value $|S(T)| \simeq 7\mu$V/K observed for bulk AuFe samples with a comparable Fe concentration [83]. On the other hand, the thermoelectric voltages become very small when both wires forming the thermocouples are wider than 300 nm. We therefore conclude that for Kondo as well as for spin glass AuFe wires the thermopower is significantly reduced when reducing the width down to 100 nm.

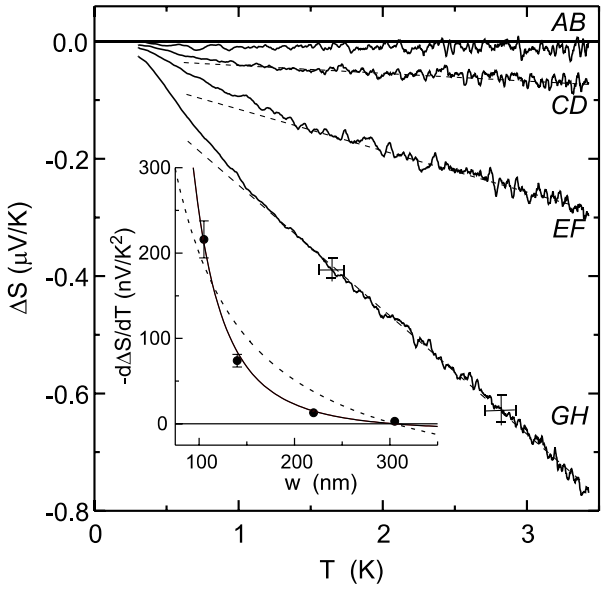

Abbildung 7.4: Difference in thermopower as function of temperature for varying difference in wire width. The dashed lines illustrate the linear behavior ot $\Delta S(T)$ above 1.5 K. The error bars indicate the uncertainty introduced by the correction of the temperature profile. Inset: Slope of $|\Delta S(T)|$ at $T = 3$ K as a function of the width of the narrow wire. The lines are best fits of a $1/w^3$ (solid) and a $1/w$ (dashed) dependence.

What is the origin of the size dependence? We have checked that the asymmetric dV/dI is absent in undoped samples. For the more dilute alloys (≤ 500 ppm) a magnetic field of 17 T completely suppresses the asymmetry. This proves that the observed thermoelectric voltages are indeed related to the magnetic scattering. Since the size effects are also present in the Kondo

samples, it is reasonable to link them to a single impurity effect along the lines of Refs. [80, 81]. For relatively high temperatures $T \geq T_f$, a considerable fraction of the magnetic impurity spins is still free to flip independently in the more concentrated spin glass wires and are therefore expected to be sensitive to the spin-orbit induced magnetic anisotropy proposed in Ref. [80]. As shown in the inset of Fig. 7.4, $|d\Delta S(T)/dT|$ increases more rapidly with decreasing width ($\propto 1/w^3$) for the 3000 ppm thermocouples than the predicted $1/w$ dependence of the slope of the Kondo resistivity [80]. At temperatures below T_f the spin flip scattering by the individual magnetic moments is suppressed by the strong internal fields which are present in the spin glass phase. This is consistent with the vanishing of the $\Delta S(T)$ below 0.4 K (see Fig. 7.4).

7.4 Conclusion

In conclusion, we have developed a new technique for quantitative measurements of the thermoelectric power on a mesoscopic scale. Our measurements clearly reveal a size dependence of the thermoelectric power of mesoscopic AuFe wires when the width of the wires is reduced below $\simeq 300$ nm. Our observations can be understood in terms of the magnetic anisotropy which affects the spins close to the surface of the sample. The spin glass freezing at lower temperatures suppresses the size effects.

Appendix A

Voltage fluctuations in the beam splitter experiment

In Chapter 3 the cross-correlation of the transmitted and the reflected channel was calculated as:

$$\langle \Delta I_t \Delta I_r \rangle = -2e\,|I|\,\Delta f \cdot T(1-T). \tag{A.1}$$

This relation is intuitively clear, since it only contains the classical shot noise value $2e\,|I|$, the frequency bandwidth Δf and a term describing the fluctuations due to the beam splitter $T(1-T)$. It is however based on the assumption that the chemical potentials of all three contacts are kept constant. But this is not the case in our experiment, since two reservoirs are connected with a resistor R_s to ground and the current flowing through it fluctuates itself. Corrections are of the order of R_s/R_K and may change the measured noise intensity with $R_K = G_0^{-1} = h/e^2$. The method to calculate those corrections is described in this appendix.

Since we measure the voltage and its fluctuation over the two resistors R_s, we need to know the chemical potentials μ_2 and μ_3 and their fluctuations (see Fig. A.1). In the case of one edge channel, we can use for the DC-limit Eq. (4.2) written as:

$$\underline{\mathrm{I}} = \frac{e}{h}\left(\underline{\underline{1}} - \underline{\underline{\mathrm{T}}}\right)\underline{\mu}, \tag{A.2}$$

where $\underline{\mu} = (\mu_\alpha)_{\alpha=1,2,3}$ and $\underline{\mathrm{I}} = (\mathrm{I}_\alpha)_{\alpha=1,2,3}$ are vectors containing the chemical potential and the current at reservoir α, respectively. $\underline{\underline{\mathrm{T}}}$ is the matrix

with the transmission probabilities between the reservoirs:

$$\underline{\underline{\mathrm{T}}} = \begin{pmatrix} 0 & 0 & 1 \\ \mathrm{T} & 1-\mathrm{T} & 0 \\ 1-\mathrm{T} & \mathrm{T} & 0 \end{pmatrix}. \tag{A.3}$$

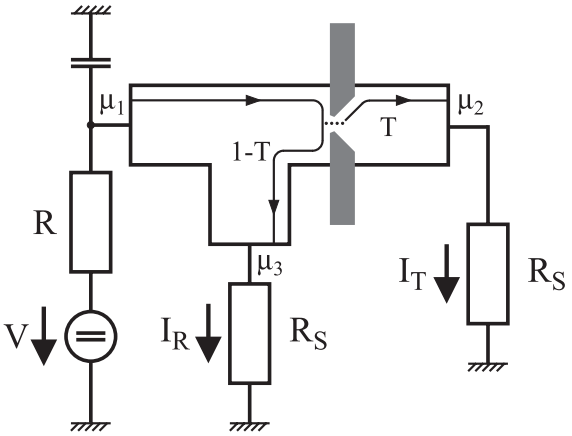

Abbildung A.1: Circuit for the beam splitter experiment described in Chapter 3.

In most theoretical considerations the chemical potentials are fixed and with the knowledge of $\underline{\underline{\mathrm{T}}}$ the resulting currents are calculated. In our experiment however the chemical potentials depend on the injected current $I = V/R$ and on the transmission probability T. As we have six unknown variables, we need three more conditions, which can be deduced from the circuit shown in Fig. A.1. The currents $I_{2,3}$ flowing through the resistors R_s determine $\mu_{2,3}$:

$$\mu_{2,3} = -eI_{2,3}R_s. \tag{A.4}$$

Furthermore the injected current I equals the current incident at reservoir μ_1:

$$I = I_1. \tag{A.5}$$

For simplicity we set $\xi = R_s/R_K$. Solving this set of equation yields:

$$\mu_1 = \frac{h}{e} I \frac{(1+\xi)(1+T\xi)}{1+2T\xi} \simeq \frac{h}{e} I = eIR_K \tag{A.6}$$

$$\mu_2 = \frac{h}{e} I\xi \frac{T+T\xi}{1+2T\xi} \simeq \frac{h}{e} I\xi T = eIR_sT \tag{A.7}$$

$$\mu_3 = \frac{h}{e} I\xi \frac{1-T+T\xi}{1+2T\xi} \simeq \frac{h}{e} I\xi(1-T) = eIR_s(1-T). \tag{A.8}$$

The approximations made here are valid if $\xi \ll 1$. In this limit the chemical potential is just the voltage drop over R_s of the current $I \cdot T$, which flows through the transmitted channel or $I \cdot (1-T)$ for the reflected channel. As can be seen from Fig. 3.4, the two plateaux for μ_2 and μ_3 are not on the same level, although in this case one channel is fully transmitted and one channel is fully reflected. This is due to the fact that ξ is not negligible.

To calculate the crosscorrelation and the autocorrelation of the current fluctuations at zero temperature, we have to introduce the scattering matrix $\underline{\underline{s}}$, which connects the quantum-mechanical wavefunctions of the incoming with the outgoing modes:

$$\begin{pmatrix} O_1 \\ O_2 \\ O_3 \end{pmatrix} = \underline{\underline{s}} \begin{pmatrix} I_1 \\ I_2 \\ I_3 \end{pmatrix}. \tag{A.9}$$

$\underline{\underline{s}}$ obeys the unitary relation: $\underline{\underline{s}}\underline{\underline{s}}^\dagger = \underline{\underline{1}}$. In the case of more than one edge channel, the elements of $\underline{\underline{s}}$ are matrices itself, in our case they are complex numbers with $|s_{\alpha\beta}|^2 = T_{\alpha\beta}$. For our three-terminal device we have in analogy to $\underline{\underline{T}}$:

$$\underline{\underline{s}} = \begin{pmatrix} 0 & 0 & s_{13} \\ t & r & 0 \\ r' & t' & 0 \end{pmatrix}, \tag{A.10}$$

with $|t|^2 = |t'|^2 = T$ and $|r|^2 = |r'|^2 = 1-T$. From Refs. [24, 25, 26] we can calculate the crosscorrelation at two arbitrary contacts α and β as:

$$\langle \Delta I_\alpha \Delta I_\beta \rangle = 2\frac{e^2}{h}\Delta f \sum_{\gamma\delta,\gamma\neq\delta} \int \mathrm{Tr}\left(\mathrm{s}^\dagger_{\alpha\gamma}\mathrm{s}_{\alpha\delta}\mathrm{s}^\dagger_{\beta\delta}\mathrm{s}_{\beta\gamma}\right) \cdot \mathrm{f}_\gamma(\mathrm{E})\left[1-\mathrm{f}_\delta(\mathrm{E})\right]\mathrm{dE}. \tag{A.11}$$

The phases of the elements of $\underline{\underline{s}}$ cancel out when calculating the correlations and we only get terms depending on T:

$$\langle \Delta I_2 \Delta I_3 \rangle = -2\frac{e^2}{h}\Delta f\,|\mu_1 - \mu_2|\,T(1-T). \tag{A.12}$$

In the limit $\xi \to 0$, μ_2 vanishes and we get the same result as in Eq. (A.1). All the other correlations, where ΔI_1 is involved, cancel out. Similarly the autocorrelation functions are calculated:

$$\langle (\Delta I_1)^2 \rangle = 0 \tag{A.13}$$

$$\langle (\Delta I_2)^2 \rangle = 2\frac{e^2}{h}\Delta f\,|\mu_1 - \mu_2|\,T(1-T) \tag{A.14}$$

$$\langle (\Delta I_3)^2 \rangle = 2\frac{e^2}{h}\Delta f\,|\mu_1 - \mu_3|\,T(1-T). \tag{A.15}$$

In order to determine the fluctuations of μ_2 and μ_3 we use the following relation:

$$\underline{\langle \mathrm{I} \rangle} + \underline{\delta \mathrm{I(t)}} = \frac{e}{h} \left[\underline{\underline{1}} - \underline{\underline{\mathrm{T}}}\right] \left[\underline{\langle \mu \rangle} + \underline{\Delta \mu(t)}\right] + \underline{\Delta \mathrm{I(t)}}. \tag{A.16}$$

The left hand side describes the current $\underline{\mathrm{I}}$ at time t flowing into the sample, which is a sum of the currents driven by the chemical potential at time t $\underline{\langle \mu \rangle} + \underline{\Delta \mu(t)}$ and the intrinsic fluctuations $\underline{\Delta I(t)}$ arising from shot noise. Subtracting the DC-component of Eq. (A.16) yields:

$$\begin{pmatrix} \delta I_1(t) \\ \delta I_2(t) \\ \delta I_3(t) \end{pmatrix} = \frac{e}{h} \begin{pmatrix} 1 & 0 & -1 \\ -T & T & 0 \\ T & 1-T & 1 \end{pmatrix} \begin{pmatrix} \Delta\mu_1(t) \\ \Delta\mu_2(t) \\ \Delta\mu_3(t) \end{pmatrix} + \begin{pmatrix} \Delta I_1(t) \\ \Delta I_2(t) \\ \Delta I_3(t) \end{pmatrix}. \tag{A.17}$$

Since the voltage fluctuations at reservoir μ_1 are cancelled out by a capacitor, $\Delta\mu_1$ vanishes and with $\delta I_{2,3}\xi \cdot h/e = -\Delta\mu_{2,3}$ we can deduce

$$\Delta\mu_2 = -\frac{h}{e}\xi\Delta I_2 \frac{1}{1+T\xi} \tag{A.18}$$

$$\Delta\mu_3 = -\frac{h}{e}\xi\Delta I_3 \frac{1}{1+\xi} - \frac{h}{e}\xi\Delta I_2 \frac{T\xi}{(1+\xi)(1+T\xi)} \tag{A.19}$$

and we finally get:

$$\langle \Delta\mu_2 \Delta\mu_3 \rangle = \frac{h^2}{e^2}\langle \Delta I_2 \Delta I_3 \rangle \frac{\xi^2}{(1+\xi)(1+T\xi)} + \frac{h^2}{e^2}\langle (\Delta I_2)^2 \rangle \frac{T\xi^3}{(1+\xi)(1+T\xi)^2}. \tag{A.20}$$

Inserting Eq. (A.12) and Eq. (A.14) into Eq. (A.20) we get the cross-correlation as a function of $|\mu_1 - \mu_2|$:

$$\langle \Delta\mu_2 \Delta\mu_3 \rangle = -2h\Delta f \, |\mu_1 - \mu_2| \, \xi^2 T(1-T) \frac{1}{(1+\xi)(1+T\xi)^2}. \tag{A.21}$$

Since we measure voltage fluctuations as a function of the current I:

$$\langle \Delta V_2 \Delta V_3 \rangle = -2e \, |I| \, \Delta f T(1-T) R_s^2 \frac{1+T\xi-\xi}{(1+2T\xi)(1+T\xi)^2}. \tag{A.22}$$

The measured voltage fluctuations are proportional to the expression for current-correlations as in Eq. (A.1), a term proportional to R_s^2 arising from the measurement resistances and a correction factor, which is equal 1 for $\xi \to 0$.

The whole calculation has been performed for one edge channel. An extension to more than one mode would result in a much more complex analysis, since the scattering matrix $\underline{\underline{s}}$ consists of matrices. However, two

simple cases are studied here. For two channels with no interchannel mixing, which are not subject to spin-splitting and have therefore the same transmission probability T, R_K can simply be replaced by $h/2e^2$. This leads to a doubling in ξ and an increase in the correction factor. The case described in Chapter 3 with four channels, where two of them are fully reflected and two are partially transmitted, the same calculation as for two channels can be performed, but by replacing I with $I/2$, since half of the current flows through noiseless channels. The correction factor can be quite substantial: for two channels, $T = 1/2$ and $R_s = 1\text{k}\Omega$, the slope is reduced by a factor of 1.2, and if R_s is increased to 3.2 kΩ a correction of 1.8 has to be performed.

Appendix B

Corrections to the noise setup calibration

This appendix describes the corrections, that have to be performed in the electron heating experiments as described in Chapter 6, if the sample resistance R is not much smaller than the series resistor R_s. Since in the heating experiments high currents have to be used to increase the electron temperature significantly, the series resistors have to be chosen small. Furthermore the sample resistance has to be high enough, otherwise the accuracy in the noise measurement is not sufficient. Hence the condition $R \ll R_s$ is not fulfilled any longer. The complete experimental setup is shown in Fig. B.1. A constant voltage source with four series resistors provides a constant current. Two of them are part of an RC-component at room temperature, which filter out the noise of the voltage source. The

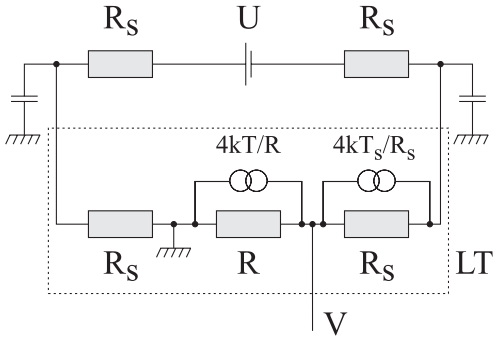

Abbildung B.1: Noise measurement setup.

other two series resistors are at low temperature on each side of the sample. One end of the sample is set to ground, while the other one may fluctuate and is used as the voltage probe for the noise measurement. Seen from this point, the resistors R and R_s are in parallel, since the other end of R_s is set dynamically to ground by the capacitance. The thermal noise of both resistors can be viewed as current sources, which are also parallel to them. Therefore a part ot the sample's thermal noise also flows through the series resistor and vice versa. If both resistors are at the same temperature, these effects compensate exactly and the thermal noise of the parallel resistance results. But if there is excess noise, e.g. due to a temperature difference in a heating experiment, corrections have to be made. The equivalent circuit is shown in Fig. B.2. The two resistors are in parallel as well as the current sources from the thermal noise. It can even be more simplified by replacing the two resistors by its equivalent parallel resistance $R \| R_s$ and by a current source with $4k(T/R + T_s/R_s)$. The measured noise over the voltage contact

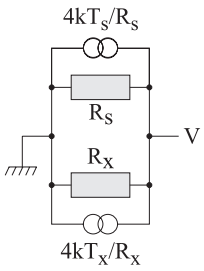

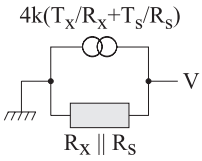

Abbildung B.2: Circuits that replace the one from Fig. B.1.

is therefore

$$4k(T_s/R_s + T/R)\left(\frac{RR_s}{R+R_s}\right)^2. \tag{B.1}$$

When calibrating the noise setup versus thermal noise, both sample and series resistor are at the same temperature:

$$T_s = T \qquad\qquad S_u^c = 4kT\frac{RR_s}{R+R_s}. \tag{B.2}$$

In the measurement only the sample temperature is raised:

$$T_s < T \qquad\qquad S_u^m = 4k(T_s/R_s + T/R)\left(\frac{RR_s}{R+R_s}\right)^2. \tag{B.3}$$

Since the measured noise S_u^m is compared to the noise obtained in the calibration S_u^c, the resulting temperature T_m is smaller than the real sample

temperature T:

$$T_m \frac{RR_s}{R+R_s} = (T_s/R_s + T/R) \left(\frac{RR_s}{R+R_s} \right)^2 . \tag{B.4}$$

The real sample temperature is then obtained by

$$T = T_m(1+\zeta) - T_s\zeta, \tag{B.5}$$

with $\zeta = R/R_s$. All the measurements shown in Chapter 6 are corrected using Eq. (B.5).

Appendix C

Calculation of the heating in mesoscopic wires

This appendix serves as a guide to estimate the electron temperature in a wire. It is a summary of all the important formulas to derive the electron temperature and can be used by an experimentalist to design an experiment such that no unwanted electron heating is present.

In the regime $L \gg l_{e-ph}$ the electron temperature is constant over the whole wire length and is a function of two parameters, the applied electric field $\mathcal{E}$ and the electron-phonon coupling constant , , which depends on the used material and probably also on the disorder (see Chapters 5 and 6). The electron temperature is then given by:

$$T_e = (T_{ph}^5 + (e\mathcal{E}/k_B)^2/,)^{1/5}. \tag{C.1}$$

Typical , -values for different materials as determined by noise thermometry are given in Table C.1.

Material	$\rho[\mu\Omega \cdot \mathrm{cm}]$	, $[10^9 K^{-3} m^{-2}]$	Ref.
Ag	0.45	0.3	[35]
Cu	3.3	8.9	[37]
Au	4	5	[36]
Al	5.5	4	[90]
Al	11	11	[90]

Tabelle C.1: Measured electron-phonon coupling constant , for different materials and disorder.

For $l_{e-e} \ll L \ll l_{e-ph}$ the temperature profile is no more constant, the mean temperature is given by:

$$\langle T_e \rangle = \frac{1}{2} T_{ph} (1 + (\nu + 1/\nu) \arctan \nu), \tag{C.2}$$

with $\nu = \sqrt{3} eV / 2\pi k_B T_{ph}$. The heating depends therefore only on the parameter eV/kT. If e.g. $eV/kT = 1$, T_e is only increased by 2.5 % above T_{ph}. On the other hand for $eV/kT \gg 1$, the electron temperature depends only on the applied voltage: $\langle T_e \rangle \simeq \sqrt{3}/8 \cdot eV/k$.

In the intermediate regime, where $L \simeq l_{e-ph}$, the heat diffusion equation from Section 5.3 has to be solved numerically, thus providing the electron temperature profile in the wire:

$$\frac{\pi^2}{6} \frac{d^2 T_e^2}{dx^2} = -\left(\frac{e\mathcal{E}}{k_B} \right)^2 +, \ (T_e^5 - T_{ph}^5), \tag{C.3}$$

For $L \ll l_{e-e}$, no electron temperature is defined. If one uses the measured noise temperature $T_N = S_I R / 4k$ as the present electron temperature, similar values as in the case $L \gg l_{e-e}$ result. For $eV/kT \gg 1$, we get $T_e = 1/6 \cdot eV/k$.

The considerations made above are only valid for ideal reservoirs. Its design plays a crucial role, if $L \ll l_{e-ph}$. Chapter 4 describes in detail, how these can be realized. On contrary, for $L \gg l_{e-ph}$, the reservoirs can be omitted, since the power is dissipated by electron-phonon scattering in the wire into the phonon bath.

Literatur

[1] Y. Imry, *Introduction to Mesoscopic Physics*, Oxford (1997)

[2] L. P. Kouwenhoven, G. Schön and L. L. Sohn, *Mesoscopic Electron Transport*, NATO ASI Series E, Kluwer Academic Publishing, Dordrecht (1996)

[3] S. Datta, *Electronic Transport in Mesoscopic Systems*, Cambridge (1995)

[4] C. W. J. Beenakker and H. van Houten, *Quantum Transport in Semiconductor Nanostructures*, in *Solid State Physics* edited by H. Ehrenreich and D. Turnbull, Academic Press (1991)

[5] K. von Klitzing, G. Dorda and M. Pepper, Phys. Rev. Lett. **45**, 494 (1980)

[6] S. A. Washburn and R. A. Webb, Advance Physics **35**, 375 (1986)

[7] B. D. Josephson, Phys. Lett. **1**, 251 (1962)

[8] B. J. van Wees, H. van Houten, C. W. J. Beenakker, J. G. Williamson, L. P. Kouwenhoven, D. van der Marel, and C. T. Foxon, Phys. Rev. Lett. **60**, 848 (1988); D. A. Wharam, T. J. Thornton, R. Newbury, M. Pepper, H. Ahmed, J. E. F. Frost, D. G. Hasko, D. C. Peacock, D. A. Ritchie and G. A. C. Jones, J. Phys. C **21**, L209 (1988)

[9] For a review, see Z. Phys. B, **85**, no. 3, 317-467 (1991); H. van Houten, C. W. J. Beenakker and A. A. M. Staring, *Coulomb-blockade oscillations in semiconductor nanostructures*, in *Single Charge Tunneling*, edited by H. Grabert and M. H. Devoret, NATO ASI Series B, Plenum, New York (1991); *Single-Electron Tunneling and Mesoscopic Devices*, edited by H. Koch and H. Lübbing, Springer (1991);

[10] For a recent review, see L. P. Kouwenhoven, C. M. Marcus, P. L. McEuen, S. Tarucha, R. M. Westervelt, and N. S. Wingreen, Proceedings of the Advanced Study Institute on *Mesoscopic Electron Transport*, edited by L. L. Sohn, L. P. Kouwenhoven, G. Schön (Kluwer, 1997); R. C. Ashoori, Nature **379**, 413 (1996).

[11] For a recent review, see M. J. M. de Jong and C. W. J. Beenakker, *Shot noise in mesoscopic systems* in *Mesoscopic Electron Transport*, edited by L. P. Kouwenhoven, G. Schön and L. L. Sohn, NATO ASI Series E, Kluwer Academic Publishing, Dordrecht (1996) and the references therein.

[12] For an introduction see Sh. Kogan, *Electronic noise and fluctuations in solids*, Cambridge University Press (1996); M. J. Buckingham, *Noise in electronic devices and systems*, Ellis Horwood Ltd., West Sussex (1983)

[13] N. Wiener, Acta Mathematica, **55**, 117 (1930); A. Khintchine, Math. Ann., **109**, no. 4, 604 (1934)

[14] F. N. Hooge, IEEE Trans. Electron Devices **41**, 1926 (1994)

[15] W. Schottky, Ann. Phys. (Leipzig) **57**, 541 (1918)

[16] M. J. M. de Jong and C. W. J.Beenakker, Phys. Rev. B **49**, 16070 (1994); P. Dielemann, H. G. Bukkems and T. M. Klapwijk, M. Schicke and K. H. Grundlach, Phys. Rev. Lett. **79**, 3486 (1997)

[17] M. B. Johnson, Phys. Rev. **29**, 367 (1927); H. Nyquist, Phys. Rev. **32**, 110 (1928)

[18] R. Landauer, J. Res. Dev. **1**, 233 (1957).

[19] D. S. Fisher and P. A. Lee, Phys. Rev. B **23**, 6851 (1981).

[20] M. Büttiker, Phys. Rev. Lett. **57**, 1761 (1986)

[21] M. Büttiker, IBM J. Res. Dev. **32**, 317 (1988)

[22] V. A. Khlus, Zh. Eksp. Teor. Fiz. **93**, 2179 (1987) [Sov. Phys. JETP **66**, 1243 (1987)];

[23] G. B. Lesovik, Pis'ma Zh. Eksp. Teor. Fiz. **49**, 513 (1989) [JETP Lett. **49**, 592 (1989)];

[24] M. Büttiker, Phys. Rev. Lett. **65**, 2901 (1990)

[25] M. Büttiker, Physica B **175**, 199 (1991)

[26] M. Büttiker, Phys. Rev. B **46**, 12485 (1992)

[27] M. Reznikov, M. Heiblum, H. Shtrikman and D. Mahalu, Phys. Rev. Lett. **75**, 3340 (1995); A. Kumar, L. Saminadayar, D. C. Glattli, Y. Jin and B. Etienne, Phys. Rev. Lett. **76**, 2778 (1996)

[28] O. N. Dorokhov, Solid State Commun. **51**, 381 (1984)

[29] C. W. J. Beenakker and M. Büttiker, Phys. Rev. B **46**, 1889 (1992)

[30] K. E. Nagaev, Phys. Lett. A **169**, 103 (1992)

[31] K. E. Nagaev, Phys. Rev. B **52**, 4740 (1995)

[32] M. J. M. de Jong and C. W. J. Beenakker, Phys. Rev. B **51**, 16867 (1995)

[33] E. V. Sukhorukov and D. Loss, Phys. Rev. Lett. **80**, 4959 (1998)

[34] M. Büttiker, private communication

[35] A. Steinbach and J. M. Martinis, M. H. Devoret, Phys. Rev. Lett. **76**, 3806 (1996)

[36] M. Henny, H. Birk, R. Huber, C. Strunk, A. Bachtold, M. Krüger and C. Schönenberger, Appl. Phys. Lett. **71**, 773 (1997)

[37] M. L. Roukes, M. R. Freeman, R. S. Germain, R. C. Richardson and M. B. Ketchen, Phys. Rev. Lett. **55**, 422 (1985).

[38] For an introduction see S. M. Sze, *VLSI Technology*, McGraw-Hill (1988)

[39] S. M. Sze, *Semiconductor devices, physics and technology*, John Wiley & Sons, 1985

[40] Wayne M. Moreau, *Semiconductor lithography, principles, practices and materials*, Plenum Press, New York (1988)

[41] D. S. Kyser and N. W. Viswanathan, J. Vac. Sci. Technol. **12**, 1305 (1975)

[42] S. V. Dubonos, B. N. Gaifullin, H. F. Raith, A. A. Svintsov, S. I. Zaitsev, Microcircuit Eng. **21**, 293 (1993)

[43] E. Weber and R. Moore, Solid State Technol. May 1979, p. 61

[44] F. Pobell, *Matter and methods at low temperatures*, Springer 1992

[45] R. Hanbury-Brown and R. Q. Twiss, Phil. Mag., Ser. 7 **45**, 663 (1954); Nature **177**, 27 (1956); Nature **178**, 1046 (1956).

[46] M. P. Silverman, Phys. Lett. A **120**, 442 (1987).

[47] H. Birk, M. J. M. de Jong, and C. Schönenberger, Phys. Rev. Lett. **75**, 1610 (1995).

[48] R. C. Liu, B. Odom, Y. Yamamoto and S. Tarucha, Nature **391**, 263-265 (1998)

[49] F. Liefrink and J. I. Dijkhuis, M. J. M. de Jong, L. W. Molenkamp and H. van Houten, Phys. Rev. B **49**, 14066 (1994)

[50] B. L. Altshuler, A. G. Aronov and D. E. Khmelnitskii, J. Phys. C **15**, 7367 (1982)

[51] R. J. Schoelkopf, P. J. Burke, A. A. Kozhevnikov, D. V. Prober and M. S. Rooks, Phys. Rev. Lett. **78**, 3370 (1997)

[52] H. Pothier, S. Guéron, N. O. Birge, D. Estève and M. H. Devoret, Phys. Rev. Lett. **79**, 3490 (1997)

[53] M. J. M. de Jong, "Shot Noise and Electrical Conduction in Mesoscopic Systems", Thesis Leiden University, 1995

[54] F. C. Wellstood, C. Urbina and J. Clarke, Phys. Rev. B **49**, 5942 (1994)

[55] D. C. Glattli, P. Jacques, A. Kumar, P. Pari and L. Saminadayar, J. Appl. Phys. **81**, 7350 (1997)

[56] N. Giordano, Phys. Rev. B **22**, 5635 (1980).

[57] S. I. Dorozhkin, F. Lell and W. Schoepe, Sol. State Comm. **60**, 245 (1986).

[58] L. W. Molenkamp and M. J. M. de Jong, Solid-State Electronics **37**, 551 (1994); M. J. M. de Jong and L. W. Molenkamp, Phys. Rev. B **51**, 13389 (1995).

[59] this is true if $\hbar\omega \ll kT$ or eV

[60] N. W. Ashcroft, N. D. Mermin, *Solid State Physics*, Saunders 1976

[61] P. W. Anderson and E. Abrahams and T. V. Ramakrishnan, Phys. Rev. Lett. **43**, 718 (1979).

[62] A. Schmid, in *Localization, Interaction and Transport Phenomena*, edited by B. Kramer, G. Bergmann and Y. Bruynseraede, (Springer, Berlin, 1985).

[63] G. Bergmann, W. Wei and Y. Zou, R. M. Mueller, Phys. Rev. B **41**, 7386 (1990).

[64] P. M. Echternach, M. R. Thoman, C. M. Gould and H. M. Bozler, Phys. Rev. B **46**, 10339 (1992).

[65] A. Mittal, R. G. Wheeler, M. W. Keller, D. E. Prober, R. N. Sacks, Surf. Sci. **361/362**, 537 (1996).

[66] J. Liu and N. Giordano, Phys. Rev. B **43**, 3928 (1991).

[67] J. F. DiTusa, K. Lin, M. Park, M. S. Isaacson and J. M. Parpia, Phys. Rev. Lett. **68**, 1156 (1992).

[68] A. Potts, M. J. Kelly, D. G. Hasko, J. R. A. Cleaver, H. Ahmed, D. A. Ritchie, J. E. F. Frost and G. A. C. Jones, Semicond. Sci. Technol. **7**, B231 (1992).

[69] K. Yoh, A. Nishida, H. Kawahara, S. Izumiya and M. Inoue, Semicond. Sci. Technol. **9**, 961 (1994).

[70] P. B. Allen, Phys. Rev. Lett. **59**, 1460 (1987).

[71] Y. L. Zhong and J. J. Lin, Phys. Rev. Lett. **80**, 588 (1998).

[72] For a recent review see, e.g.: J. A. Mydosh, *Spin glasses, An experimental introduction* (Taylor & Francis, London, 1993).

[73] G. Chen and N. Giordano, Phys. Rev. Lett. **66**, 209 (1991).

[74] J. F. DiTusa, K. Lin, M. Park, M. S. Isaacson and J. M. Parpia, Phys. Rev. Lett. **68**, 678 (1992).

[75] K. R. Lane, M. Park, M. S. Isaacson, and J. M. Parpia, Phys. Rev. **B51**, 945 (1995).

[76] V. Chandrasekhar, P. Santhanam, N. A. Pevebre, R. A. Webb, H. Vloeberghs, C. van Haesendonck and Y. Bruynseraede, Phys. Rev. Lett. **72**, 2053 (1994).

[77] G. Neuttiens, J. Eom, C. Strunk, V. Chandrasekhar, C. van Haesendonck and Y. Bruynseraede, Europhys. Lett. **34**, 617 (1996).

[78] M. A. Blachly and N. Giordano, Europhys. Lett. **27**, 687 (1994).

[79] R. Buchmann, H. P. Falke, H. P. Jablonski, and E. F. Wassermann, Phys. Rev. B **17**, 4315 (1978).

[80] O. Újsághy, A. Zawadowski, and B. L. Gyorffy, Phys. Rev. Lett. **76**, 2378 (1996); O. Újsághy and A. Zawadowski, Phys. Rev. B **57**, 11 598 (1998) and Phys. Rev. B **57**, 11 609 (1998) ; V. Fomin *et al.*, to be published.

[81] I. Martin, Y. Wan, and P. Phillips, Phys. Rev. Lett. **78**, 114 (1997).

[82] R. D. Barnard, *Thermoelectricity in metals and alloys* (Taylor & Francis, London, 1972).

[83] D. K. C. MacDonald, W. B. Pearson, and I. M. Templeton, Proc. Roy. Soc. **A266**, 161 (1962).

[84] J. Eom, G. Neuttiens, C. Strunk, C. van Haesendonck, Y. Bruynseraede and V. Chandrasekhar, Phys. Rev. Lett. **77**, 2276 (1996).

[85] G. Neuttiens, J. Eom, C. Strunk, H. Pattyn, C. van Haesendonck, Y. Bruynseraede and V. Chandrasekhar, Europhys. Lett. **42**, 185 (1998).

[86] B. L. Gallagher, T. Galloway, P. Beton and J. P. Oxley, S. P. Beaumont, S. Thoms and C. D. W. Wilkinson, Phys. Rev. Lett. **64**, 2058 (1990).

[87] L. W. Molenkamp, H. van Houten, C. W. J. Beenakker and R. Eppenga, C. T. Foxon, Phys. Rev. Lett. **65**, 1052 (1990).

[88] Here we assume that the magnetic TEP dominates all other contributions, which is well justified for dilute magnetic alloys [82].

[89] O. Laborde and P. Radhakrishna, Sol. Stat. Comm. **9**, 701 (1971).

[90] M. Henny, unpublished

List of publications

Publications in journals and proceedings:

- *Template-synthesis of nanowires in porous polycarbonate membranes: electrochemistry and morphology*, C. Schönenberger, B. M. I. van der Zande, L. G. J. Fokkink, M. Henny, C. Schmid, M. Krüger, A. Bachtold, R. Huber, H. Birk and U. Staufer, Journal of Physical Chemistry **B 101**, 5597-5605 (1997).

- *Shot noise reduction in long mesoscopic wires*, M. Henny, H. Birk, R. Huber and C. Schönenberger, in *Physics, Chemistry and Application of Nanostructures*, edited by V. E. Borisenko, A. B. Filonov, S. V. Gaponenko, V. S. Gurin, Proceedings of the Nanomeeting-97 in Minsk.

- *Electron heating effects in diffusive metal wires*, M. Henny, H. Birk, R. Huber, C. Strunk, A. Bachtold, M. Krüger and C. Schönenberger, Applied Physics Letters **71**, 773 (1997).

- *Contacting single template synthesized nanowires for electric measurements*, A. Bachtold, C. Terrier, M. Krüger, M. Henny, T. Hoss, C. Strunk, R. Huber, H. Birk, U. Staufer and C. Schönenberger, Microelectronic Engineering **41/42**, 571-574 (1998).

- *Contacting carbon-nanotubes selectively with low-ohmic contacts for four-probe electric measurements*, A. Bachtold, M. Henny, C. Terrier, C. Strunk and C. Schönenberger, J.-P. Salvetat, J.-M. Bonard and L. Forro, Applied Physics Letters **73**, 274 (1998).

- *Size dependent thermopower in mesoscopic AuFe wires*, C. Strunk, M. Henny and C. Schönenberger, G. Neuttiens and C. Van Haesendonck, Physical Review Letters **81**, 2982 (1998).

- *The 1/3-shot noise suppression in metallic diffusive wires*, M. Henny, S. Oberholzer, C. Strunk and C. Schönenberger, Phys. Rev. B **59**, 2871 (1999).

- *The Fermionic Hanbury-Brown & Twiss Experiment*, M. Henny, S. Oberholzer, C. Strunk, T. Heinzel, K. Ensslin, M. Holland and C. Schönenberger, Science **284**, 296 (1999).

Talks:

- *Growth in pores and lithography*, Nanotreff, 13./14. May 1996, Augst

- *Tilt angle evaporation technique for realization of nanowires and tunnel contacts*, (invited) Workshop on electron beam techniques used for nanostructuring, 13./14. March 1997, Raith GmbH, Dortmund

- *Noise in mesoscopic wires*, Nanomeeting-97, Minsk, 19.-23. May 1997

- *Electrical noise in metallic diffusive wires*, (invited) Festkörperkolloquium Universität Ulm, 18. December 1997

- *Electrical noise in metallic diffusive wires*, Frühjahrstagung der Deutschen Physikalischen Gesellschaft, 23.-27. March 1998, Regensburg

- *Anti-correlation of current fluctuations in a mesoscopic beam splitter*, 11th International Conference on Superlattices, Microstructures and Microdevices, 27. July - 1. August 1998, Hurghada

- *Shot noise in nanoconductors*, Seminar Physik der Kondensierten Materie, Universität Basel, 26. October 1998

Poster contributions:

- *Shot-noise reduction in mesoscopic devices*, M. Henny and C. Schönenberger, Hasliberg-2 workshop on Nanoscience, 14.-18. October 1996, Hasliberg

- *Shot-noise and electron heating in mesoscopic wires*, H. Birk, M. Henny, R. Huber, C. Strunk and C. Schönenberger, poster at "Phasdom strategic domain meeting", 10.-13. March 1997, Aachen

- *Electron heating and finite size effects in submicron AuFe spin glasses*, C. Strunk, J. Eom, G. Neuttiens, M. Henny, V. Chandrasekhar, C. Van Haesendonck and Y. Bruynseraede, poster at "Phasdom strategic domain meeting", 10.-13. March 1997, Aachen

- *Time dependent electrical current fluctuations in metallic diffusive wires*, M. Henny, C. Strunk, L. Lanz, H. Birk, R. Huber, C. Schönenberger, poster at Leybold-Heraeus Seminar on "AC and time dependent quantum transport", 20.-24. October 1997, Bad Honnef

- *Electrical noise in metallic diffusive wires*, S. Oberholzer, M. Henny, C. Strunk and C. Schönenberger, poster at "10th International Winterschool on New Developments in Solid State Physics", 23.-27. February 1998, Mauterndorf

- *The Fermionic Hanbury-Brown and Twiss experiment*, M. Henny, C. Strunk and C. Schönenberger, poster at "Phasdom strategic domain meeting", 28.-30. September 1998, Neuchatel

Curriculum Vitae

Matthias Henny

4. 12. 1971	Geboren in Basel als Sohn des Julian Henny und der Elisabeth, geborene Lachenmeier
1978 - 1983	Besuch der Primarschule in Therwil
1983 - 1987	Besuch des Progymnasiums in Therwil
1987 - 1990	Besuch des Gymnasiums in Oberwil, Matura Typus B
1990 - 1995	Studium an der Universität Basel in den Fächern Physik, Mathematik und Betriebswirtschaftslehre
1992	Vordiplom in Physik und Mathematik
1993	Vorlizentiat im Rahmen des Nebenfaches Betriebswirtschaft
1994	Diplom in Physik, Abschluss Nebenfach Betriebswirtschaft
1995	Diplomarbeit in der Gruppe von Prof. Dr. H.-J. Güntherodt, Thema: "Rastertunnelmikroskopie an ZnO(0001) und Cu_3Au(001) im Ultrahochvakuum"
1995	Beginn der Dissertation unter der Leitung von Prof. Dr. C. Schönenberger zum Thema "Shot noise in Nanoconductors" Assistent zur Vorlesung "Kondensierte Materie"
24. 9. 1998	Mündliche Doktorprüfung

Folgenden Dozentinnen und Dozenten verdanke ich meine Ausbildung:

G. Backenstoss, H. Burkhart, J. Fünfschilling, H.-J. Güntherodt, W. Hill, H. C. Im Hof, H. Kraft, W. Müller, P. Oelhafen, M. Plüss, F. Rosenkranz, H. Rudin, H. Schierenbeck, R. Schilling, C. Schönenberger, I. Sick, T. Studer, J.-B. Suck, L. Tauscher, H. Thomas, D. Trautmann, Ch. Ullrich, D. Vossieck, R. Wagner, I. Zschokke-Gränacher

Danksagung

Viele Personen haben zum Gelingen dieser Dissertation beigetragen. Den grössten Dank schulde ich meinem Doktorvater Prof. Christian Schönenberger, der diese Arbeit ermöglicht und wissenschaftlich begleitet hat. Besonders schätzte ich, dass er trotz vollem Terminkalender stets Zeit fand, anstehende Probleme wissenschaftlicher und technischer Natur kreativ und motivierend anzugehen und bis zur Lösungsfindung zu diskutieren. Bei Prof. Markus Büttiker von der Université de Genève bedanke ich mich für die Übernahme des Korreferates und für viele wertvolle, wissenschaftliche Diskussionen.

Danken möchte ich auch allen jetzigen Mitarbeitern der Forschungsgruppe für mesoskopische Physik für die Zusammenarbeit im Labor: Adrian Bachtold, Hans-Werner Fink, Jürg Furer, Tilman Hoss, Michael Krüger, Thomas Nussbaumer, Stefan Oberholzer, Christoph Strunk und Christophe Terrier. An dieser Stelle erwähne ich auch alle Ehemaligen, allesamt Leute der ersten Stunde, die sehr viel zum schnellen Aufbau der Laboratorien beigetragen haben: Holger Birk, Richard Huber und Urs Staufer. Ich danke auch allen Diplomanden für ihre Mithilfe in der Forschungsarbeit: Michael Brunner, Lukas Lanz, Daniel Mosimann und Christoph Schmid.

Bei der täglichen Arbeit im Labor wurden wir durch Alexander Heury, Urban Meier, Daniel Michel, Armin Rinklin, Werner Roth und Peter Wunderlin von der mechanischen Werkstatt unter der Leitung von Paul Cattin unterstützt. Besonders schätzte ich die Mithilfe der beiden Elektronikwerkstätten mit Peter Fornaro, Hans-Rudolf Hidber, Roberto Maffiolini, Pascal Pellmont und Andreas Tonin, sowie Bernd Heimann, Daniel Sacker und Michael Steinacher.

Den Theoretikern Harry Thomas, Daniel Loss und Eugene Sukhorukov danke ich für ihren Input zu unseren Experimenten, sowie Thomas Gramespacher von der Université de Genève für die Mithilfe bei den Berechnungen zu Kapitel 3 und Anhang A. Bei Thomas Heinzel, Sebastian Brosig und Klaus Ensslin von der ETH Zürich und Martin Holland von der University of Glasgow möchte ich mich für die Herstellung der 2DEG-Proben

bedanken. Für die Zusammenarbeit im Zusammenhang mit der Messung der breitenabhängigen Thermokraft in Spingläsern bin ich Chris van Haesendonck, Geert Neuttiens und Hugo Pattyn von der Katholischen Universität Leuven dankbar. Bedanken möchte ich mich auch bei Daniel Estève und Hugues Pothier vom CEA-Saclay für viele hilfreiche Tips zur Probenherstellung, wertvolle Diskussionen und für das Computerprogramm zur Berechnung der Elektronenverteilungsfunktion in diffusiven Drähten mit Elektron-Elektron-Wechselwirkung.

Am meisten Dank schulde ich meinen Eltern und meinen zwei Brüdern, in deren Zuhause ich mich immer wohl gefühlt habe und die mir das richtige Umfeld für meine wissenschaftlichen Interessen vermittelten. Ebenso danke ich allen, die mich daran erinnerten, dass es auch ein Leben ausserhalb der Physik gibt.

Diese Arbeit wurde vom Schweizerischen Nationalfonds zur Förderung der wissenschaftlichen Forschung und vom Fonds zur Förderung des akademischen Nachwuchses der Universität Basel unterstützt. Der Druck wurde teilweise vom Dissertationenfonds der Universität Basel finanziert.